HDL-TR-2129
November 1987

Basic Mechanisms of Radiation Effects in Electronic Materials and Devices

by F. Barry McLean
Timothy R. Oldham

This work was sponsored in part by the Defense Nuclear Agency under subtask PVRC, work unit 00174.

U.S. Army Laboratory Command
Harry Diamond Laboratories
Adelphi, MD 20783-1197

The findings in this report are not to be construed as an official Department of the Army position unless so designated by other authorized documents.

Citation of manufacturers' or trade names does not constitute an official endorsement or approval of the use thereof.

Destroy this report when it is no longer needed. Do not return it to the originator.

UNCLASSIFIED
SECURITY CLASSIFICATION OF THIS PAGE

REPORT DOCUMENTATION PAGE

Form Approved
OMB No 0704-0188
Exp Date: Jun 30 1986

AD-A186 936

1a REPORT SECURITY CLASSIFICATION UNCLASSIFIED	1b RESTRICTIVE MARKINGS
2a SECURITY CLASSIFICATION AUTHORITY	3. DISTRIBUTION/AVAILABILITY OF REPORT Approved for public release; distribution unlimited.
2b. DECLASSIFICATION/DOWNGRADING SCHEDULE	
4. PERFORMING ORGANIZATION REPORT NUMBER(S) HDL-TR-2129	5. MONITORING ORGANIZATION REPORT NUMBER(S)
6a. NAME OF PERFORMING ORGANIZATION Harry Diamond Laboratories 6b. OFFICE SYMBOL (If applicable) SLCHD-NW-RC	7a. NAME OF MONITORING ORGANIZATION
6c. ADDRESS (City, State, and ZIP Code) 2800 Powder Mill Road Adelphi, MD 20783-1197	7b. ADDRESS (City, State, and ZIP Code)
8a. NAME OF FUNDING/SPONSORING ORGANIZATION Defense Nuclear Agency 8b OFFICE SYMBOL (If applicable)	9. PROCUREMENT INSTRUMENT IDENTIFICATION NUMBER
8c. ADDRESS (City, State, and ZIP Code) Washington, D.C. 20305	10. SOURCE OF FUNDING NUMBERS PROGRAM ELEMENT NO. 62715H; PROJECT NO; TASK NO RVRA; WORK UNIT ACCESSION NO 00174

11. TITLE (Include Security Classification)
Basic Mechanisms of Radiation Effects in Electronic Materials and Devices

12. PERSONAL AUTHOR(S)
F. Barry McLean and Timothy R. Oldham

13a. TYPE OF REPORT	13b TIME COVERED	14. DATE OF REPORT (Year, Month, Day)	15. PAGE COUNT
Final	FROM Sep 86 TO Sep 87	September 1987	91

16. SUPPLEMENTARY NOTATION
This material was presented as a short course tutorial at the 1987 IEEE Nuclear and Space Radiation Effects Conference, Snowmass, CO (July 1987). HDL project: 234723; AMS code: 612120.H25

17. COSATI CODES		
FIELD	GROUP	SUB-GROUP
09	03	
20	12	

18. SUBJECT TERMS (Continue on reverse if necessary and identify by block number)
Radiation effects, ionizing radiation, nuclear weapons effects, microelectronics, metal-oxide-semiconductor (MOS) devices, bipolar devices, GaAs JFET's, total-dose ionization, transient radiation, single-event upset (cont'd on reverse)

19. ABSTRACT (Continue on reverse if necessary and identify by block number)

This report reviews the primary physical processes underlying the response of electronic materials and devices to radiation as well as the relationship of these processes to the modes of circuit degradation and failure. An overview presents brief discussions of the major radiation environments of practical interest, the interaction of radiation with solid targets, common terminology of radiation exposure, and the primary radiation effects in electronic materials, including ionization effects (radiation-induced photocurrents and space charge buildup) and atomic displacement damage effects.

An emphasis is given to the problem of total-dose ionization response, primarily in metal-oxide-semiconductor (MOS) systems. In particular, a description of the basic physical phenomena underlying the complex time history of the MOS radiation response is given, and some implications of the time-dependent response for issues of radiation testing, hardness assurance and radiation response prediction are pointed out. There is also discussion on the implications of scaling down the gate oxide thickness and on the increasingly important problem of radiation-induced leakage currents.

(cont'd on reverse)

20. DISTRIBUTION/AVAILABILITY OF ABSTRACT ☒ UNCLASSIFIED/UNLIMITED ☐ SAME AS RPT ☐ DTIC USERS	21 ABSTRACT SECURITY CLASSIFICATION UNCLASSIFIED
22a. NAME OF RESPONSIBLE INDIVIDUAL F. Barry McLean	22b TELEPHONE (Include Area Code) (202) 394-3180 22c OFFICE SYMBOL SLCHD-NW-RC

DD FORM 1473, 84 MAR 83 APR edition may be used until exhausted
All other editions are obsolete

SECURITY CLASSIFICATION OF THIS PAGE
UNCLASSIFIED

18. SUBJECT TERMS (cont'd)

neutron displacement damage, thermal effects

19. ABSTRACT (cont'd)

The discussion of total-dose ionization effects is followed by briefer treatments of transient radiation effects, including transient upset due to bulk semiconductor ionization and single-particle-induced upset, and on the effects of atomic displacement damage on electrical properties, including discussion of the time-dependent annealing of the damage as well as long-term damage coefficients. While the focus of the report is on radiation effects in silicon-based devices, there is also discussion of the similarities and differences observed in radiation effects in GaAs devices. The report ends with a brief section devoted to thermal effects, including discussions of the role of temperature in radiation response, synergistic effects of simultaneous radiation exposure and heating, and on the long-term reliability problem of hot carrier injection in MOS field-effect transistors, whose effects closely parallel those resulting from radiation.

Contents

Contents (cont'd)

Figures

Figures (cont'd)

Figures (cont'd)

Figures (cont'd)

Figures (cont'd)

Figures (cont'd)

Tables

Lists

1. Introduction

When an integrated circuit (IC) is exposed to a radiation environment, in general there will be an alteration of the electrical properties of active components of the circuit that can result in degradation of circuit performance or circuit failure. In addition, for pulsed irradiation, there may be radiation-generated photocurrents which can lead to transient circuit upset. The primary goal of the radiation effects community is to harden electronic systems against degradation, failure, or upset when these are subjected to some radiation environment. The hardening may be accomplished by one or more of several different means, including proper design and control of IC processing, appropriate device and circuit design, circumvention and error-correcting techniques, and careful piecepart screening and hardness assurance procedures.

An important if not essential ingredient of any sensible hardening effort is a good understanding of the primary physical processes underlying the response of electronic materials and devices to radiation and, further, how these processes are related to the modes of circuit degradation and failure. Armed with such a basic understanding of the physical phenomena involved, the process control or circuit design engineer is in a much improved position to formulate and to execute a successful hardening effort. In providing such a basic understanding of radiation effects in IC's, the study of the basic mechanisms of radiation response in itself plays a key role in the overall activities of the radiation effects community. Besides its educational function, basic mechanisms research serves to unify the knowledge base of the community and to instill confidence that the work of the community can be rationally understood. Basic mechanisms studies also provide direct support to many of the community's activities, such as efforts in hardening of devices and circuits, in establishing the relationship between hardness levels and circuit processing, and in programs in dosimetry, radiation testing, and hardness assurance, including the extrapolation of test data to prediction of circuit response in various radiation environments of interest.

In this report, we discuss the basic mechanisms of radiation effects in electronic materials and devices. For the most part, we focus our discussions on materials (Si and SiO_2) and devices (metal-oxide semiconductor—MOS—and bipolar) important in silicon technologies. We begin with a section on fundamentals which contains brief discussions of the major radiation environments of practical interest, the interaction of radiation with solid targets, common terminology of radiation exposure, and an overview of the primary radiation effects in electronic materials, including ionization effects, both radiation-induced photocurrents and space-charge buildup, and atomic displacement damage effects. An emphasis is given in this review to the problem of total-dose ionization response, primarily in MOS systems (sect. 3). In particular, the basic physical phenomena underlying the complex time history of the MOS radiation response are described, and some implications of the time-dependent response for issues of radiation testing, hardness assurance, and prediction are pointed out. We also discuss the implications of scaling down the gate oxide thickness and the increasingly important problem of radiation-induced

leakage currents. The section on total-dose ionization effects is followed by sections on transient radiation effects (sect. 4), including transient upset due to bulk semiconductor ionization and single-particle-induced upset; and on the effects of atomic displacement damage on electrical properties (sect. 5), including discussion of the time-dependent annealing of the damage as well as long-term damage coefficients. While the focus of the report is on radiation effects in silicon-based devices, section 6 presents some discussion of the similarities and differences observed in radiation effects in GaAs devices. The report ends with a brief section devoted to thermal effects, including discussions of the role of temperature in radiation response, synergistic effects of simultaneous radiation exposure and heating, and the long-term reliability problem of hot carrier injection in MOS field-effect transistors (MOSFET's), whose effects closely parallel those resulting from radiation.

There are several reasons for the emphasis given to the topic of total-dose ionization response. First, a review of this nature demands that the broad subject area, i.e., the major topics or problem areas, be covered on some level. But because of time and space limitations, such a coverage of the material is necessarily in the nature of an overview; it would be impossible to discuss all the topics in detail. However, in order for the reader to come away with some appreciation of the actual scope and complexity of the kinds of problems typically encountered in practice, it seems worthwhile to highlight one problem area and explore it in some greater depth than is possible for the entire subject area. Second, the topic of total-dose ionization response serves as a good specific example of the interplay between basic mechanisms research and the more practical work of the radiation effects community. In particular, as indicated above, the postirradiation behavior of MOS devices has been found to be a rather complex, time-dependent response governed by several distinct physical processes, each having its own characteristic time scale and functional dependencies on various parameters such as electric field, temperature, oxide thickness, and processing history. This rich phenomenology of time-dependent effects, while making life very interesting for the basic mechanisms researcher, has at the same time made life difficult for those workers involved with the more practical issues of radiation testing, hardness assurance, and prediction of circuit response. So, at present, there is considerable activity and interest in formulating appropriate procedures and guidelines for sensible total-dose radiation testing and hardness assurance of MOS IC's, an activity which demands close coupling between basic mechanisms work and the other activities of the radiation effects community.

2. Fundamentals

2.1 Sources and Types of Radiation

There are a variety of radiation sources and environments to which electronic systems may be exposed. The ones of most practical interest are space radiation and radiations from nuclear reactors and explosions; these have been the primary drivers of the work in radiation effects and hardening over the years. The specific types and irradiation scenarios associated with each of these environments differ widely. Therefore, when attempting to harden a particular electronics system, it is important to keep the specific application and potential radiation environment in mind. For example, systems to be used in space may have to withstand large doses of radiation which are accumulated slowly over long periods of time, whereas electronics to be used in the vicinity of nuclear explosions need to be hardened against radiation delivered in very short pulses but at very high dose rates. At the end of this section, after reviewing some basic concepts and terminology, we will return to describe in a little more specific manner the environments associated with these more practically important radiation sources.

Other radiation sources to which electronic systems may be exposed include materials with radioactive contaminants, such as uranium and thorium, which when incorporated into packaged IC's can produce isolated radiation events (e.g., alpha particle emissions); these events can result in occasional transient upsets. These are similar to single-event upsets encountered in space radiation environments (see sect. 4). Also, there are various irradiation tools used in the processing of modern small-scale, high-density IC's. These include ion implantation machines, plasma ion etching, and x-ray and electron-beam lithography tools. It is important to be aware of (and to minimize) the extent of radiation damage that may occur with the use of these tools. Finally, we mention various radiation simulators which are used both to study the fundamental nature of the interactions of radiation with matter, as well as to simulate various aspects of threat radiation environments of interest. These include such facilities as Co^{60} cells, particle accelerators (e.g., LINAC), flash x-ray machines, and nuclear reactors.

The various radiation sources or environments give rise to a variety of irradiating particles, with a wide variation in energy spectrum and time history. For example, nuclear explosions give rise primarily to pulses of gamma rays and neutrons, whereas the space environment consists essentially of a low-level, constant flux of energetic charged particles—electrons, protons, alpha particles, and heavier ions. The various types of irradiating particles can be grouped into three major categories: photons (x-rays and gammas), charged particles (electrons, protons, alpha particles, and heavy ions), and neutrons. Cosmic rays encountered in the space environment consist of a variety of charged particles generally with very high energies (>100 MeV). Neutrons of concern can be either high energy (≥10 keV) or thermal ($\sim k_B T$). Clearly, there is a large variation in the kinetic energies of the particles of concern—all the way from thermal neutrons to cosmic rays of several hundred megaelectronvolts. There is also obviously a wide variety in the mass and charge states of the radiation parti-

cles. Both photons and neutrons are charge neutral, and photons are massless (zero rest mass) as well. Energetic charged particles can be negative (electrons) or positive (protons, alpha particles), and ions can be multiply charged.

2.2 Interaction of Radiation with Solid Targets

The interaction of radiation with solid-material targets depends on a number of factors, namely, on the mass, charge state, and kinetic energy of the incident impinging particle, and on the atomic mass, charge (atomic number), and density of the target material. There are a number of specific types of interaction that can occur between the primary particles and target atoms, which are summarized in list 1. We do not discuss the details of these interactions here, as they are adequately discussed in a number of textbooks and other available references [1-7].* We do, however, indicate the general, qualitative features of the interactions, much of which is as excerpted from previous IEEE Nuclear and Space Radiation Effects Conference (NSREC) short course notes [5,6].

List 1. Specific interactions between primary irradiating particles and target atoms.

Photons (→ high-energy secondary electrons)
- Photoelectric effect
- Compton scattering
- Pair production

Charged particles
- Rutherford (Coulombic) scattering
- Nuclear interactions (heavy particles)

Neutrons
- Nuclear interactions
  - Elastic scattering
  - Inelastic scattering
  - Transmutation reactions

2.2.1 *Photon Interactions*

Photons interact with target atoms through the photoelectric effect, Compton scattering, and pair production. In all three cases, the interaction produces energetic free electrons. The energy range in which photoelectric collisions dominate depends on the atomic number, Z, of the material. The probability of a photoelectric interaction decreases with increasing photon energy and increases with Z. If the incident photon is energetic enough to emit an electron from the K shell, then most (~80 percent) of the collisions are with K-shell electrons. In the photoelectric process, the incident photon energy is completely absorbed by the emitted electron (photoelectron). If a K-shell electron is involved, then an L-shell electron will drop into the remaining empty state. Either a characteristic x ray or a low-energy Auger electron is emitted from the L shell, depending on the value of Z.

In contrast to the photoelectric effect, Compton scattering does not involve complete absorption of the incident photon. In Compton scattering, the photon energy is much greater than the binding energy of atomic electrons (such as those in the K shell). The incident photon gives up a portion of its energy to scatter an atomic electron, thereby creating an energetic Compton electron, and the lower energy scattered photon continues to travel in the target material. As the photon energy increases, Compton scattering dominates over the photoelectric effect.

The third type of photon interaction, pair production, has a threshold energy of 1.02 MeV. Above this energy, a photon striking a high-Z target may be completely absorbed and cause a positron/electron pair to form. (A positron has the same rest mass and charge as an electron, except that the charge is positive.)

Figure 1 illustrates the relative importance of the three photon interactions as a function of Z and photon energy. The solid lines correspond to equal interaction cross sections for the neighboring effects. For silicon (Z = 14), the photoelectric effect dominates at energies below 50 keV and pair production dominates at energies above 20 MeV. Over the broad intervening energy range, Compton scattering dominates. In all three cases, however, the essential result of the photon interactions is the production of energetic secondary electrons (and positrons at very high photon energy), which then undergo subsequent charged particle interactions. In other words, the primary energy transfer from the incident photons to the target occurs via the

*References are listed at the end of the text.

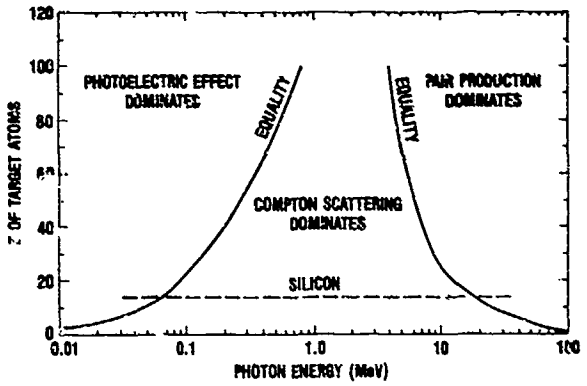

Figure 1. Illustration of relative importance of three photon interactions as function of atomic number and photon energy. Solid lines correspond to equal cross sections for neighboring effects.

secondary electron interactions, and we now discuss such charged particle interactions.

2.2.2 *Charged Particle Interactions*

Charged particles incident on a target interact primarily by Rutherford scattering (Coulomb scattering). This interaction can cause both excitation and liberation (ionization) of atomic electrons. Additionally, through Rutherford scattering, sufficient energy can be transferred to atoms to displace them from their normal lattice positions. Heavy charged particles can also undergo nuclear interactions of the type described below for neutrons. For example, a proton can be absorbed in a target nucleus, and the nucleus then emits an alpha particle.

Ionization of the target material is a major consequence of the charged particle interactions, especially for electrons and the lighter charged ions (protons, alphas). In semiconductors and insulators, ionization results in excess, nonequilibrium densities of electrons and holes; in section 2.4, we discuss the implications of ionization in these materials. Here we point out that the actual ionization processes associated with the passage of a single energetic charged particle through a solid is exceedingly complex, with the generation of a number of high-energy secondary electrons with various energies and momenta, which subsequently produce further ionization, and so on in a cascade process. However, most of the final ionization events and most of the energy transfer occur through a single type of intermediate process involving the collective motions of many valence electrons in simple oscillatory motion against the background of positive ionic cores [8]. (Because of the much larger masses, the ion cores can be considered stationary relative to the oscillating electrons.) These plasma vibrations, or plasmons as they are called in the jargon of quantum mechanics, are induced by the long-range nature of the Coulomb interaction, which extends over regions containing many atoms. The plasmon energies, corresponding to the resonance frequency of the oscillations, are typically in the range from 10 to 20 eV for most solids, depending upon the number density of valence electrons. Following its creation, a plasmon decays rapidly ($\lesssim$1 ps) via excitation of a single electron/hole pair across the bandgap. The excess kinetic energy carried by the individual electrons and holes may result in one or two further ionization events (depending upon the bandgap width) with the remainder of the energy being quickly dissipated as thermal lattice motion.

2.2.3 *Neutron Interactions*

Neutrons incident on a target undergo the following nuclear interactions: elastic scattering, inelastic scattering, and transmutation. In an elastic collision, the neutron gives up a portion of its energy to an atom of the target material, and can dislodge the atom from its lattice position. This process will occur as long as the imparted energy is greater than that required for displacement (~25 eV for most materials). The displaced atom is referred to as the primary recoil (or primary knock-on); it subsequently will lose energy to ionization and can also displace other lattice atoms. Inelastic neutron scattering involves capture of the incident neutron by the nucleus of the target atom and subsequent emission of the neutron at a lower energy. Kinetic energy is lost in this process and the target nucleus is left in an excited state. The excited nucleus returns to its original state by emission of a gamma ray. The kinetic energy of the emitted neutron is reduced, compared to the incident neutron, by the energy of the gamma ray. Inelastic neutron scattering can also cause displacement of the target atom to occur. The transmutation reaction involves capture of the incident neutron by the target nucleus and subsequent emission of another

particle, such as a proton or an alpha particle. The remaining atom is thereby transmuted, i.e., converted from one element into another.

2.2.4 *Basic Effects: Ionization and Atomic Displacements*

In spite of the seemingly complex interactions of radiation with matter, with the various dependencies of the interactions on the properties of the incident particle and target materials, in the end there are two essential consequences as far as effects on solid-state electronics are concerned: ionization (generation of electron/hole pairs) and displacement damage (dislodging atoms from their normal lattice sites). In general, as already pointed out, particles passing through electronic materials deposit a portion of their energy into ionization and the remainder into atomic displacements. However, for most practical purposes, the situation is even simpler than this statement indicates. Specifically, for charged particle irradiation—even though a certain amount of atomic displacement can occur in general, especially for the heavier ions—the primary modes of degradation of electronic devices occur as a result of ionization. Similarly, for high-energy neutron irradiation, the primary mechanisms for device degradation are attributed to atomic displacement damage, even though there can be considerable ionization associated with neutron interactions. This simplified situation is summarized schematically in figure 2. It must be kept in mind, however, that this is a simplification which applies to the commonly observed failure or degradation modes of most electronic devices. To be sure, there are situations or particular devices in which neutron-induced ionization can be significant, or in which displacement damage associated with energetic charged particle irradiation can be significant. But for the topics to be covered in this discussion, we can essentially associate ionization damage with charged particles and displacement damage with neutrons.

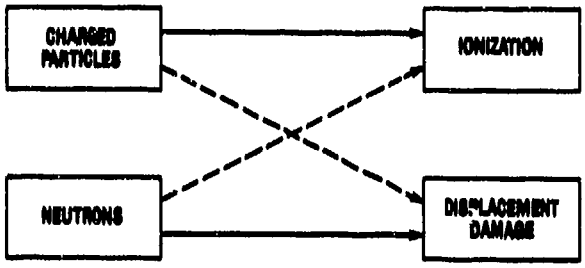

Figure 2. Schematic indicating primary radiation effects (solid lines) and secondary effects (dashed lines) in electronic materials.

2.3 Terminology of Radiation Exposure

Before going further into the specific effects of ionization or displacement damage in electronic materials, we should pause to discuss some of the commonly used terminology and units of radiation exposure and damage. This enables us to begin putting the subsequent discussion onto a quantitative basis. Table 1 highlights some of the important terminology and units of radiation exposure. Flux is simply the particle current density incident on a particular area element expressed in number of particles/cm^2-s. Particle fluence is just the time integral of the flux over some period of time (e.g., over the time of a radiation pulse) expressed in units of particles/cm^2. The energy spectrum is simply the distribution of a particle fluence (or flux) over energy, e.g., particles/cm^2-MeV.

Neutron exposure of a sample is commonly given in terms of the neutron fluence, n/cm^2. However, the amount of displacement damage from neutrons in a given material varies significantly with neutron energy (see sect. 5 for further discussion). Therefore, in order to allow meaningful comparisons between experiments using different neutron energy spectra, often neutron fluences are expressed in terms of ("normalized to") an equivalent 1-MeV neutron fluence, which is that fluence of

Table 1. Important terminology and units of radiation exposure

Type of radiation exposure	Units of measure
Flux	Particles/cm^2-s
Fluence	Particles/cm^2
Energy spectrum	Particles/cm^2-MeV
Neutrons	
• Fluence	n/cm^2
• 1-MeV equivalent fluence	n/cm^2
Ionizing radiation	
• Stopping power (linear energy transfer function (1/ρ)(dE/dx))	MeV/(g/cm^2)
• Total radiation absorbed dose	rad[a]
• Ionizing dose rate	rad(Si)/s

[a] *1 rad(Si) = 100 ergs/g(Si) = 0.01 J/kg(Si); SI unit: 1 gray (Gy) = 100 rad = 1 J/kg*

1-MeV neutrons that would produce the same electronic effect as the neutron spectrum used in a particular study.

For charged particle exposure, the amount of energy that goes into ionization is given by the stopping power, or the linear energy transfer (LET) function $\rho^{-1}dE/dx$, commonly expressed in units of MeV-cm^2/g. The stopping power has been tabulated for a number of target materials as a function of incident particle energy and atomic number. An example of the stopping power for electrons [9] and protons [10] incident on silicon is shown in figure 3. The absorbed ionizing dose (D or γ) is the integral over energy of the product of the particle energy spectrum and the stopping power. The commonly used unit of absorbed ionizing dose is the rad (radiation absorbed dose). One rad is equal to an absorbed energy of 100 ergs per gram of material. Because the energy loss per unit mass differs from one material to another, the material in which the dose is deposited must be specified when this unit is used, e.g., rad(Si) or rad(SiO_2). The SI unit of absorbed dose is the gray (Gy), which is equal to an absorbed energy of 1 J/kg, or 100 rad. However, the gray is rarely used by the radiation effects community. Finally, the ionizing dose rate ($\dot{\gamma}$) is usually expressed in rad/s.

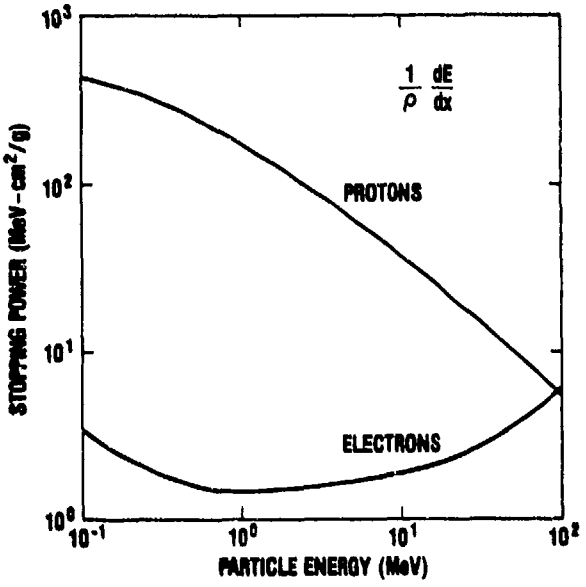

Figure 3. Stopping power as function of particle energy for electrons and protons incident on silicon.

2.4 Overview of Primary Radiation Effects in Electronic Materials

In section 2.2, we noted that the dominant effects resulting from the interaction of radiation with electronic materials are ionization (primarily associated with charged particle interactions) and atomic displacement damage (primarily associated with high-energy neutron exposure). Here, we briefly discuss the major consequences of these effects.

2.4.1 Ionization Effects

Figure 4 is a schematic of the ionization process in semiconductors and insulators. In figure 4a, an electron in the valence band is excited across the bandgap into a conduction band state, either as a direct result of interaction with an energetic

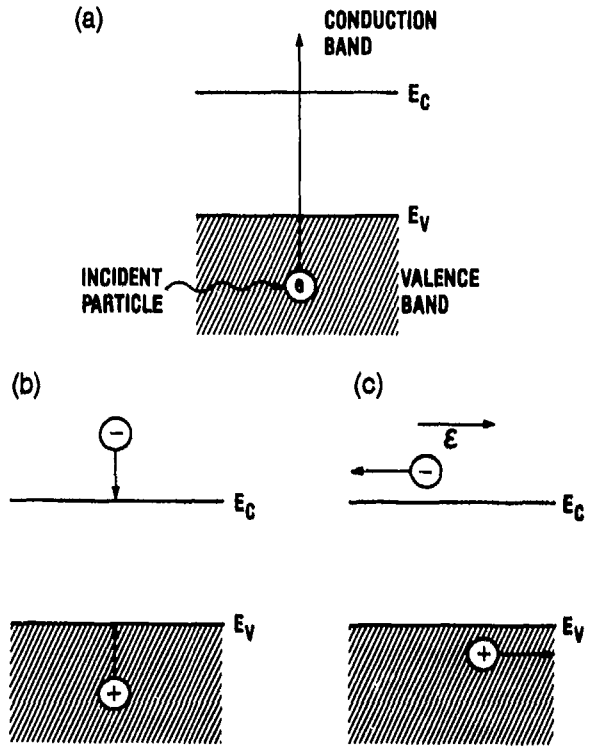

Figure 4. Schematic indicating process of ionization in semiconductors and insulators: (a) ionization event, (b) thermalization (picosecond time scale), and (c) charge separation and drift. Ionization leads to transient photocurrents and buildup of trapped charge (space-charge effects). Effective measure of damage is charge yield per unit dose (electron/hole pairs per rad).

charged particle or as the result of the decay of a plasmon excitation (the collective oscillation of a large number of valence-band electrons). Very rapidly (on the order of a picosecond), the excited electron in the conduction band and the hole left behind in the valence band lose their excess kinetic energy (fig. 4b) through lattice scattering and are "thermalized" in energy, falling to the vicinity of the conduction and valence-band edges, respectively. Then, except for some fraction (small in semiconductors, possibly large in insulators) of the electron/hole pairs which undergo what is called initial recombination, the electron and hole will be free to diffuse and drift (if electric fields are present) away from their point of generation (fig. 4c), until they either undergo recombination elsewhere in the material, or are trapped at a localized trap (defect) site, or are collected at an electrode.

If an electric field is present, there will be net charge separation and, therefore, an electric current. These radiation-induced photocurrents can be a major problem in semiconductor junction regions, resulting in transient upset of circuits or a current latchup condition, which is an induced parasitic silicon-controlled rectifier (SCR) type of current path in certain device geometries. Associated with the passage of even a single energetic heavy particle (alphas, heavy ions), there may be sufficient ionization that the photocurrent or collected charge may cause a transient upset. In this case, the upset errors are referred to as single-event upsets, as opposed to bulk ionization-induced photocurrents. Photocurrents associated with a single particle may also in some cases induce current latchup. These problems are increasing in importance as the sizes of devices are scaled down, so that less charge is necessary to cause failure.

In insulators (e.g., SiO_2), radiation-induced photocurrents are generally not a problem because of the much lower carrier mobilities and lower numbers of electron/hole pairs created. However, insulators generally contain relatively large densities of charge trapping centers at which the radiation-induced charges can be trapped for long periods of time. The trapped charges can then generate internal space-charge electric fields, which in turn can lead to voltage offsets or shifts in device operating characteristics. If sufficient space-charge fields are generated, device failure may result. This is a major radiation effects problem in metal-oxide-semiconductor (MOS) devices. In addition, internal space-charge fields due to trapped charge in field oxides and passivation insulators can turn on parasitic current leakage paths in adjoining semiconductor materials. As device dimensions are scaled down, this is becoming more of a major problem in both MOS and bipolar technologies.

The amount of damage due to ionization is directly related to the charge yield per unit dose, i.e., number of electron/hole pairs generated per rad. This is true both for the magnitudes of the induced photocurrents (for pulsed irradiation) or for the amount of trapped charge buildup for total dose effects. Table 2 lists for several important electronic materials the average ionization energy (E_p) required to generate a single electron/hole pair, as well as the initial charge pair density per rad (g_o) deposited in the material [5,6]. The latter quantity is obtained simply from the product of the material density and the deposited energy per rad (1 rad = 100 erg/g = 6.24×10^{13} eV/g) divided by E_p. As noted earlier, in wide-bandgap insulators such as SiO_2, there can be significant initial (or immediate) recombination of the electron/hole pairs before they can separate. The actual charge yield in this case is a function of the electric field and the line density of electron/hole pairs (number created per track length of the incident particle); the value of g_o listed in table 2 corresponds to the yield in the high field limit (see sect. 3.3.1 for further discussion).

Table 2. Electron-hole pair generation energies and pair densities generated by 1 rad

Material	Pair generation energy, E_p (eV)	Pair density generated per rad, g_o (pairs/cm^3)
Silicon	3.6	4.0×10^{13}
Silicon dioxide	17	8.1×10^{12}
Gallium arsenide	~4.8	$\sim 7 \times 10^{13}$
Germanium	2.8	1.2×10^{14}

2.4.2 Displacement Damage Effects

Figure 5 is a schematic of the atomic displacement process in a crystalline lattice (e.g., Si). An incident high-energy particle (e.g., a neutron) inter-

acts with a target lattice atom via one of the mechanisms mentioned in section 2.2, imparting sufficient energy to the lattice atom to dislodge it from its initial site (fig. 5a). The recoil, or knock-on, atom may travel some distance in the lattice before coming to rest, perhaps in the process itself inducing further displacements. The reflected primary particle continues through the lattice, also inducing further displacements as long as its kinetic energy is sufficiently large.

The important outcome of the atomic displacements is that defects are produced in the crystal lattice. These may be simple defects such as vacancies and interstitials, or simple combinations of these such as divacancies, or complexes of vacancies and interstitials with impurity atoms, or even more complex clusters of defects. (Defect clusters are important in neutron irradiation; see sect. 5 for further discussion.) For example, figure 5b shows a simple vacancy defect at the initial lattice site and a simple interstitial where the knock-on atom came to rest. Now, from the theory of crystalline semiconductors, we know that any defects or impurities which disturb the lattice periodicity have the effect of producing localized, discrete energy levels lying within the forbidden bandgap of the perfect lattice, i.e., lying between the conduction band minimum and the valence band maximum. It is these electronic energy levels (gap states) associated with the radiation-induced defects that cause an alteration of the electrical properties of the semiconductor crystal and lead to degradation or failure of the device. For example, additional recombination centers may be introduced which can shorten the minority carrier lifetimes and consequently degrade the gain of a bipolar transistor. The appropriate measure of displacement damage in a material is its effect on some pertinent electrical parameter, such as carrier lifetime or transistor gain. In section 5, we elaborate further on the possible effects of the radiation-induced defect centers.

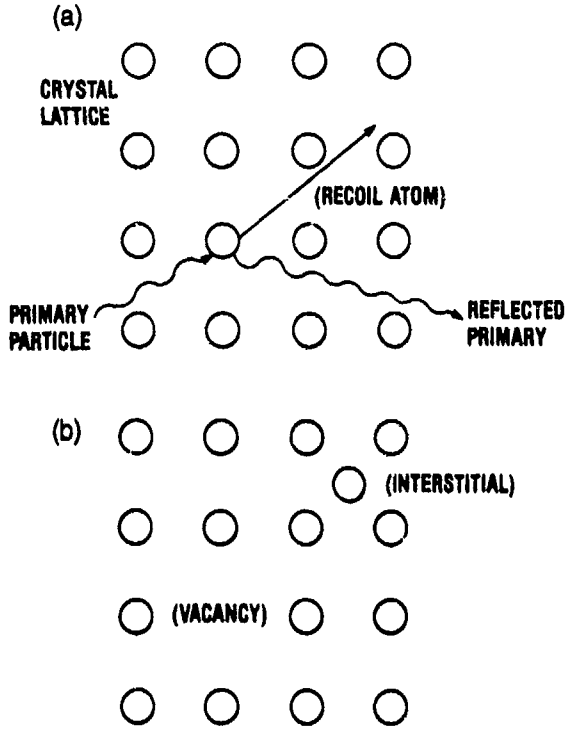

Figure 5. Schematic of atomic displacement damage in crystalline solid: (a) atomic displacement event and (b) simple radiation-induced defects (vacancy and interstitial). Atom displacements produce lattice defects which result in localized trap states—energy levels within bandgap. Measure of damage is effect on a pertinent electrical parameter (e.g., minority carrier lifetime or transistor gain).

The primary basic effects of radiation on electronic materials that we have briefly discussed are summarized in list 2. The overall content of the list is akin to the general form of a radiation specification that may be imposed on an electronic system required to operate in some radiation environment. That is, the system may be required to survive or to be hardened against failure for given

List 2. Summary of primary radiation effects in electronic materials and devices.

Ionization effects

- Total dose—charge buildup effects (D in rad(Si) or rad(SiO_2))
  - ☐ Voltage offsets
  - ☐ Induced parasitic leakage currents
  - ☐ Speed (mobility) degradation
- Transient radiation effects—induced photocurrents
  - ☐ Transient upset due to bulk semiconductor ionization ($\dot{\gamma}$ in rad(Si)/s)
  - ☐ Single-event upset due to energetic heavy ions (errors/bit-day)
  - ☐ Current latchup

Displacement damage (n/cm^2 or 1-MeV neutron equivalent)

- Induced defect states
  - ☐ Lifetime degradation
  - ☐ Transistor gain degradation

values of total dose (D, in rad(Si) or rad(SiO_2)), dose rate ($\dot{\gamma}$, in rad(Si)/s), single-event upset (SEU—usually expressed in terms of some maximum error rate per bit for the threat environment, e.g., errors/bit-day), and neutron fluence (n/cm^2). Some typical target values for good radiation-hardened circuits are total dose to 1 Mrad, $\dot{\gamma}$ to 10^9 rad/s, SEU to 10^{-7} errors/bit-day, and neutron fluence to 10^{14} cm^{-2}.

2.5 Characteristics of Specific Radiation Environments

Obviously, when trying to define a radiation survivability specification for an electronic system, we must bear in mind the potential radiation environment. We end this section simply with several lists (lists 3 to 5), which summarize some pertinent information concerning the three radiation environments of most practical interest: space, nuclear explosions, and nuclear reactors. These lists (1) summarize the qualitative characteristics of the various environments, (2) indicate the primary failure mechanism of IC's when exposed to these environments, and (3) note some of the radiation simulators available to obtain pertinent radiation effects data. For the most part, the lists are self-explanatory. We do, of course, discuss the various failure mechanisms in some detail in the remainder of this document, but in doing so it is helpful to have some idea of the qualitative features of the real threat environments. Further, essentially all the data we discuss were generated with one of the several common radiation simulator test facilities. Finally, we note that the lower bounds on the various radiation characteristics indicated on lists 3 and 4 indicate generally the levels beyond which serious hardening efforts must be implemented if IC's are to continue operating effectively. Similar bounds are not indicated on list 5 for nuclear reactors, because the requirements here depend critically on the placement of electronic parts and whether the parts are intended for use in a normal reactor operation environment or for an accident scenario.

List 3. Characteristics of space radiation environment.

Environment
- Low ionization dose rate (<1 rad/s)
- Total dose (>10^5 rad)
- High-energy electrons and protons trapped in earth's magnetosphere
- Cosmic rays (electrons, protons, alphas, heavy ions)

Primary failure mechanisms
- Total-dose-induced charge buildup
- Single-event upset

Test simulators
- Low-dose-rate ionization sources: Co^{60}, low-energy x-ray tester
- High-energy particle sources: proton and heavy ion beams

List 4. Pertinent features of radiation from nuclear explosion.

Environment
- High-dose-rate gamma flux ($\dot{\gamma}$ >10^8 rad/s)
- Total dose (>10^4 rad)
- Delayed high-energy neutron flux (fluence > 10^{13} n/cm^2)

Primary failure mechanisms
- Total-dose-induced charge buildup
- Transient-photocurrent-induced upset and latchup
- Neutron displacement damage

Test simulators
- Ionization sources:
  - ☐ Flash x ray, LINAC electron beam (for $\dot{\gamma}$)
  - ☐ Co^{60}, low-energy x-ray tester (for D)
- Neutron sources: nuclear reactor

List 5. Features of nuclear reactor radiation environment.

Environment
- Steady-state neutron flux
- Low to moderate ionizing dose rate (gamma rays)

Primary failure mechanisms
- Displacement damage
- Total-dose-induced charge buildup

Test simulators
- Nuclear reactor
- Moderate-dose-rate ionization sources: Co^{60}, low-energy x-ray tester

3. Total-Dose Ionization Effects

3.1 Introduction

As pointed out in the previous section, one of the major effects associated with radiation-induced ionization in electronic materials is that of trapped-charge buildup, which induces internal space-charge fields that interfere with the normal (designed) operation and control of devices. This problem is primarily associated with the insulating films used in modern IC technologies, and it is the major type of effect encompassed in the term "total-dose ionization." The major focus of work in this area over the past 20 years or so [11] has been on the MOS technologies because of the charge-trapping effects in the thin silicon dioxide films employed in these technologies, both as gate oxides over the active semiconductor channel region and as field, isolation, and passivation oxides. However, as device dimensions shrink, the total-dose problem is increasing in concern as well for the bipolar technologies in connection with trapped-charge-induced leakage paths near field and passivation oxides. Here, for the purposes of discussing the physics, we focus on the total-dose charging problem in the SiO_2 gate oxides of MOS structures. The basic mechanisms underlying the charge trapping are the same in both gate and field/passivation oxides; only the circuit manifestations differ. We return to briefly discuss the induced leakage current problem at the end of this section for both MOS and bipolar structures. We note here at the outset that, in general, charging of the oxide regions can occur both within the bulk of the oxide films as well as at the interfaces between the oxides and the semiconductor regions.

Figure 6 shows a simple schematic of a MOSFET, in this case an n-channel device using a p-type Si substrate. When a bias potential is applied to the gate contact, there will be an electric field across the gate oxide region and into the Si surface region immediately below the gate region. If the gate bias is sufficiently large and positive (for n-channel operation), the majority carriers (holes in p-type Si) will be repelled from or depleted in this surface region, and minority carriers (electrons) will be attracted to this region, forming what is called an inversion layer. If now also a potential difference is applied between the source and drain contacts (n^+-doped regions in fig. 6), the inversion layer provides a low-resistance current channel for electrons to flow from the source to the drain. The device is then said to be turned on (fig. 6a), and the control gate bias potential at which the channel just begins to conduct appreciable current is called the turn-on voltage or threshold voltage of the device.

The total-dose ionization problem that occurs in this structure is then due to the radiation-induced charging (normally positive) of the thin gate oxide region, which generates additional space-charge fields at the Si surface. These additional induced fields result in voltage offsets or shifts in the turn-on voltages of the devices, which lead to circuit degradation and failure. For example, for sufficiently large amounts of trapped positive charge for the device schematically shown in figure 6, the device may be turned on even for zero applied gate bias (fig. 6b). In this case, the device is said to have failed by "going depletion mode."

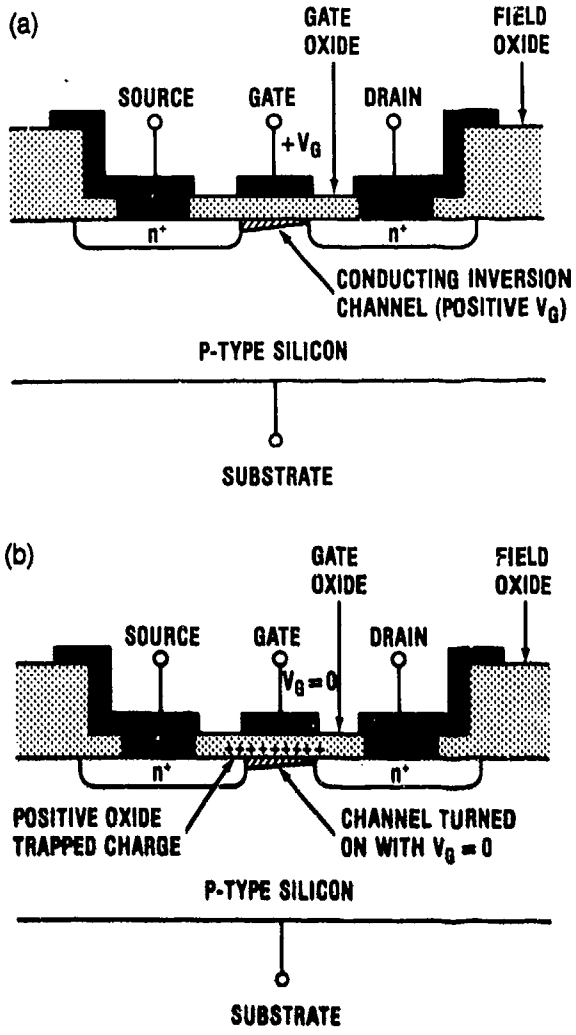

Figure 6. Schematic of n-channel MOSFET illustrating basic effect of total-dose-ionization-induced charging of gate oxide: (a) normal operation and (b) postirradiation.

Conceptually, in a broad sense, the radiation-induced oxide-charging problem is fairly simple to understand. It is only when one gets down to grappling with details of the radiation response—particularly when trying to quantify the response for practical applications—that one begins to appreciate some of the complexities involved in radiation effects studies. For example, there is a relatively complex time dependence of the radiation response of the simple MOS structure shown in figure 6, having to do with a wide variation in the characteristic time scales for various physical processes involved, such as for the charge generation, transport, trapping and annealing processes, and interface-state generation at the SiO_2/Si interface. The complexity of the time-dependence response has implications not only for understanding the basic physics of the response, but also certainly for practical issues of testing, prediction, and hardness assurance. In this discussion, we have chosen to highlight the radiation response of MOS structures, mainly in order to give the reader more of an in-depth understanding, in one particular problem area, of the complexities that may occur when these sorts of issues are addressed.

We begin with an overview of the time-dependent radiation response of MOS systems and then discuss in some further detail each of the major physical processes involved in the response. Then we turn to some of the implications of the response for the issues of testing, prediction, and hardness assurance. We end with brief discussions concerning the implications of scaling the gate oxide thickness down and with leakage currents associated with field/passivation/isolation oxide regions of IC's.

3.2 Overview of Radiation Response of MOS Structures

Figure 7 shows a schematic energy band diagram for an MOS structure where positive bias is applied to the gate, so that free electrons in the oxide layer will be swept toward the gate and holes will be attracted to the Si substrate. (In an energy

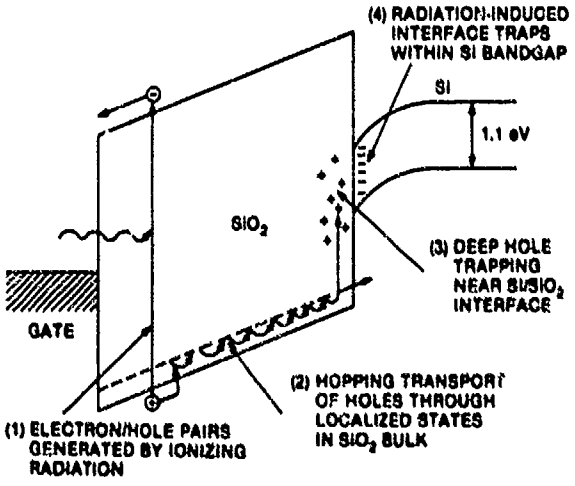

Figure 7. Schematic energy band diagram of SiO_2 MOS structure for positive gate bias, indicating major physical processes underlying radiation response.

band diagram—which is essentially equivalent to a potential energy diagram—electrons want to fall downhill, whereas holes will float upwards.) Also indicated in figure 7 are the four major basic processes contributing to the radiation response of such a system, which we now discuss.

As already mentioned several times, the part of an MOS structure most sensitive to ionizing radiation is the oxide insulating layer (SiO_2), which in present-day devices is generally less than 100 nm thick. When the radiation passes through the oxide, the energy deposited creates electron/hole pairs. in SiO_2, the radiation-generated electrons are much more mobile than the holes, and they are swept out of the oxide (collected at the gate electrode) in times on the order of picoseconds [12]. However, in that first picosecond or two, some fraction of the electrons and holes will recombine. This fraction depends greatly on the applied field and on the energy and type of the incident particle. The holes which escape initial recombination are relatively immobile and remain behind near their points of generation, causing negative voltage shifts in the electrical characteristics of MOS devices, e.g., in threshold voltage (V_T) for MOS transistors (MOSFET's) or flatband voltage (V_{fb}) for MOS capacitors. These initial processes of pair creation and prompt recombination—which determine the actual charge (hole) yield in the SiO_2 film and consequently the initial (maximum) voltage shift—constitute the first major factor of the MOS response.

Over a period of time extending typically at room temperature from 10^{-7} s to the order of seconds (but much longer at lower temperatures), the holes undergo a rather anomalous stochastic hopping transport through the oxide in response to any electric fields present. (They move toward the Si substrate for the gate bias situation depicted in fig. 7). This hole transport process, which is very dispersive in time, is the second major factor of the MOS response. It gives rise to a short-term, transient recovery in the voltage shifts and is sensitive to many variables including primarily applied field, temperature, and oxide thickness, and, to a lesser extent, oxide processing history.

When the holes reach the SiO_2 interface (for positive applied gate bias), some fraction of them are captured in long-term trapping sites, and cause a remnant negative voltage shift that is not sensitive to the silicon surface potential and which can persist in time for hours to years. This long-lived radiation-induced voltage shift component is the most commonly observed form of radiation damage in MOS devices. The long-term trapping of holes near the SiO_2/Si interface, as well as their subsequent annealing in time, constitutes the third major factor of MOS response indicated on figure 7; hole trapping and annealing are very sensitive to the processing of the oxide and to other variables such as field and temperature.

The fourth and final component of MOS response is that of a radiation-induced buildup of interface traps right at the SiO_2/Si interface. These are localized states with energy levels within the Si bandgap. Their occupancy is determined by the location of the Fermi level at the interface, and, consequently, the radiation-induced interface traps give rise to a voltage shift component which depends on the silicon surface potential. In general, there can be both prompt interface traps, present immediately after a radiation pulse, as well as a delayed time-dependent buildup of states which can continue for thousands to tens of thousands of seconds at room temperature. Both the magnitude and nature (relative ratio of prompt and delayed components) of the interface traps are also highly dependent upon oxide processing, as well as upon other variables such as temperature and applied field (both magnitude and polarity).

A major electrical consequence of the radiation-induced charging of the SiO_2 film (including transporting holes, trapped holes, and interface traps) is a shift in pertinent voltage operating points for devices, such as in the threshold voltage V_T for a MOSFET. Let us write the threshold voltage as

$$V_T(t) = V_T^o + \Delta V_T(t). \qquad (1)$$

where V_T^o is the threshold voltage before irradiation and $\Delta V_T(t)$ is the voltage shift following radiation exposure, and for reasons already discussed, $\Delta V_T(t)$ is in general time dependent. The preirradiation threshold voltage is defined and its explicit expression is given in any textbook discussing MOS transistors [13-16]. It depends upon temperature, gate-semiconductor work function difference,

substrate doping density, oxide layer thickness, and substrate bias. There are also contributions from any oxide charges and interface traps existing before irradiation (and there are always some small amounts of these, but usually for good devices their areal densities are $\lesssim 10^{10}$ cm^{-2}).

Based on figure 7 and its discussion, we break the radiation-induced threshold voltage shift into three components:

$$\Delta V_T(t) = \Delta V_{ot}(t) + \Delta V_{ot}(t) + \Delta V_{it}(t), \quad (2)$$

where $\Delta V_{ot}(t)$ is the (short-term) contribution from the radiation-generated mobile holes transporting in the oxide bulk, $\Delta V_{ot}(t)$ is due to the deep trapped holes near the interface, and $\Delta V_{it}(t)$ is the contribution from the charged interface traps. Note that all three components are in general time dependent. They are given explicitly as

$$\Delta V_{ot}(t) = -q/C_{ox} \int_0^{d_{ox}} dx\,(x/d_{ox})\, n_h(x,t), \quad (3a)$$

$$\Delta V_{ot}(t) = -q/C_{ox}\, \Delta N_{ot}(t), \quad (3b)$$

$$\Delta V_{it}(t) = -\Delta Q_{it}(t)/C_{ox}. \quad (3c)$$

where q is the electronic charge, d_{ox} is the oxide thickness, and C_{ox} is the oxide capacitance per unit area ($C_{ox} = \epsilon_{ox}/d_{ox}$) where ϵ_{ox} is the dielectric constant of the oxide. In equation (3a), $n_h(x,t)$ is the space- and time-dependent density of free (mobile) holes, and distance x in the oxide is measured relative to the gate/SiO_2 interface. In equation (3b) $\Delta N_{ot}(t)$ is the radiation-induced areal density of deep trapped holes near the SiO_2/Si interface; it is time dependent both because of its time-dependent buildup as the transporting holes reach the interface and because of its long-term annealing, which can extend out to years. In equation (3c), we leave the sign of the radiation-induced interface trapped charge $\Delta Q_{it}(t)$ unspecified, as it can contribute either a net negative or net positive charge depending on the position of the Fermi level at the Si surface at inversion. (Usually ΔQ_{it} is negative for n-channel and positive for p-channel devices at the threshold voltage; see sect. 3.3.4.) We note that in general a voltage offset is simply proportional to the first moment of the induced oxide charge relative to the gate interface. For the mobile hole distribution, equation (3a) retains this definition explicitly, since the transporting holes can be distributed through the bulk of the oxide. For both the long-term trapped holes and interface traps, $\langle x \rangle \cong d_{ox}$, with the resulting simplifications exhibited in equations (3b) and (3c). Also we note that positive charge induces a negative shift in V_t and negative charge a positive shift.

As a further aid in understanding some of the basic processes involved in the time-dependent response of MOS structures, we show in figure 8 (from Srour [5]) schematic diagrams illustrating the positions and magnitudes of the radiation-induced charges in the SiO_2 before and after an infinitesimally short pulse of radiation. The processes depicted here include charge generation and initial recombination, hole transport, and long-term hole trapping. The annealing of the trapped holes and interface trap buildup are not included. Figure 9 illustrates schematically the corresponding capacitance-voltage (C-V) curves for an MOS capacitor for the times indicated in figure 8.

The preirradiation condition ($t = 0^-$) is depicted in figure 8a—no oxide charges; the corresponding C-V curve is indicated by the $t = 0^-$ curve of figure 9. At $t = 0$ (fig. 8b), the radiation pulse occurs, generating electron/hole pairs across the oxide bulk. In a time of the order of picoseconds ($t = 0^+$) some of the electron/hole pairs will recombine (fig. 8c) and the relatively highly mobile electrons will transport toward the gate and be collected (fig. 8d). The corresponding C-V curve is shifted far to the left in the negative voltage direction, as indi-

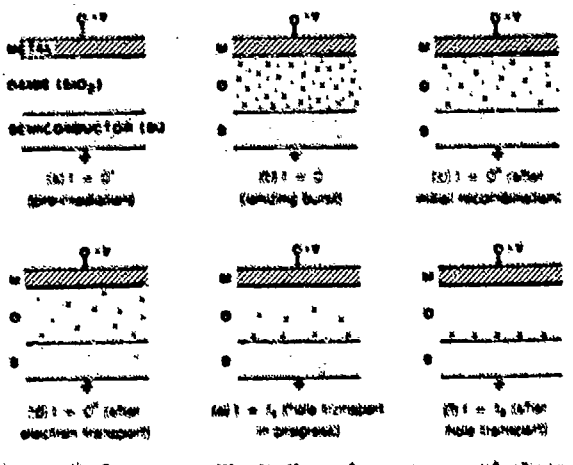

Figure 8. Schematic illustration of processes of charge generation and initial recombination, hole transport, and long-term trapping near SiO_2/Si interface [5].

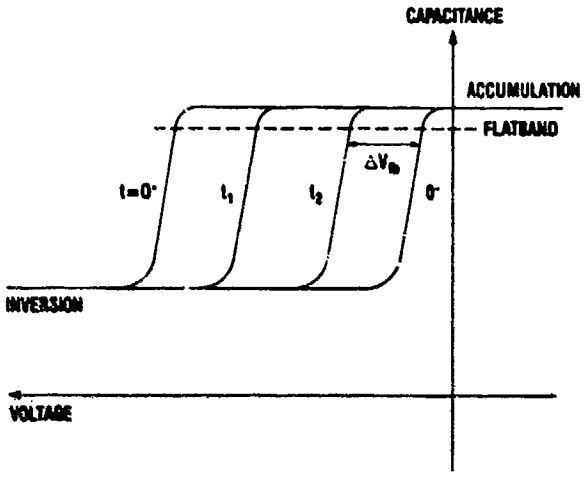

Figure 9. Capacitance/voltage curves corresponding to times and conditions shown in figure 8 [5].

cated by the curve labeled $t = 0^+$ in figure 9. The magnitude of the flatband voltage shift $\Delta V_{fb}(0^+)$ is maximum at this time. Then the holes begin their relatively slow hopping transport toward the SiO_2/Si interface, where some fraction of them are captured in the long-term trapping sites. Figure 8e at $t = t_1$ shows the intermediate situation, where some holes are still transporting, some have been collected by the substrate electrode, and some have been trapped near the interface. Because less positive charge remains in the oxide, the C-V curve has annealed back partially at $t = t_1$ in the positive voltage direction from its initial shifted position at $t = 0^+$. The final charge configuration ($t = t_2$) after completion of the hole transport is depicted in figure 8f, where only the long-term, trapped holes remain near the SiO_2/Si interface, giving rise to a long-term flatband voltage shift in the C-V characteristic, as indicated by the $t = t_2$ curve of figure 9.

The overall, actual situation is even more complicated than figures 8 and 9 would indicate. In general, there can be long-term annealing of the deeply trapped holes via tunneling of electrons from the Si substrate, which gives rise to a much slower recovery of the C-V curve further toward the pre-irradiation curve. And there are radiation-induced interface traps which, in general, can be present both right after irradiation ($t = 0^+$) as well as continuing to build up over long time periods. The interface traps not only contribute to the shift of device characteristics, but also cause a distortion (stretchout) of the curves (C-V or I-V) because the charge state of the traps is dependent upon the surface potential (and hence upon the applied bias).

Concluding this overview section, the schematic, time-dependent recovery curve in figure 10 shows the radiation-induced shift in threshold voltage as a function of log-time from 10^{-6} to 10^{9} s for a radiation-hardened n-channel MOSFET under positive gate bias at room temperature after exposure to an ionizing radiation pulse of ~1 μs in duration. This figure is schematic in that it does not show real data (over the enormous time regime depicted), yet it is basically representative of the composite response of an actual hardened n-channel device. The figure relates the major features of the response with each of the primary processes indicated in figure 7. The initial shift, $\Delta V_T(10^{-6}$ s), which is also the maximum shift, is determined mainly by the electron/hole pair creation in the SiO_2 bulk and by the initial recombination processes. (There can, however, be some contributions from annealing by hole transport during the pulse and from prompt interface-state production, which is low for a hardened oxide.) The short-term annealing that is shown occurring out to about 10^{-2} s is due to the hole transport process. The shift remaining at 10^{-2} s is primarily due to the deep hole trapping near the SiO_2/Si interface, which then anneals out slowly in time (approximately linearly with log-time) essentially out to infinite time (to 10^{9} s in fig. 10).

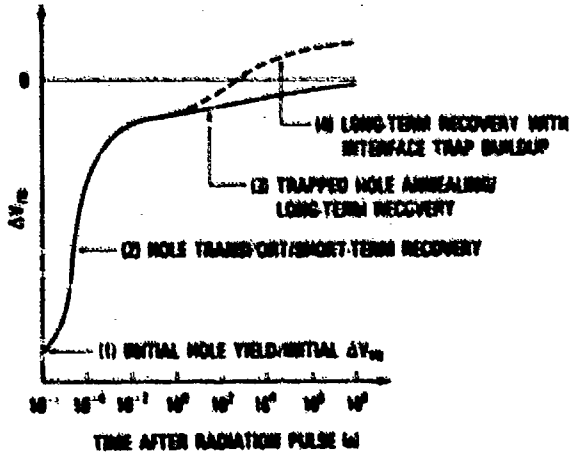

Figure 10. Schematic time-dependent threshold-voltage recovery of n-channel MOSFET following pulsed irradiation, relating major features of response to underlying physical processes.

The solid curve in figure 10 corresponds to transport, trapping, and annealing of holes alone. In addition to long-term annealing of trapped holes, however, a buildup of radiation-induced interface traps may occur, typically in the time regime between $\sim 10^{-2}$ and 10^3 s, which is indicated by the dashed curve in figure 10. (For an n-channel device, the interface-state contribution to V_T is positive, corresponding to net negative interface trap charge at the threshold voltage.) If the interface trap contribution is relatively large, the threshold voltage may actually recover past its preirradiation value (ΔV_T going positive), giving rise to what is called superrecovery or rebound. This effect can also lead to circuit failure, if sufficiently large. If there is a relatively large component of prompt interface trap production, then there would simply be an additional upward translation of the solid and/or dashed curves for all time. Again, because of the annealing of trapped positive charge, superrecovery or rebound could occur.

In any case, because of the several different physical processes involved, each having different characteristic times, it is apparent that the overall time history of the recovery can be fairly complex, with important implications for sensible testing procedures, hardness assurance, and prediction. In simplest terms, one must be able to extract from test data—usually done over a very limited time regime and for a limited range of experimental conditions—the expected performance of an IC in a particular threat environment which may involve a completely different time regime (perhaps orders of magnitude shorter or longer). Before addressing these issues, we first discuss in further detail the basic physical processes responsible for the complex time history depicted in figure 10.

3.3 Descriptions of Physical Processes Underlying Radiation Response of MOS Devices

In this section, we provide a little more detail and discussion of each of the physical mechanisms mentioned in the previous subsection as being important factors underlying the radiation response of MOS devices (see fig. 7). This is not a detailed exposition or review of these subjects; rather, our intent is to provide the reader a little more feeling for these processes by summarizing their major characteristics and indicating the main concepts used in their model descriptions. We discuss a few representative examples of data sets for each process, and also provide some basic references for the reader to obtain further information. The reader not interested in such detail may wish to proceed to section 3.4.

3.3.1 Initial Hole Yield

The initial hole yield in the oxide determines the initial (maximum) voltage shifts of MOS devices and sets the scale for the amount of damage (at any time) due to ionizing radiation. The two major factors that determine the initial hole density are the electron/hole pair creation energy and the field-dependent fraction of holes which escapes the initial recombination processes. The initial value of the threshold voltage shifts is then simply related to the initial hole density via the dose and geometric (oxide thickness) factors.

The electron/hole pair creation energy E_p was determined by Ausman and McLean [17] to be 18 ± 3 eV, based on an analysis of experimental data of Curtis et al [18]. This result has been confirmed independently by others since [19,20], including a recent more accurate set of measurements and analysis by Benedetto and Boesch [21] which establishes E_p to be 17 ± 1 eV.

From the value of E_p, the initial electron/hole pair density per unit dose is easily determined to be 8.1×10^{12} cm^{-3} rad^{-1}(SiO_2) (see table 2, sect. 2). But this initial density is quickly reduced by the initial recombination processes occurring in picoseconds, before the electrons are swept out of the oxide and collected. The fraction of holes escaping initial recombination, $f_y(E_{ox})$, which determines the final hole yield, is determined mainly by two factors: the magnitude of the oxide electric field E_{ox}, which is acting to separate the charge pairs, and the initial line density of electron/hole pairs created by the incident radiation particle. The pair line density, which is determined by the linear energy transfer (LET) and therefore a function of the incident particle type and energy, is inversely proportional to the average separation distance between electron/hole pairs. Obviously, the closer the average spacing of the pairs, the more recombination that occurs for a given field, and the less will be the final yield of holes.

The initial recombination problem has not been solved analytically for arbitrary pair line density. However, analytic solutions do exist in the limiting cases, namely, where the charge pairs are far apart (geminate model) and the opposite, where the electron/hole pairs are very close together (columnar model). The characteristic distance scale which distinguishes these cases is the thermalization radius of a single electron/hole pair, i.e., the average separation distance between an electron and hole of the *same* pair after they have dissipated their excess kinetic energy and reached thermal equilibrium energies. For SiO_2 the average thermalization distance is about 8 nm [17,22].

Figure 11 illustrates schematically the two limiting cases for which recombination models have been solved. For the geminate case (fig. 11a) the separation distance between pairs is much larger than the thermalization distance. Then one can treat only the recombination between the individual members of the same pair. That is, one need only calculate the recombination probability of a single isolated charge pair whose members are attracted to each other via the mutual Coulomb attraction while, at the same time, they undergo both a drift motion (in opposite directions) in response to the local electric field and a random diffusive motion driven by the thermal fluctuations of the system. The geminate recombination model was first formulated by Smoluchowski [23] and later solved by Onsager [24], originally for recombination of electrons and positive ions in gases.

The other limiting case (fig. 11b) occurs when the average pair separation distance is much less than the thermalization distance. In this case—columnar recombination—the individual electron/hole pairs lose their identity, and recombination must be considered between many electrons and holes lying in a cylindrical distribution around the track of the incident particle. Obviously, the probability of recombination of an individual carrier in this case is significantly greater than in the geminate model because of the enhanced probability of recombination encounters between opposite charges. The columnar model was originally solved by Jaffe [25], expanding on previous work by Langevin [26]; more recently, a more accurate, numerical treatment has been done by Oldham [22] which also extends the range of applicability of the model.

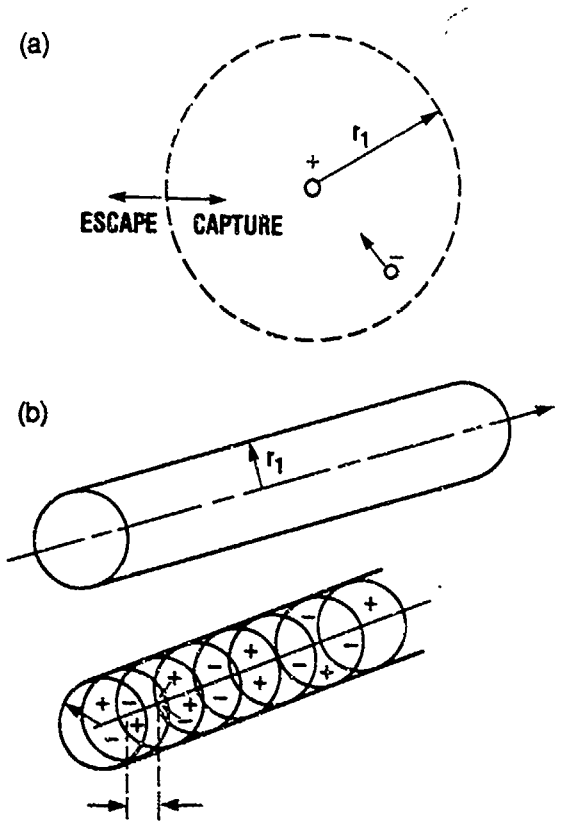

Figure 11. Schematic diagrams indicating limiting pair separation distances for two recombination models: (a) geminate (separate electron/hole pairs) and (b) columnar (overlapping electron/hole pairs).

These models have been applied to the initial recombination process in thermally grown SiO_2 films with good success in recent years. For example, low-LET particles such as high-energy electrons (including the high-energy secondary Compton electrons from Co^{60} gamma interactions) generate a sparse density of charge pairs along their tracks (for a 1-MeV electron, the average pair separation distance is ~50 nm), and the geminate model fits the results very well. On the other hand, very-high-LET particles, such as protons, alpha particles, and other heavier ions, generate a high density of pairs along their tracks (for example, a 1-MeV proton generates an electron/hole pair on the average about every 0.3 nm), and the columnar model is successful in describing the experimental results. As one might expect, many experiments of practical interest fall in the transition region between these two models for the limiting cases of pair separation distance. However, the experimental results reflect a smooth continuous transition

between the limiting cases. That is, intermediate cases show increasing columnar behavior (stronger recombination) as the density of electron/hole pairs is increased. Figure 12 is a compilation of a number of experimental results [17,18,20,21,27] of the fractional hole yield f_y versus electric field for a number of particles spanning the range from low to high LET. For these particle sources at a field of 1 MV/cm, the yield varies from almost 90 percent for low-LET particles (12-MeV electrons and Co^{60}) to only about 6 percent for the high-LET 2-MeV alpha particles. This figure clearly shows that recombination is a real and often important effect when MOS responses to different radiation sources are compared.

Finally, knowing the initial pair volume density per rad ($g_o = 8.1 \times 10^{12}$ cm^{-3} $rad^{-1}(SiO_2)$) and the fractional hole yield after recombination $f_y(E_{ox})$ (from fig. 12), the initial threshold (or flatband) voltage shift is easily obtained. Assuming a uniform generation density across the oxide layer, the total initial areal charge density of holes which escape recombination is $\Delta Q_h = q g_o d_{ox} f_y(E_{ox}) D$, where d_{ox} is the oxide thickness and D is the dose in rad(SiO_2). The initial threshold shift is related to ΔQ_h as

$$-\Delta V_T(0^+) = \Delta Q_h / 2C_{ox} = [q g_o d_{ox} f_y(E_{ox}) D] / 2C_{ox} \qquad (4)$$

where $C_{ox} = \varepsilon_{ox}/d_{ox}$, the factor of 2 comes from the fact that the centroid of a uniform charge density is

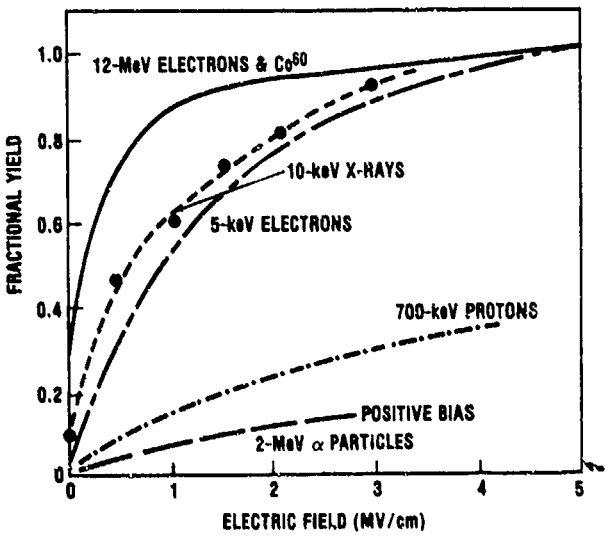

Figure 12. Experimentally measured fractional hole yield versus electric field in SiO_2 for a number of incident particles.

$d_{ox}/2$, and a negative voltage shift is explicitly indicated corresponding to the positive sign of the induced charge. Finally, substituting for the constant factors in equation (4), we have

$$-\Delta V_T(0^+) = 1.9 \times 10^{-8} d_{ox}^2 f_y(E_{ox}) D \,. \qquad (5)$$

Here, the units of ΔV_T are volts if d_{ox} is expressed in nanometers and D in rad(SiO_2). Equation (5) explicitly shows the dependence of the initial voltage shifts on oxide thickness squared, indicating a significant improvement in the radiation susceptibility of devices having thinner gate oxides.

3.3.2 Hole Transport

The transport of the holes through the SiO_2 oxide layer, which is responsible for the early-time recovery of V_T (fig. 10), has been studied extensively by several groups [28–39]. It has been found to exhibit some rather unusual properties, the principal ones being the following: (1) It is highly dispersive in time, taking place over many decades in time following a radiation pulse. (2) It is universal in nature, meaning that changes in temperature, field, and thickness do not affect the shape or overall dispersion of the recovery curves, when plotted in terms of log-time. Changes in these variables affect only the time scale for the recovery. (3) The transport is field activated. (4) At temperatures above about 140 K, the transport has an Arrhenius-type temperature activation dependence, but below ~140 K, the transport essentially becomes thermally nonactivated. (5) The characteristic recovery time, or hole transit time, has a strong superlinear power-law dependence on oxide thickness.

Many of these features, such as the dispersion in time, universality, and superlinear thickness dependence, can be directly attributed to a wide distribution of transit times of the individual holes through the material. The wide distribution of transit times is a result of a broad distribution of individual (microscopic) event times which extend into the time range necessary for the fastest carriers to transit through the sample. In essence, while some carriers transit the sample very rapidly via a succession of rapid events (e.g., hops), other carriers are immobilized at some point for times on the order of or greater than the transit time of the fastest carriers. Such broad distributions of event

times can be easily envisioned in several simple situations: first, in hopping transport, small fluctuations (due to disorder) in either the intersite hopping distance or in activation energy, or even in bond angles, can produce large variations in the hopping transfer integrals and hence lead to large variations in hopping times; and second, for transport mediated by traps (multiple trapping), in which the carriers move via normal band conduction between trapping events, relatively small variations in the trap energy level can lead to a broad distribution of release times from the traps. These simple models are indicated schematically in figure 13.

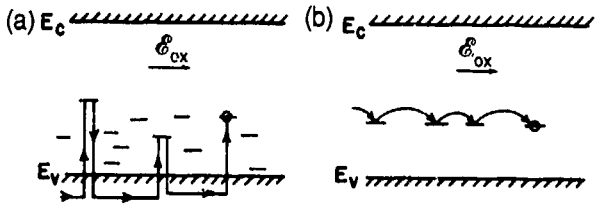

Figure 13. Schematic diagrams of two possible transport models which can lead to large dispersion in carrier transit times: (a) trap-modulated transport via valence band conduction, and (b) hopping transport via tunneling between localized states.

The best overall description of the experimental data seems to be provided by the hopping transport mechanism. Specifically, the available transport data on clean, hardened oxides, in which the short-term recovery is not masked by significant amounts of deep hole trapping near the SiO_2/Si interface, has been successfully described by a continuous-time-random-walk (CTRW) formalism originally developed by Montroll, Weiss, Scher, and others [40–43] and applied to hole transport in SiO_2 by McLean et al [28,31,32,36–39,44] and Hughes [29,30,35]. In essence, a response function (e.g., a radiation-induced voltage shift) may be characterized by the functional form $F(\alpha;t/t_\sigma)$, where α is a disorder parameter describing the amount of dispersion (or shape) of the response and is independent of T, E_{ox}, and d_{ox}. These parameters enter only in the characteristic time scale, $t_\sigma = t_\sigma(T, E_{ox}, d_{ox})$, for the response. (In practice, t_σ may be taken as the time that half recovery of the threshold voltage shift occurs.) Explicitly, for $T \gtrsim 140$ K, t_σ is given by

$$t_\sigma = t_\sigma^o (d_{ox}/a)^{1/\alpha} \exp[\Delta(E_{ox})/k_B T] , \qquad (6)$$

where t_σ^o is a constant, k_B is the Boltzmann constant, a is a hopping distance, and the field-dependent activation energy is

$$\Delta(E_{ox}) = \Delta_o - bE_{ox} , \qquad (7)$$

where b is a constant and Δ_o is the low field limit of $\Delta(E_{ox})$. For clean, hardened SiO_2, the parameter values appearing in equations (6) and (7) are $\alpha \cong 0.25$, a = 1 nm, Δ_o = 0.65 eV, b = 0.05 eV/MV/cm, and $t_\sigma^o \cong 10^{-22}$ s if the half-recovery time of a voltage shift is used as a measure of t_σ. Note that for α = 0.25, $t_\sigma \propto d_{ox}^4$, which indicates the strong superlinear thickness dependence referred to earlier. With these parameter values, the time to reach half-recovery for a 100-nm oxide at room temperature and for a 1-MV/cm field is $\sim 3 \times 10^{-4}$ s.

The specific intersite hopping transfer mechanism seems most likely to be small polaron-like hopping of the holes between localized, shallow trap states having a random spatial distribution but separated by an average distance of 1 nm. The term polaron refers to the situation where the charge carrier (hole in our case) strongly interacts with the surrounding medium, inducing a significant distortion of the lattice or atom network in the immediate vicinity of the carrier. This situation is also sometimes referred to as self-trapping of the carrier. As the carrier moves via hopping through the material, it carries the accompanying lattice distortion with it. The strongest evidence for the polaron hopping mechanism is the transition from thermally activated behavior above ~140 K to an essentially nonactivated transport at lower temperature. This transition—occurring at about a quarter of the Debye temperature—is a classic signature of polaron hopping [45–47]. We note, however, that the transport is still strongly field dependent in the low-temperature nonactivated regime.

Some of the salient features of hole transport are illustrated by the data sets shown in figures 14 and 15. Figure 14 shows the effect of temperature [36], and figure 15 the effect of oxide field [37]. These data are measurements of the flatband vol-

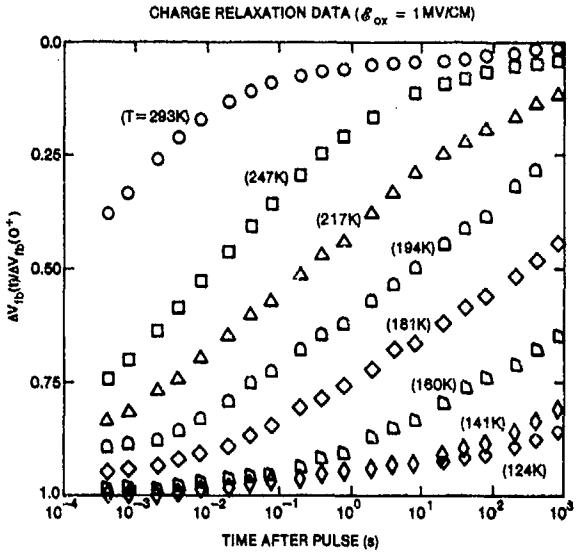

Figure 14. Normalized flatband voltage recovery data following pulsed 12-MeV LINAC electron irradiation of 96.5-nm oxide MOS capacitor under 1-MV/cm oxide field for series of temperatures between 124 and 293 K [36].

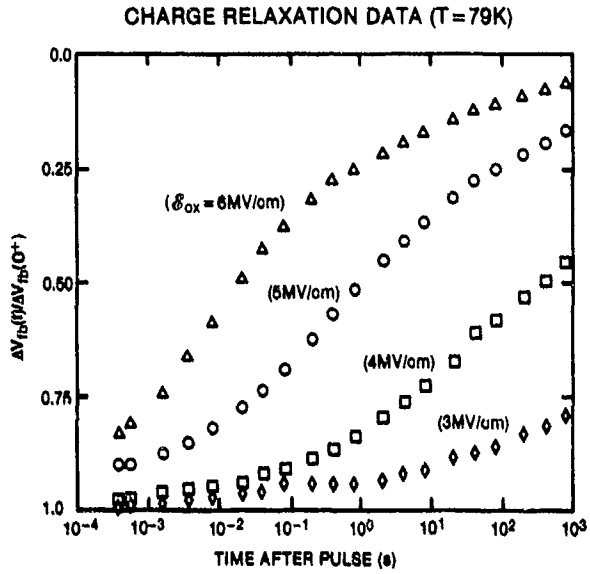

Figure 15. Normalized flatband voltage recovery data following pulsed LINAC electron-beam exposure for 96.5-nm oxide MOS capacitor at 80 K and for oxide fields from 3 to 6 MV/cm [37].

tage shift versus log-time from 10^{-4} to 10^{3} s following pulsed 12-MeV electron (LINAC) irradiation of MOS capacitors. The data in these figures are all normalized to the initial shifts, $\Delta V_{fb}(0^+)$, immediately after the radiation pulse. The initial shifts are not those at the earliest measurement ($\sim 10^{-4}$ s), but rather are the calculated shifts before any transport occurs. The actual values of $\Delta V_{fb}(0^+)$ vary with dose, field, and thickness as described in the previous subsection. The data are plotted in the negative direction because the voltage shifts are negative, indicative of net positive charge induced in the oxide layer. Figure 14 shows the response for a series of temperatures between 125 and 293 K at a single oxide field of 1 MV/cm. The strong temperature activation above 141 K is apparent; in fact, plotting the time, say, at which half-recovery occurs versus 1/T (Arrhenius-type plot) yields a straight line, the slope of which yields an activation energy of $\sim$0.60 eV. Figure 15 shows the response at a constant temperature of 79 K with oxide field as a parameter in the range from 3 to 6 MV/cm.

The large amount of time dispersion is apparent in both figures 14 and 15, with the recovery taking place over many decades in time (something like 8 to 10 decades from start to finish). The universal feature of the transport is also evident in the data: changes in an external parameter (temperature in fig. 14 and field in fig. 15) do not seem to have much effect on the shape of the recovery curves when plotted in log-time. Rather, the major effect of changes in these parameters is simply to produce a rigid translation of the curves along the log-time axis; that is, only the time scale for the transport is affected and not the amount of dispersion. In fact, if these data are replotted in time units scaled to a characteristic recovery time (e.g., half-recovery time), the data for different parameter values essentially trace out the same universal curve. This is shown in figure 16 for the temperature data of figure 14, where the data for all temperatures in terms of scaled time trace out a universal curve over ten or more decades in time. In several instances, data points from as many as five temperatures overlap to a considerable degree in the same region of scaled time. The solid curve in figure 16 is the calculated response based on the CTRW model for α = 0.25 [44], indicating good agreement overall of the model with the response data.

The almost complete recovery of ΔV_{fb} at late times and high temperatures in figure 14 indicates very little long-term, or permanent, trapping of holes in this particular sample—a trapping fraction of <2 percent is indicated by these data. Hence,

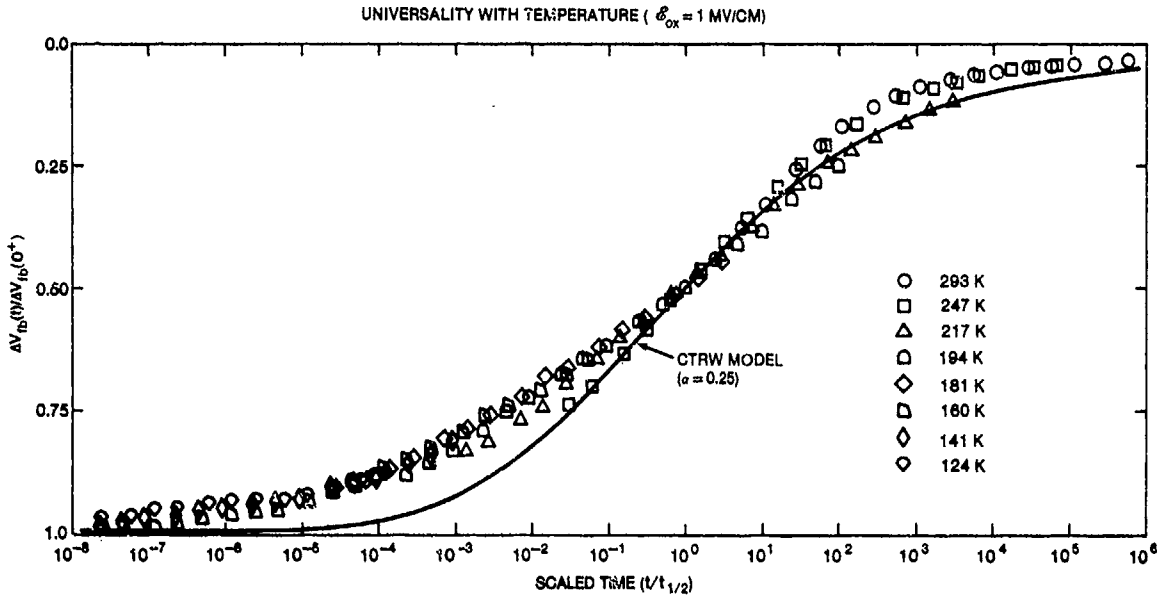

Figure 16. Normalized flatband voltage recovery data of figure 14 replotted with time scaled to half recovery time. Shows universality of response with respect to temperature. Solid curve is calculated CTRW model recovery for α = 0.25.

this particular oxide is a good (clean, radiation-hard) oxide in which to analyze the hole transport, not complicated by effects associated with deep hole traps. We caution the reader that the deep hole trapping fraction can vary greatly among different oxides, so care must be exercised when quantitatively characterizing hole transport properties if the trapping fraction is large (see sect. 3.3.3).

We see in figures 14 and 15 that little transport or recovery occurs at the lowest temperatures until relatively long times on the scale of the experiments. For example, at 80 K and for E_{ox} = 3 MV/cm, the recovery begins only after 10 s (fig. 15). In fact, for E_{ox} < 2 MV/cm, essentially no recovery takes place at 80 K for times of the order of thousands of seconds. The holes remain frozen in place very near their point of generation. This feature has been used in studies of the charge yield in SiO_2 [19,20,27]. It also has severe implications for the operation of SiO_2 MOS devices at cryogenic temperatures, if they are exposed to ionizing radiation. Indeed, there would be no short-term recovery of the devices, as is the case at room temperature (fig. 10); the threshold voltage shift would remain essentially at its maximum initial value for all practical times (see sect. 7.1 for further discussion of this point).

Finally, figure 17 shows the strong superlinear oxide thickness dependence of the recovery time as contained in equation (6). In this figure we show log-log plots of the recovery time versus oxide thickness for two sets of samples [38]: one set of MOS capacitor samples initially grown to a thickness of 98 nm and then etched back to several smaller thicknesses down to 41.3 nm, and another set of as-grown samples with various thicknesses between 21 and 98 nm. The relative displacement between the two plots is not significant, since the data for the two plots were obtained under different conditions. For the etched-back samples, the data were recorded at 79 K and 5 MV/cm, and the time for ΔV_{fb} to reach half recovery was used as a measure of the transit time. For the as-grown samples, the data were taken at 220 K and 1 MV/cm, and the time for ΔV_{fb} to reach 75-percent recovery was used as a measure of the transit time. (The 75-percent recovery point was used in this latter case in order to have a reliable horizontal cut through all the recovery curves.) The importance of figure 17 is that it shows that the log-recovery-time versus log-thickness data can be fit reasonably well by straight lines in both cases, with slopes of 4.2 and 4.0 for the etched-back and as-grown cases, respectively. These values agree very well with the prediction of a d_{ox}^4 dependence from equation (6)

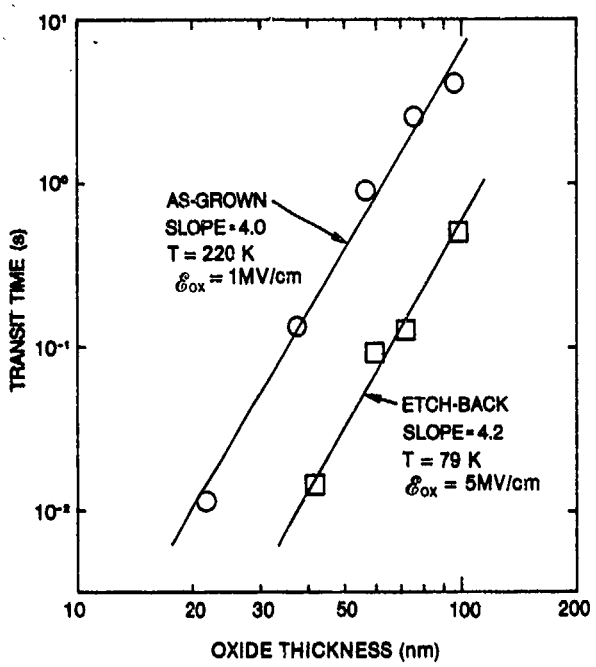

Figure 17. Log of recovery time versus oxide thickness for both etched-back and as-grown oxide MOS capacitors [38].

with $\alpha = 0.25$ for this oxide. A direct practical implication of these results is that thinning the gate oxide layer significantly reduces the short-term recovery times of radiation-induced threshold voltage shifts.

3.3.3 *Deep Hole Trapping and Annealing*

Following exposure to ionizing radiation and after the radiation-generated holes have had time to complete their transport through the oxide, MOS structures typically exhibit a negative voltage shift component, ΔV_{ot}, in their electrical characteristics (e.g., V_T, V_{fb}) that is not sensitive to silicon surface potential and that persists for hours to years. This long-lived radiation effect component is the most commonly observed form of radiation damage in MOS devices and is attributed to the long-term trapping of some fraction of the radiation-generated holes in the oxide layer within ~10 nm of the SiO_2/Si interface. This effect generally dominates other radiation damage processes in MOS structures, including negative charge (electron) trapping and interface-state buildup effects, unless specific device processing changes are made to alter the oxide and consequently reduce the hole trapping or enhance the other effects.

An important point made in the overview section (sect. 3.2) that is worth reiteration is the following: radiation effects involving interface phenomena in general (hole trapping and long-term annealing (removal) of trapped holes, interface trap buildup) are all highly dependant upon oxide processing. There can be orders of magnitude variation in the different effects among oxides of varying processing histories. This is in contrast to the bulk phenomena of charge pair generation, recombination, and hole transport, in which remarkably little variation is observed among thermal oxides of greatly different processing. Consequently, in terms of minimizing long-term damage effects associated with the interface phenomena, proper control of oxide (circuit) processing has been and continues to be a major thrust of radiation hardening efforts.

The effect of processing on the fraction of holes which undergoes deep, long-lived trapping is illustrated by the data shown in figure 18 [48]. Here, the threshold voltage shifts versus total dose are plotted for two n-channel devices where the radiation hardness was varied by changing the high-temperature processing. The dose rate was 8×10^4 rad per minute and the measurements were obtained within 10 minutes of the exposure at each dose. Clearly, at each dose there is roughly an order of magnitude difference in the threshold voltage shift, which in turn is most likely due to an order of magnitude difference in the number of hole

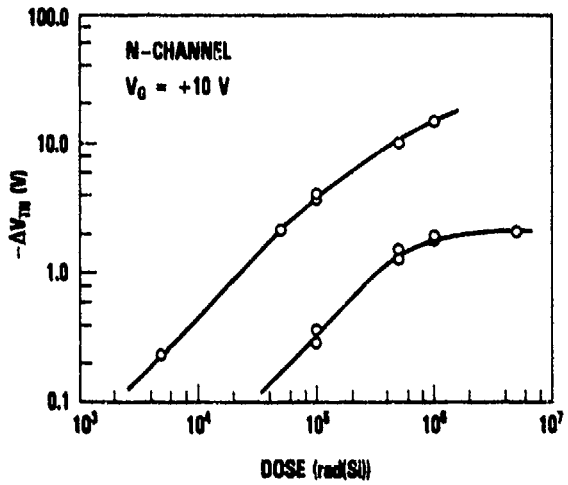

Figure 18. Effect of processing variation on hole trapping: threshold voltage shift versus total dose for two n-channel MOSFET's which received different high-temperature processing [48].

traps present in the two oxides. In general, the fraction of radiation-generated holes that undergoes long-term deep trapping has been found to vary from as little as 1 or 2 percent for a good, hardened oxide, to the order of 10 to 20 percent for good-quality commercial oxides, and to as much as 50 to 70 percent in very soft commercial oxides.

Evidence concerning the location of the trapped holes is contained in figure 19 which shows long-term ΔV_{fb} measured in MOS capacitors on n-type silicon irradiated to 1 Mrad(SiO_2) at gate voltages from −10 to 10 V [49]. The negative ΔV_{fb} includes contributions from both the oxide trapped charge and radiation-generated interface states, but the response is dominated by the trapped hole component. The shift under positive V_g is much greater than that observed at equivalent negative V_g. From similar data, Zaininger [50] first in 1966 inferred that the positive oxide charge must be fairly mobile since it apparently moves rapidly to and is trapped near the SiO_2/Si interface under positive bias and moves toward the gate under negative bias. If bulk trapping were involved rather than trapping near the interfaces, the shifts for positive and negative polarity for the same field magnitude would not differ nearly as much as data such as figure 19 indicate. A great amount of other work, including oxide etch-back analysis [51–54], internal photoemission spectroscopy [55,56], and inferences from the postirradiation buildup [57–59] and annealing [60] of the trapped charge all indicate

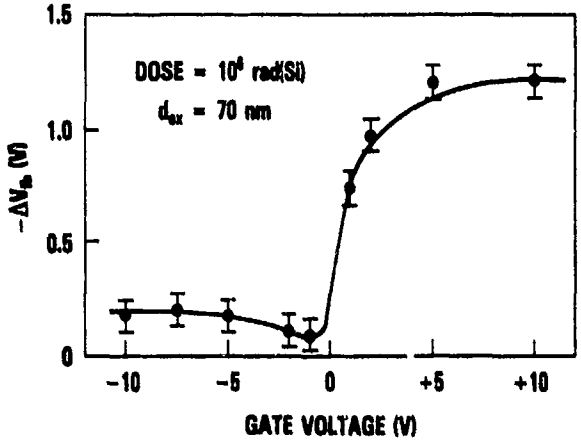

Figure 19. Bias dependence of radiation-induced voltage shift: radiation-induced flatband voltage shift versus gate voltage for MOS capacitor following 1-Mrad(SiO_2) exposure [49].

that the location of the long-term trapped holes under positive gate bias is generally within ~10 nm of the SiO_2/Si interface.

In a critical experiment which first demonstrated that radiation-generated holes are responsible for the positive oxide charging, Powell and Derbenwick [53] used vacuum ultraviolet (VUV) light to probe charge generation in MOS structures. Using MOS capacitors with semitransparent gold gate electrodes and 10-eV light that was absorbed and generated electron/hole pairs in the first 10 nm of the oxide near the gate, they found that positive charge appeared at the SiO_2/Si interface—well out of range of the VUV photons—under positive gate bias, while no oxide charging took place under negative bias. These results and other effects they observed indicated clearly that holes are mobile in SiO_2 and are readily trapped near the SiO_2/Si interface. Later work on charge generation and transport by many investigators, as described in section 3.3.2, confirmed the role of the trapped holes as the principal source of oxide charging in MOS structures with thermal oxides.

Besides the location of the trapped holes in the oxide within ~10 nm of the SiO_2/Si interface and the fact that the hole trapping fraction is highly dependent on processing, other pertinent pieces of information concerning the characteristics of the hole traps—obtained from the work of many investigators over the years—include the following: (1) The number density of the hole traps typically lies in the range from 10^{18} to 10^{19} cm^{-3} [51,61–63], with the corresponding areal density range being from 10^{12} to 10^{13} cm^{-2}. (2) The cross section for hole trapping is usually found to be around 5×10^{-14} cm^2 for a 1-MV/cm oxide field [62,63]. (3) The cross section decreases as $E_{ox}^{-1/2}$ for fields above 1 MV/cm in magnitude [64–66]. For the data shown in figure 19, the increase in ΔV_{fb} as the bias is increased from zero is attributed to the increased yield of holes with increasing field, but the flattening of the curve for larger positive bias (and sometimes a turn-around has been observed) is probably due to the decreasing cross section for hole capture as the field increases above 1 MV/cm. (4) It is commonly observed [20,58,59,61,63] that the total number of trapped holes, N_{ot}, tends to a saturation level in the 1- to 10-Mrad dose range. Depending on specific circumstances, this is due to one or more

operating factors, including trap filling (hard saturation), large space charge effects to the point of field reversal in some regions of the oxide layer, and recombination of the trapped holes with radiation-generated electrons moving through the trapped hole distribution. (5) There are several different experimental indications [54,60,67,68] that the energy level associated with most (but perhaps not all) of the deep hole traps is about 3 eV above the valence-band edge of SiO_2. (6) Based upon an increasing accumulation of electron spin resonance (ESR) spectroscopy data [67,69,70], the microscopic structure of the trapped holes seems to be the so-called E_1' center, which is a trivalent silicon defect associated with an oxygen vacancy in the SiO_2 structure [71-73].

In essence, present evidence suggests the following model for the hole trapping process. The SiO_2/Si interface region of MOS structures is characterized by high local strain [74] and a deficiency of oxygen atoms which result in a number of strained Si-Si bonds (instead of normal Si-O-Si bonding configurations). A hole encountering such a strained bond may break the bond and recombine with one of the bonding electrons. The resulting positively charged structure relaxes to the E_1' center configuration, with one of the Si atoms retaining the remaining electron from the broken bond and the positive charge residing with the other trivalent Si atom. Figure 20 shows a simple schematic [75] of the trapping process.

Let us now address the question of the long-term stability of the deeply trapped holes. In fact, the holes in deep traps in the SiO_2 layer of an MOS structure after irradiation are not truly "permanently" trapped. Instead, they are observed to disappear from the oxide over times from milliseconds to years. This discharge of the trapped holes, as commonly observed at or near room temperature, is the major contributor to the so-called "long-term annealing" of radiation damage in MOS devices. The annealing of the trapped holes has two manifestations that may reflect different hole removal processes. The first is the slow bias-dependent recovery of ΔV_{ot} typically observed at normal device operating temperatures (−55° to 125°C, for instance). Aspects of this process have been described through a tunneling model. The second is the relatively rapid and strongly temperature-dependent thermal detrapping or recombination of the holes observed when MOS structures are deliberately subjected to thermal annealing cycles at elevated temperatures (150° to 350°C). This process has been described through a thermal detrapping model. We restrict our attention here to just the "tunnel anneal" process important at normal operating temperatures.

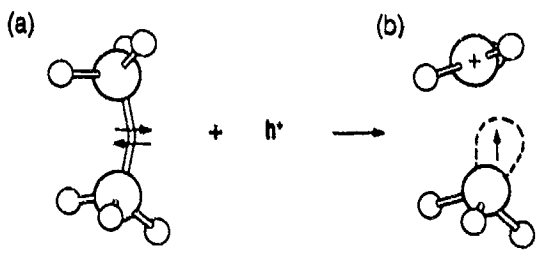

Figure 20. Schematic of hole trapping process indicating (a) initial strained Si-Si bond (oxygen vacancy) and (b) relaxed E_1' center configuration after hole capture [75].

Figure 21 presents typical results for the time dependence of hole annealing at room temperature. Midgap voltage shift, ΔV_{mg} ($\sim\Delta V_{ot}$—see sect. 3.4.4), is plotted as a function of time after irradiation for three n-channel MOSFET samples with different dry oxide processing [60]. The discharge of the trapped holes is roughly linear in log(t). This behavior is a hallmark of the hole anneal process and has been used in convolution schemes for predicting the response of MOS devices under low-dose-rate irradiation conditions [48,76,77]. We note that the three devices shown in figure 21 have been irradiated to different doses to achieve roughly comparable shifts for the first measurements (20 krad for the soft samples, 90 krad for the intermediate samples, and 1 Mrad for the hard samples).

Several investigators have suggested a tunneling process to explain the log(t) recovery and other aspects of hole annealing in MOS structures [38,60,68,78,79]. These models assume that electrons from the silicon substrate tunnel to, and recombine with, the trapped holes in the distribution of traps near the SiO_2/Si interface, as illustrated by the schematic diagrams in figure 22. (Equivalently, one can think of the holes tunneling from the traps to the silicon valence band.) As a consequence of the exponential decay of the tun-

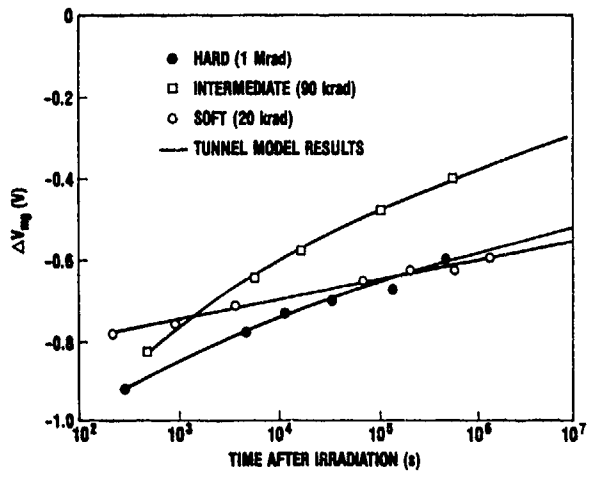

Figure 21. Long-term annealing data for three MOSFET's of varying radiation hardness. Devices received indicated doses to produce comparable initial shifts [60].

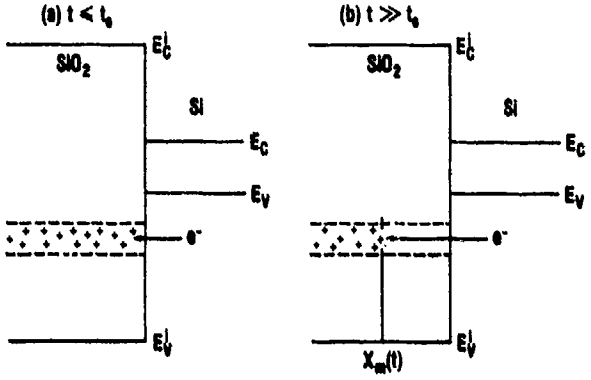

Figure 22. Schematic of trapped hole removal by electron tunneling from Si substrate.

neling probability with distance into the SiO_2, at a given time t the hole traps are emptying at a depth $X_m(t)$ from the silicon that increases logarithmically with time [80,81]:

$$X_m(t) = (1/2\beta)\ell n(t/t_0), \quad (8)$$

where β is the tunneling barrier height parameter and t_0 is the time scale parameter. For distances only slightly greater than X_m, essentially all the traps remain full at time t; for distances only slightly less than X_m, essentially all the traps have been emptied by tunneling. Thus, hole removal proceeds via a "tunneling front" that moves into the oxide with a "velocity" $\Delta X_m = 1.15/\beta$ per decade in time. (ΔX_m has been found to be about 0.2 nm per decade [68,79].) For $X_m \ll d_{ox}$ and a uniform distribution of traps in the oxide within tunneling distance of the silicon, the resulting trapped charge loss (and hence the decrease in ΔV_{ot}) at a given time due to the tunnel anneal is then proportional to X_m; i.e., ΔV_{ot} decreases as $\ell n(t)$. Thus the tunneling model explains qualitatively the observed approximate log(t) anneal of the trapped holes.

This simple model fails to describe the observed responses in detail. As shown in figure 21, the annealing curves are not completely linear; the rate of annealing tends to decrease with time. This is clearly to be expected, since the rate of annealing should approach zero as the amount of charge left to be removed (remaining ΔV_{ot}) approaches zero. The simple log(t) anneal arises from the assumption that the trapped holes are distributed uniformly into the oxide from the silicon interface. In reality, the hole trap density generally falls off with distance from the silicon. Oldham et al [60] assumed an exponential falloff in occupied hole trap density from the interface and incorporated this form into the appropriate expressions from tunneling theory; this yielded the solid line fits to the data as shown in figure 21. An important conclusion from this analysis was that the trapped hole distribution lies close to the SiO_2/Si interface in hard oxides (i.e., the distribution falls off relatively sharply from the interface), whereas it extends deeper into the oxide bulk for the soft oxides. This is apparently related to the size of the strained, oxygen-deficient region near the interface, a property highly dependent upon processing conditions. The fact that the tunneling rate depends exponentially on tunneling distance then explains the many orders variation in long-term annealing rates among different oxides [82].

Additional aspects of the tunnel anneal process are its dependencies upon temperature and oxide field. The temperature effect seems to be adequately explained [68] by a linear temperature dependence of the trap energy levels, $E_t(T) = E_t^o - bT$, where $E_t^o = 3.6$ eV and $b = 2.0$ meV/K. The electric field dependence arises from the field modification of the tunneling potential barrier height; a positive electric field has the effect of lowering the

barrier to tunneling and thereby increases the rate of annealing.

3.3.4 *Radiation-Induced Interface Traps*

Interface traps (N_{it}) are localized electronic states located at or very near the SiO_2/Si interface, having their energy levels distributed within the Si bandgap. They can exchange charge with the Si conduction and valence bands. Their occupancy, or charge state, depends upon the position of the Fermi level at the interface, i.e., upon the value of the surface potential. The major effects of N_{it} in MOS systems are to (1) produce distortions in device characteristics (e.g., C-V_g or I-V_g) as the gate bias is varied; (2) shift the threshold voltage due to the net interface trapped charge at the turn-on or inversion point; and (3) introduce additional Coulomb scattering centers for carriers moving in the surface channel of a MOSFET which degrade the carrier mobilities. Before irradiation, the areal density of interface traps in good modern devices is $\lesssim 10^{10}$ cm^{-2}, a density such that N_{it} effects normally are not much of a problem.

Upon irradiation, however, interface traps can build up to a significant level, resulting in discernible effects in devices. As mentioned in section 3.2, in general two components of radiation-induced interface traps (ΔN_{it}) have been observed, one a prompt component present at the earliest measurements following an irradiation and the other a time-dependent component which can continue building up for thousands of seconds. The relative ratio of the two components can vary greatly, with one or the other dominating in a particular system. As a rather loose general statement, the delayed time-dependent ΔN_{it} seems to dominate in metal (aluminum) gate devices [83–89], prompt ΔN_{it} dominates in thick, steam oxides (as used as field oxides) [90,91], and both components seem to be present in more or less comparable amounts in the polysilicon gate devices [92] that are more representative of present-day technology.

An example illustrating the effect of the time-dependent buildup of N_{it} is shown in figure 23, which shows C-V traces of an aluminum-gate dry oxide MOS capacitor both before irradiation and for a series of times from 0.04 to 400 s following

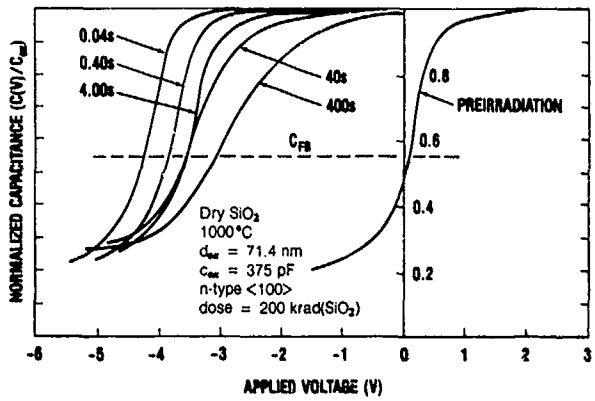

Figure 23. High-frequency 1-MHz C-V curves of MOS Al-gate capacitor at several times following pulsed electron-beam irradiation [83].

pulsed 200-krad(SiO_2) LINAC electron beam exposure [83]. At the first measurement following irradiation (0.04 s), the C-V curve is simply shifted along the negative voltage axis without discernible change in its shape compared to the preirradiation trace, indicative simply of positive charge being induced in the oxide. The next few curves (at 0.4 and 4.0 s) show a rigid shift back in the positive voltage direction with little change in shape because of a combination of the tail end of the hole transport process and deep trapped hole annealing. However, between 4.0 and 40 s a significant change or stretchout in the shape of the C-V trace occurs, and the stretchout becomes even greater at 400 s. This distortion is directly attributed to the delayed buildup of radiation-induced N_{it}.

Figure 24 shows the time-dependent buildup of interface trap density (for states with energies between midgap and inversion) for Al-gate wet oxide capacitors for a series of oxide fields between 1 and 6 MV/cm, from 2 to almost 10^5 s following pulsed LINAC irradiation [84]. Note that the final N_{it} levels in this case are almost solely due to the time-dependent buildup process. There is obviously a strong field dependence on both the rate of buildup and the final value of N_{it}. For all fields, the buildup apparently begins on the order of seconds (the point at 1 s on figure 24 is also the preirradiation N_{it} value), continuing for several hundred seconds at the highest field (6 MV/cm) before leveling off. For the lower field values (1 and 2 MV/cm) the generation rate is much lower, but N_{it} is still seen to be increasing even at the latest measurement times.

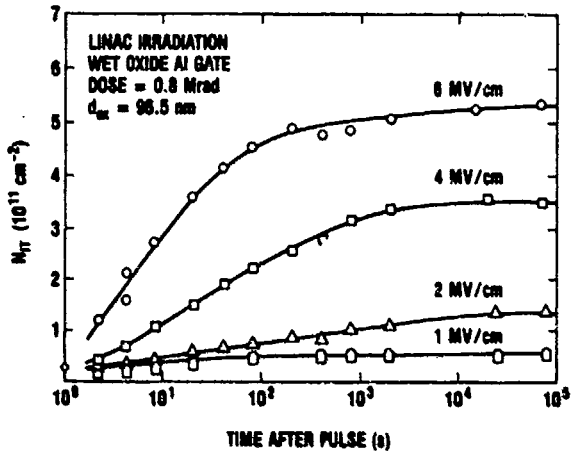

Figure 24. Integrated interface trap density between midgap and inversion surface potentials as function of time following pulsed electron-beam exposure for several values of oxide field [84].

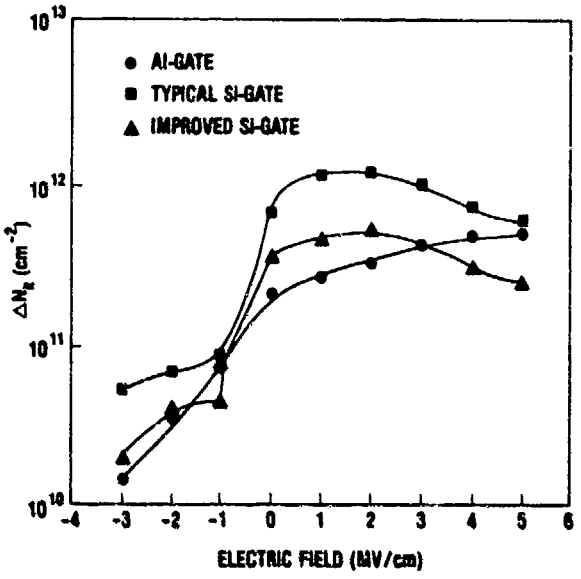

Figure 25. Oxide field dependence of radiation-induced interface trap buildup following 1-Mrad(SiO_2) irradiation in three MOS capacitors having different gate structures [93].

In figure 25, the field dependence of the radiation-induced interface trap buildup is compared for three types of MOS capacitors [93]: aluminum gate, polysilicon-gate samples receiving "typical Si-gate processing," and special "hardened" Si-gate capacitors. Plotted in the figure is the increase in interface trap density between midgap and inversion following 1-Mrad(SiO_2) irradiation as a function of oxide electric field for both positive and negative polarities. The ΔN_{it} for the Si-gate samples contained both prompt and delayed time-dependent components. In all three samples, the ΔN_{it} is much less under negative bias polarity than positive polarity (note the log scale for ΔN_{it}). The N_{it} buildup for the Al-gate capacitors increases with increasing positive field, in general agreement with the earlier data of figure 24. However, the Si-gate capacitors exhibit a rapid increase in N_{it} production for positive fields up to ~1 MV/cm, but which peaks in the range from 1 to 2 MV/cm and then drops off somewhat at higher fields. It is clear that there are some qualitative differences in the mechanisms of N_{it} buildup in Al-gate and Si-gate systems. These differences are not understood at the present time, although they are likely to be associated with differences in the nature of the generation mechanisms for the prompt and delayed time-dependent components. Note also in figure 25 that for normal operating fields of 1 to 2 MV/cm, the ΔN_{it} for the typical commercial Si-gate process is about five times greater than that for the Al-gate samples. This increased ΔN_{it} is commonly observed for Si-gate technologies. The magnitude of the interface trap production in the "improved" Si-gate process in the figure is comparable to that in the Al-gate process.

We have attempted with the discussion thus far to illustrate some of the major observations that have been made concerning the buildup of radiation-induced interface traps, such as the existence of prompt and delayed time-dependent components, the strong bias polarity effect, the dependence on the magnitude for positive fields, and the strong dependence on oxide processing including the differences between aluminum gate and polysilicon gate structures. At the present time, the precise mechanisms responsible for the interface trap buildup are not well understood, and in fact the general area of SiO_2/Si interface traps and their generation under various stresses (radiation, high electric fields, hot carrier injection, etc) is a complex subject of intense current interest and debate. It is beyond the scope of the present discussion to attempt a review of this area and particularly to sort it out. We conclude this section simply by noting without discussion some other observations that have been made concerning the characteristics of radiation-induced interface traps and factors that may be contributing to their buildup.

(1) There is much evidence that N_{it} buildup is associated with the hole transport, trapping, and annealing processes [83–89,94,95].

(2) There may also be a strong correlation of the buildup with hydrogen or water content of the oxide, and in fact arguments have been made that the time-dependent buildup is associated with the release (during the hole transport phase) and diffusion of hydrogen, or a water-related species, from the oxide bulk to the interface [96–101].

(3) The amount of interfacial strain—which is highly variable with processing—seems to be an important factor [74,89,102–104].

(4) The rate of buildup of the time-dependent N_{it} component increases with temperature; however, the final density at long times is essentially independent of temperature [84,86,99].

(5) Annealing of interface traps has not been observed at normal operating temperatures [84,86]; significant annealing occurs only for $T \gtrsim 150$°C [105].

(6) In many cases, a sublinear dependence of ΔN_{it} on dose ($\sim D^{2/3}$) has been observed, particularly for the delayed time-dependent component [84,87,106,107].

(7) The magnitude of N_{it} buildup is generally observed to decrease with decreasing oxide thickness [38,106,108–111].

(8) The energy distributions of radiation-induced interface traps are commonly observed to be U-shaped, with a minimum near midgap and rising toward both the conduction and valence band edges [83,84,112]. However, there is debate on the existence of intermediate structures, such as peaks [113].

(9) The interface traps seem to be amphoteric in nature, that is, they have a net negative charge (acceptor-like) when the Fermi level (E_F) at the surface is in the top half of the Si bandgap; they have net positive charge (donor-like) when E_F is in the bottom half of the bandgap; and they are charge neutral when E_F is near midgap [113–116]. This latter statement is important for charge separation (between ΔV_{ot} and ΔV_{it}) techniques, as is discussed in section 3.4.

(10) The evidence originating from ESR spectroscopy indicates that (at least for a large fraction) the microscopic structure of the interface trap is that of an Si atom at the interface back-bonded to three Si atoms on the silicon side and having a single broken dangling bond extending into the SiO_2. This is called the P_b center by the ESR spectroscopists [117]. The amphoteric nature of the states is attributed to the broken dangling bond containing 0, 1, or 2 electrons, with the charge state of the P_b center as a whole therefore being positive, neutral, or negative, respectively [113, 115,118,119]. We should qualify these statements, however, to the extent that most of the ESR work to date has been done on (111) Si interfaces to obtain the maximum ESR signals; not much has been done on the technologically more important (100) Si interface. In fact, there is much active discussion at present as to whether the midgap charge neutrality condition actually holds for the (100) Si interface (see sect. 3.4.4).

(11) Since the radiation-induced interface traps lie at or very near the SiO_2/Si interface, they—especially when charged—introduce additional scattering centers for the conducting channel carriers in MOSFET's; these are in addition to the normal scattering from surface roughness, ionized dopants or other impurities in the surface region, and lattice vibrations (phonons). As a consequence, ΔN_{it} can lead to reduction of the carrier mobilities and hence to degradation in the transconductance [120]. This is normally a secondary effect in the low to moderate dose range ($\lesssim 1$ Mrad), but can become a serious factor in circuit degradation or failure at high dose levels by causing a significant decrease in circuit speed.

3.4 Implications for Radiation Testing, Hardness Assurance, and Prediction

We have emphasized the complex time history of the radiation response of MOS systems occurring from microseconds to the order of years. This complex response originates from the variety of distinct basic processes contributing to the response: initial hole yield, hole transport, deep hole trapping and annealing, and the buildup of interface traps. Characteristic time regimes are associated with each process; these are generally functions of temperature, field, oxide thickness, etc, and may overlap with each other. Figure 26 is another version of the schematic time-dependent

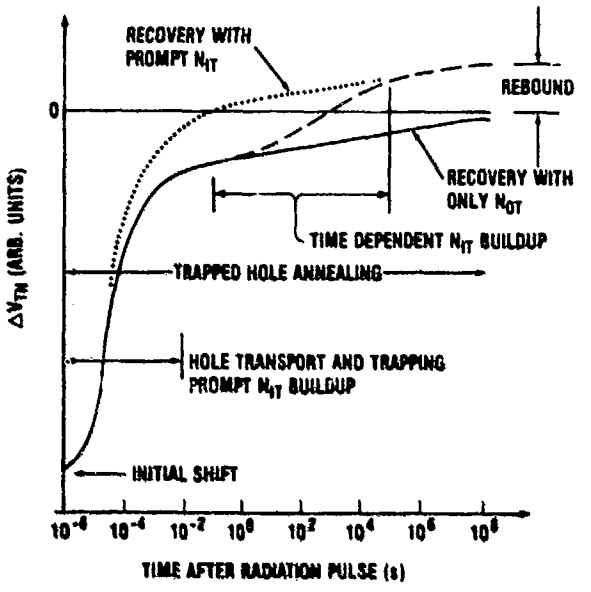

Figure 26. Schematic time-dependent threshold-voltage recovery of n-channel MOSFET following pulsed irradiation, indicating characteristic room-temperature time regimes associated with various basic physical processes, as well as various possible long-term responses.

threshold-voltage recovery of an n-channel MOSFET, but with the various characteristic time regimes (at room temperature) explicitly noted, as well as the various long-term behaviors illustrated: recovery without ΔN_{it}, with prompt ΔN_{it}, and with time-dependent ΔN_{it} buildup. Another very significant complication is the large variation among different oxides in the magnitudes of phenomena associated with the SiO_2/Si interface, including in particular large relative variations. These variations arise mainly from differences in oxide processing. All these factors greatly complicate issues dealing with radiation testing, hardness assurance, and response prediction of circuits in potential threat environments.

It is obvious upon a little reflection that it is important to bear in mind the specific radiation environment and the time regimes of operational interest when attempting to assess the hardness level of a particular circuit. In many cases, one must perform radiation hardness testing in some practically dictated time regimes (as well as dose and dose rate regimes), when the actual operational use in the anticipated threat environment may be for entirely different time, dose, and dose rate regimes. Because of the complex time response, extrapolations of test data to operational situations are nontrivial. Stated very simply, one cannot generally place a circuit in a radiation test source (e.g., Co^{60}), take it out, and at some one later time make a measurement of, say, threshold voltage shift and then use this one data point to assess the hardness level of the circuit for some other radiation environment and time regime of operational use.

Over the past few years, there have been (and continue to be) much practical interest and much effort by a number of workers in the community in trying to arrive at useful and sensible testing and prediction procedures for MOS circuits. Our purpose here is not to delve into this subject area, but rather simply to point out some of the issues and problems originating from the basic mechanisms of the response. In this section, we briefly discuss several selected but important issues of ongoing concern, including superrecovery or the rebound effect, apparent dose-rate-dependent effects, trapped hole saturation effects, charge separation techniques, classification of oxide response, and dose enhancement considerations. For the most part, we will assume that we are dealing with sufficiently long time scales ($\gtrsim$1 s) such that the hole transport phase can be considered finished and only the effects relating to ΔN_{ot} and ΔN_{it} need be considered.

3.4.1 *Superrecovery (Rebound Effect)*

We have noted that deeply trapped holes (ΔN_{ot}) can anneal out over very long periods of time. We also mentioned that interface traps (ΔN_{it}) have not been observed to anneal out at normal operating temperatures. Furthermore, ΔN_{it} may continue to build up over time. Since for an n-channel device under positive bias the interface traps contribute net negative charge and therefore a positive contribution (ΔV_{it}) to the threshold voltage, these factors taken together may lead to the phenomenon called superrecovery [121] or rebound [122]. Namely, at the end of an irradiation, the threshold voltage for an n-channel MOSFET is generally shifted negatively, since the (negative) voltage contribution ΔV_{ot} from the trapped holes usually dominates ΔV_{it}, at least for doses up to 1 Mrad or so. However, as annealing of the trapped holes occurs and/or further buildup of the interface trapped charge occurs, the

threshold voltage may actually anneal back to and past its initial preirradiation value; i.e., ΔV_T may go positive at some late time after cessation of the radiation. If the positive voltage excursion is sufficiently large, circuit failure may result from this effect as well as for a negative excursion.

The rebound effect is clearly demonstrated by the data shown in figure 27 [122]. Here, the threshold voltage of a polysilicon-gate n-channel MOSFET, as well as the separate components ΔV_{it} and ΔV_{ot}, is plotted against time after exposure to 1-Mrad Co^{60} irradiation, which is completed in 1 hour. A gate bias of +10 V was maintained during both irradiation and the anneal time. Data for two temperatures are shown, for 25°C and for 125°C (which accelerates the rate of hole annealing). At neither temperature is there observed any annealing of ΔV_{it}, but rather some slight increase in ΔV_{it} after cessation of the irradiation is discernible. The important point, of course, is that V_T, which initially at the end of the irradiation is shifted negatively by about a volt, returns in the positive direction far past its preirradiation value. In fact, after 100 hours of anneal at 125°C, ΔV_{ot} is completely annealed, leaving a final positive shift in V_T of +2.5 V, which is due entirely to interface trapped charge (most of which was already present at the end of irradiation).

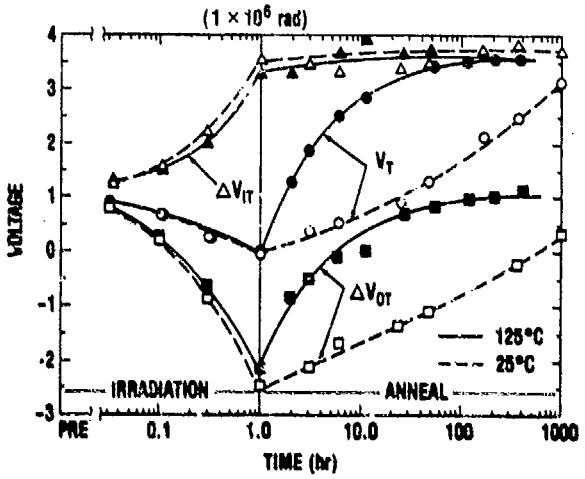

Figure 27. Threshold voltage shift of n-channel MOS transistor during irradiation and anneal with V_T separated into shifts due to interface trapped charge (ΔV_{it}) and oxide trapped charge (ΔV_{ot}). Long-term response illustrates rebound effect [122].

There are some interesting possibilities associated with this effect. For example, a device may initially be in failure at the end of an irradiation because of a sufficiently large negative voltage shift, and then as the trapped holes anneal, the device may begin operating normally at some time and continue operating until the device fails again from too great a positive threshold voltage excursion. We may also note in this regard that some hardening schemes in the past have attempted to rely on the compensation of trapped positive (hole) charge by net negative interface trapped charge. However, this type of hardening fix is risky at best, because utmost control must be maintained over the oxide processing to avoid too much radiation-induced N_{it} and consequently failure by rebound at long times. Such careful control of the processing is usually not possible in the long run for production lines. The optimum hardening approach is to minimize both ΔN_{ot} and ΔN_{it} [93].

3.4.2 Apparent Dose Rate Effects

A related problem area is that of an apparent dose rate effect on device response. That is, measurements of device response (e.g., ΔV_T) at the end of irradiation to a fixed total dose but delivered at different dose rates usually will show different results. This is clearly a result of the complex time history of the response in which, for example, different amounts of trapped hole annealing will occur during irradiation for different exposure times (to the same dose). To deal with this problem, resort has been made in the past to the techniques of linear response theory. This type of analysis is valid as long as one is dealing with systems whose response is linear in dose. If one knows the impulse response function, $\Delta V_R(t)$, say the threshold voltage response to an infinitesimally short irradiation pulse, then the general response to an arbitrary irradiation described by the dose rate function $\dot{\gamma}(t)$ may be obtained through the convolution integral

$$\Delta V_T(t) = \int_0^t dt' \, \dot{\gamma}(t') \, \Delta V_R(t - t'). \qquad (9)$$

A simple example for which this technique has been applied [48,76,77] is that for trapped hole annealing that is linear in log-time.

A rather spectacular example of an apparent dose rate effect whose origins are similar to the rebound effect is shown in figure 28 [121] in which the dose necessary for failure of an MOS device is plotted versus dose rate. The peak that occurs in this figure is simply that dose rate (~1 rad(Si)/s in this case) at which an essentially exact balance is achieved between positive charge buildup (deep hole trapping) on one hand, and the compensating effects of hole anneal and negative interface trapped charge buildup on the other hand. For lower dose rate values than the critical one to maintain balance, sufficient hole annealing occurs that the negative interface trapped charge wins out, resulting in eventual device failure by positive threshold shift excursion. At higher dose rates, the introduction of additional hole trapping dominates, and the device fails at a dose for which a sufficient negative threshold voltage shift is exceeded. This failure usually occurs at a lower total dose because n-channel devices can tolerate less of a negative ΔV_T shift than of a positive one. In any case, the point is that if one were to perform a simple radiation test measurement with a dose rate that just happens to be close to the critical dose rate for charge buildup balance, one might be led to conclude that a circuit is fairly hard (to over 100 krad for the example in fig. 28), whereas in reality the device would fail at much lower total-dose levels if either higher or lower dose rates are used.

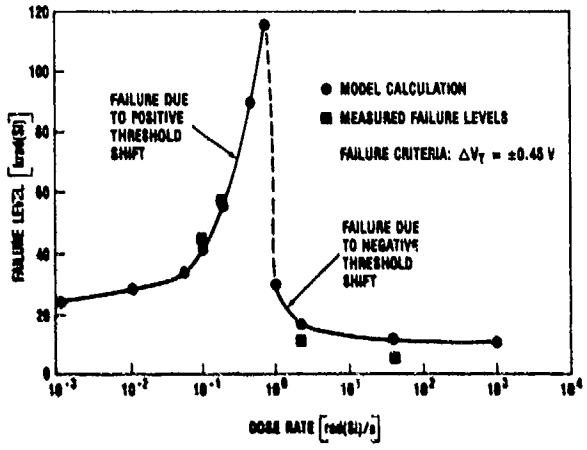

Figure 28. Dependence of circuit total-dose failure level on dose rate, indicating failure due to positive ΔV_T at low dose rate and to negative ΔV_T at high dose rate [121].

3.4.3 *Nonlinear Effects; Trapped Hole Saturation*

In the previous subsection, we mentioned that apparent dose rate effects such as varying amounts of trapped hole anneal during irradiation exposure can sometimes be handled with the convolution integrals of linear response theory. This approach is valid as long as the system response is linear in dose. Unfortunately, this is not always the case for situations of practical interest. For example, the number of trapped holes ΔN_{ot} tends to saturate for moderate to large dose rates at doses in the range from 1 to 10 Mrad(SiO_2) [20,58,59,61,63]. This saturation may be due to one or more factors, including hard saturation due to trap filling, space charge effects, or a balance between hole trapping and hole removal through tunnel anneal or recombination with radiation-induced electrons. An example of such an effect is illustrated by figure 29, in which the threshold voltages for n- and p-channel MOSFET's are shown plotted versus total ionizing dose [5]. The threshold voltage for the n-channel device first shifts negatively as the positive charge buildup due to trapped holes dominates the response. But at a dose $\gtrsim$1 Mrad, a turnaround is observed with V_T shifting back in the positive direction at increasing dose levels. This turnaround behavior is due to saturation of the trapped hole density, while at the same time the interface trapped

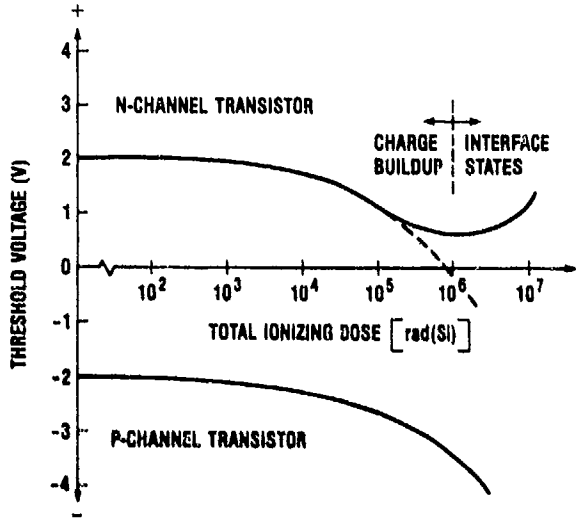

Figure 29. Threshold voltage versus total dose in irradiated n- and p-channel MOSFET's, illustrating effect of hole trapping saturation and continued interface trap buildup in n-channel device.

charge (negative for n-channel) continues to increase. For the p-channel device under negative gate bias, the interface states also contribute net positive charge, and there is a continued negative shift with dose in its threshold voltage.

Other nonlinear effects have been reported, such as the sublinear dose dependence ($\sim D^{2/3}$) of the delayed time-dependent buildup of ΔN_{it} [84,86,106,107]. There are also recent observations of an increasing rate of N_{it} buildup at high doses, or maybe even a threshold dose level for N_{it} production in some cases [82]. The whole issue of nonlinear effects lies beyond the scope of this discussion, but it is worthwhile to know that such effects exist and may be important factors at times.

3.4.4 Charge Separation Techniques

Recall from equation (2) that the radiation-induced threshold voltage shift can be written as the sum of the contributions from the oxide trapped charge and interface trapped charge

$$\Delta V_T = \Delta V_{ot} + \Delta V_{it} . \tag{10}$$

(We are neglecting ΔV_{st} here, as we are assuming sufficiently late times that the short-term recovery due to hole transport is over.) Now, because of the different time behavior of ΔN_{ot} and ΔN_{it}, as well as the fact that their magnitudes (including their relative ratio) may vary greatly among different oxides, it is clear that in order to perform sensible radiation testing one must be able to experimentally decompose ΔV_T into its separate components (as for the data shown in fig. 27). Although still somewhat controversial, most of the charge separation techniques that have come into practical use recently are based on the assumption of net charge neutrality of ΔN_{it} at the midgap voltage, i.e., the value of applied bias such that the Fermi level at the SiO_2/Si interface is at the midpoint of the Si bandgap. By definition the oxide trapped charge does not change its occupancy or charge state as the bias varies. (For ΔN_{ot} alone, device characteristics undergo a rigid, uniform translation along the negative voltage axis by an amount ΔV_{ot}.) Therefore, with the assumption of midgap neutrality of ΔN_{it}, the radiation-induced voltage shift (ΔV_{mg}) of a device characteristic (C-V_g, subthreshold I_D-V_g) at the midgap potential can be attributed solely to the oxide trapped charge:

$$\Delta V_{mg} = -q\Delta N_{ot}/C_{ox} = \Delta V_{ot} . \tag{11}$$

Hence, from the two measurements, ΔV_{mg} and ΔV_T, one can effect the charge separation. Combining equations (10) and (11), one has

$$\Delta V_{it} = -\Delta Q_{it}/C_{ox} = \Delta V_T - \Delta V_{mg} . \tag{12}$$

We note that ΔV_{it} in equation (12) corresponds to the net interface trap charge ΔQ_{it} at threshold (or inversion). ΔQ_{it} is the integral of the interface trap charge distribution between the midgap and threshold values of surface potential. ΔV_{it} is positive if the net charge in this region is negative.

There are several variations on a theme, all basically using the same assumption of midgap neutrality of interface traps. For example, one can use the stretchout of MOS capacitor C-V curves between the midgap and inversion voltage points, or the stretchout of subthreshold I_D-V_g curves of MOS transistors between midgap and threshold, or if the leakage currents are too high to measure the drain current at midgap (usually in the sub-picoampere regime) then the so-called subthreshold slope method is used, which essentially is the extrapolation of the drain current in the subthreshold regime down to its value at midgap. We do not present further details of the methods here but refer the interested reader to the literature for these [122–124] and other methods of charge separation [125,126]. As a final comment here we note that there is still some disagreement [127] about the validity of the midgap N_{it} charge neutrality assumption; however, it has given useful results in practice and the assumption seems to hold at least approximately for most devices.

3.4.5 Classification Scheme for Oxide Response

Assuming that the charge separation of ΔV_T can be made into the individual contributions from ΔN_{ot} and ΔN_{it}, then it is useful to separate the response of various oxides into various categories depending on the magnitudes and relative ratio of

the two charge components. A primary motivation for such a classification is to put some order into the rather complex picture of possible oxide response (e.g., see fig. 26) and to assist in establishing useful guidelines for appropriate radiation testing. If one knows (can measure) the separate amounts of ΔN_{ot} and ΔN_{it} for a particular device, then based on past accumulated experience, one has some handle on the qualitative features of the radiation response of the device and can generate pertinent test data to help in making quantitative predictions about the device response in a particular environment.

An example of a scheme proposed by Boesch [128] to categorize oxide response for such purposes is the matrix shown in table 3. It essentially classifies oxide response as being one of four qualitative types, based, first, on low ΔN°_{ot} or high ΔN°_{ot} and, secondly, on whether $\Delta N_{it} \ll \Delta N^{\circ}_{ot}$ or $\Delta N_{it} \approx \Delta N^{\circ}_{ot}$. Here, ΔN°_{ot} is the oxide trapped hole density present at the earliest measurement times of interest, before appreciable trapped hole annealing occurs. Note that categories for $\Delta N_{it} \gg \Delta N^{\circ}_{ot}$ are not included, since this case is not observed in practice. We do not discuss this classification scheme in detail or how it may be put to use in testing schemes. However, noted in the matrix table are the general qualitative features of the response in each case. We also note that in practice some oxides will fall into the grey zones between the categories, a problem inherent in any classification scheme. In these cases, one should always go to the more conservative category for choosing testing procedures.

Table 3. Categorization matrix of possible total-dose response types for MOS devices, indicating qualitative features of response for each type. ΔN°_{ot} refers to trapped hole density before annealing occurs [128].

	$\Delta N_{it} \ll \Delta N^{\circ}_{ot}$	$\Delta N_{it} \approx \Delta N^{\circ}_{ot}$
Low ΔN°_{ot}	**Category 1** No superrecovery Moderate log(t) recovery Negligible mobility degradation Hard	**Category 3** Some superrecovery Complex time history Some mobility degradation Hard
High ΔN°_{ot}	**Category 2** No superrecovery Weak log(t) recovery Possible mobility degradation Soft	**Category 4** Large superrecovery Complex time history Severe mobility degradation Soft

3.4.6 Dose Enhancement

As a final topic in this section on radiation testing, we discuss a current problem of great interest having to do with the use of low-energy x-ray testers for generating radiation effects data. This is a different type of problem from the ones we have been discussing, in that it does not involve issues relating to the time-dependent MOS response; rather, it involves ascertaining the actual ionizing dose delivered to the oxide.

The general phenomenon of dose enhancement has been known and studied for years. It occurs in the regions near interfaces between materials of different atomic number under photon (x-ray, gamma) irradiation. It is essentially due to a dose gradient arising from differences in the secondary electron production and transport properties of the two adjoining materials. Secondary electron equilibrium exists in the bulk of materials, but not for distances from an interface less than the maximum secondary electron range. The problem has come up recently in radiation testing of MOS devices because of the advent and growing popularity of laboratory bench-type low-energy ($\sim$10 keV) x-ray testers used instead of conventional ionizing radiation facilities, such as Co^{60} sources. The advantage of such low-energy x-ray testers is that they can be safely used, with some minor precautions, directly in a lab environment or on a production line.

Figure 30 illustrates the dose enhancement problem associated with thin SiO_2 film MOS structures [27]. Shown are schematics of the spatial profiles of the actual dose delivered (dashed lines) to an MOS device with (a) a thick ($\gg$500 nm) SiO_2 layer, and (b) a thin ($\lesssim$100 nm) SiO_2 layer that is typical of current technologies. For 10-keV x rays in SiO_2, the average secondary electron range is $\sim$500 nm, so this distance is the criterion for thin or thick oxide layers for purposes of dose enhancement effects. The solid straight curves in each figure represent the bulk equilibrium dose levels. Figure 30b indicates the dose enhancement effect

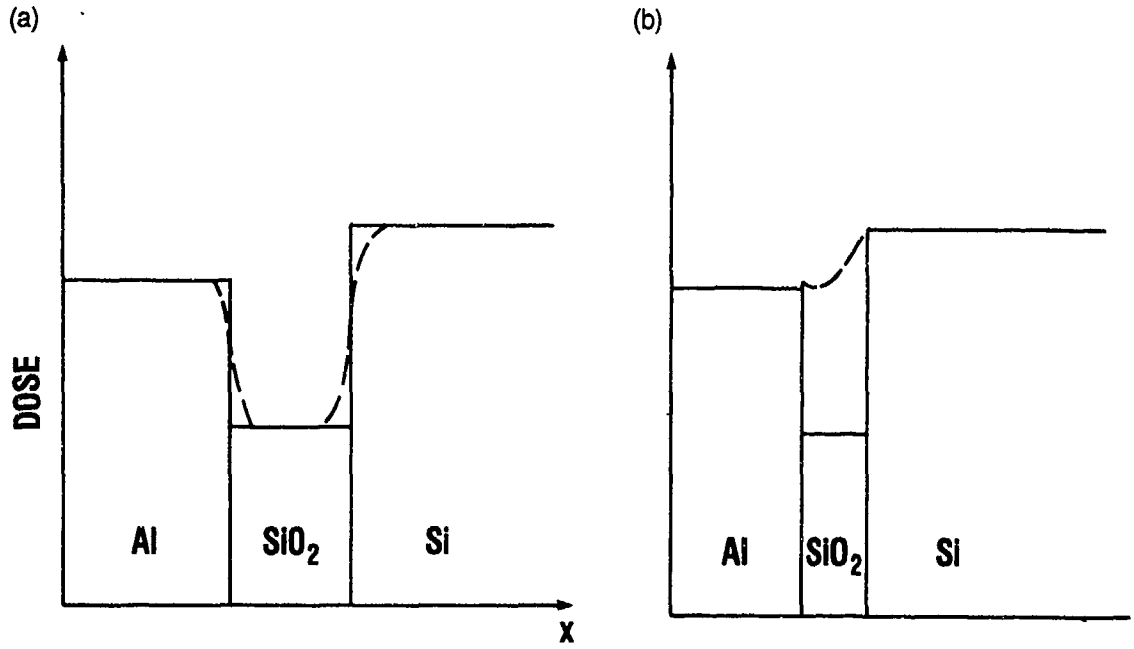

Figure 30. Schematic diagram illustrating dose enhancement effect in thin SiO_2 layers associated with low-energy (~10-keV) x rays: (a) thick SiO_2 layer (≳500 nm) and (b) thin SiO_2 layer (≲100 nm). Solid lines indicate bulk equilibrium dose values in each region and dashed lines actual dose profiles [27].

(dashed line) in thin SiO_2 layers over the bulk SiO_2 value due to the nonequilibrium secondary electron emission into the SiO_2 layer from the adjoining Al and Si regions.

Figure 31 is a composite figure taken from Benedetto and Boesch [129] indicating the results of recent work on this problem. It shows the relative dose enhancement factor (ratio of actual dose delivered to the bulk dose value) as a function of oxide thickness. The circles are two sets of experimental data points [27,129] and the two curves are theoretical calculations [64,130]. There seems to be reasonable agreement between theory and experiment. But the main point is that there is clearly a dose enhancement effect for the low-energy x rays, with an enhancement factor of ~1.6 for oxide thickness ≲100 nm. We note that for the high-energy (~1 MeV) Co^{60} gamma photons, the enhancement effect is essentially negligible, because for these energy photons the cross sections for interaction (Compton scattering) are very nearly the same for all the materials indicated on figure 30, and the secondary electron fluxes across the boundaries are very nearly the bulk equilibrium values. Therefore, it is important when comparing radiation response data taken with a low-energy

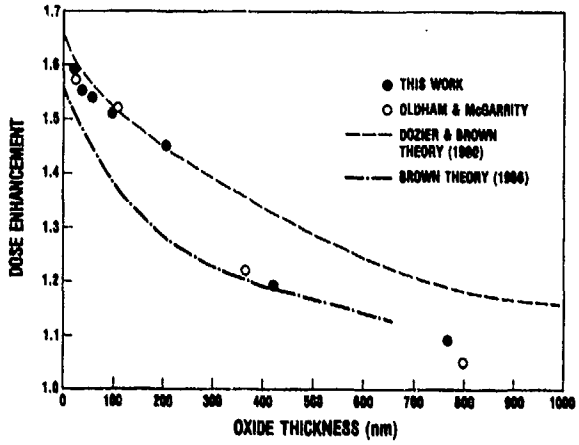

Figure 31. Measured and calculated dose enhancement factors versus SiO_2 oxide layer thickness for 10-keV x rays [129].

x-ray source with data from Co^{60} that the dose enhancement factor is accounted for in the low-energy x-ray data.

3.5 Implications of Scaling Down Oxide Thickness

In section 3.3 on the physical processes of the radiation response of MOS systems, we noted sev-

eral benefits that are gained when the gate oxide layer is thinned. First, the initial shifts are reduced according to equation (5) as d_{ox}^2, and the long-term hole trapping N_{ot} scales accordingly in the linear regime. Second, the short-term recovery time (hole transit time) decreases as $\sim d_{ox}^4$; see equation (6) and following discussions, or figure 17. Third, the recovery time is further decreased if also the gate potential is the same for a thinner oxide, resulting in a larger oxide field ($E_{ox} \sim V_g/d_{ox}$). (See eq (6) or fig. 15.) The combined effect of all three factors is dramatically illustrated by the flatband voltage recovery data shown in figure 32 for three as-grown oxide thicknesses (37.6, 56.6, and 96.3 nm) exposed at 220 K to pulsed LINAC irradiation under constant 10-V applied gate bias [38]. The vertical slash marks indicate the 75-percent recovery point in each case. (These data are not normalized, so that the d_{ox}^2 reduction in the initial ΔV_{fb} is also included.) We simply note that thinning the oxide by a factor of ~2.5 leads under these conditions to more than an order of magnitude reduction in the shifts for the entire time regime of the measurements.

Now turn attention to the effect on long-term deep hole trapping. First of all, ΔV_{ot} obviously scales in the same manner ($\sim d_{ox}^2$) as the initial shift. Next, if gate bias is constant, then the fraction of hole trapping decreases as $E_{ox}^{-1/2}$ for fields above 1 MV/cm, and further the long-term annealing rate

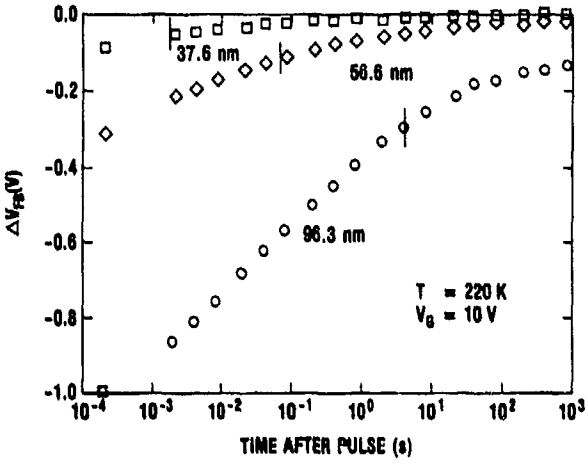

Figure 32. Flatband voltage recovery data at 220 K for three thicknesses of as-grown oxide MOS capacitors under constant 10-V applied gate bias. Vertical slash marks indicate 75-percent recovery point in each case [38].

is somewhat enhanced with increasing field (see sect. 3.3.3). But now consider what happens when d_{ox} is scaled down to and below the order of 10 nm. We discussed in section 3.3.3 that for temperatures below ~150 °C, the tunneling of electrons from the Si substrate into the SiO_2, where they recombine with the trapped holes, seems to be the process responsible for the long-term anneal of the oxide positive trapped charge. Referring to figure 22, the time-dependent tunneling distance $X_m(t)$ associated with the tunnel anneal process lies in the range from 2 to 4 nm for practical times of interest, say from 10^{-3} to 10^6 s. Hence, for oxides with $d_{ox} \lesssim 10$ nm, one could expect enhanced hole removal to occur by electrons tunneling into the oxide from the gate electrode also. In fact, the tunneling parameters would be roughly the same for polysilicon-gate material as for the Si substrate. This possibility of enhanced recovery by trapped hole recombination with tunneling electrons from both electrodes is indicated schematically in figure 33.

That this indeed seems to occur is indicated by the low-temperature (80 K) data shown in figure 34. Here, the circles are data (from Benedetto et al [79]) of threshold shift per unit dose on MOSFET's having oxide thicknesses between 5 and 11 nm, compared with a fit (solid line) to earlier flatband voltage shift data of Saks et al [78] on MOS capacitors with d_{ox} between 5 and 80 nm. The dashed straight line in the figure is the simple d_{ox}^2 scaling law from equation (5) with no annealing. We recall that at 80 K and for fields $\lesssim 2$ MV/cm, there is no

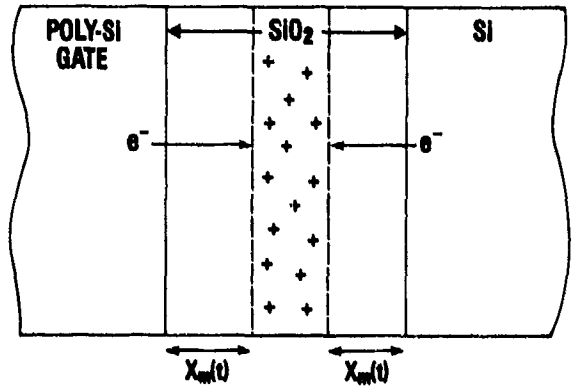

Figure 33. Model schematic of trapped hole removal in thin gate-oxide MOS structures by electron tunneling from both Si substrate and polysilicon gate [79].

appreciable hole transport in the time regime of figure 34; essentially all the annealing occurs via hole removal by tunneling. To be sure, there would still be a drop in the shifts below the d_{ox}^2 line for tunneling only from the Si interface, especially for thin oxides where the tunneling distance $X_m(t)$ cannot be neglected compared with d_{ox} in the charge moment expressions for voltage shifts. However, the magnitude of the departure of ΔV from the d_{ox}^2 scaling for $d_{ox} \lesssim 10$ nm is consistent only with tunneling from both electrodes.

The case is strengthened further by the time-dependent recovery data [79] for threshold shift and transconductance change Δg_m, shown in figure 35 for a MOSFET with a thin gate oxide of 5.3 nm, also irradiated at low temperature (77 K). Here, both ΔV_T and Δg_m show log time annealing from 10^{-3} to ~2 s, where essentially complete recovery of ΔV_T occurs and the response flattens out with the threshold voltage at its preirradiation value. This is simply explained by the tunneling fronts shown in figure 33 converging near the center of the oxide with essentially complete removal of the radiation-generated holes. The recovery and flattening of Δg_m at the same time suggest that the trapped holes in the oxide serve as additional scattering (Coulomb) centers for the channel carriers, with the additional scattering vanishing upon removal of the holes. (The increase in the response curves at $t \gtrsim 100$ s is probably due to thermal instability (instrumental drift) problems at long times; note the millivolt voltage scale in fig. 35.)

The bottom line from this discussion is quite clear: there are very significant gains to be made in the radiation performance of MOS devices by thinning the gate oxide layers. Very dramatic gains can be made by thinning d_{ox} down to and below 10 nm (fig. 34 and 35). This range is probably not achievable for practical production in the near future, but quite substantial gains are achieved even in reducing d_{ox} down to the 10- to 30-nm range (see fig. 32), which is certainly the range present-day very-large-scale integrated circuit (VLSI) technologies are beginning to employ. As the gate oxide thicknesses are scaled down to this regime, there will be decreased concern about the radiation susceptibility of the gate oxides. As a consequence, it is likely that we will see the emphasis in total-dose hardening efforts shifting more toward field and passivation oxides, and hence from radiation-induced threshold voltage shifts to radiation-induced leakage currents, a topic we now address only briefly.

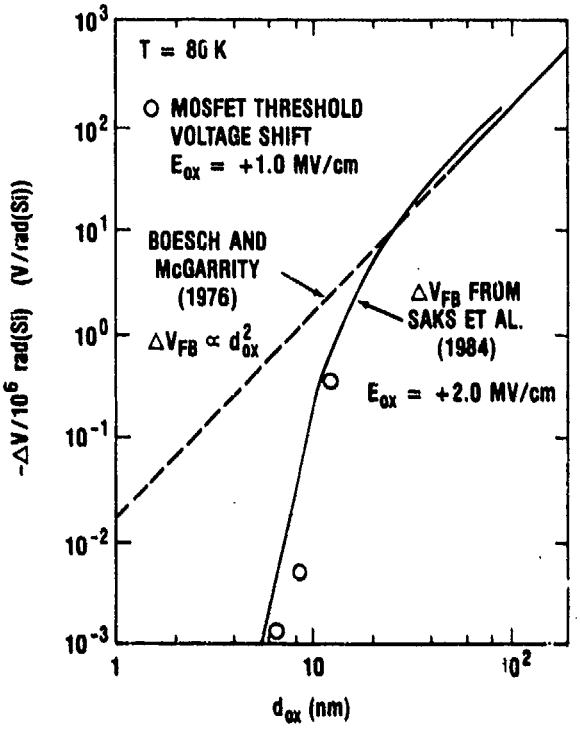

Figure 34. Threshold and flatband voltage shifts per Mrad(SiO_2) at 80 K. Dashed line is simple oxide thickness squared scaling; solid line is ΔV_{fb} data on capacitors [78]; and circles are ΔV_T data on MOSFET's [79].

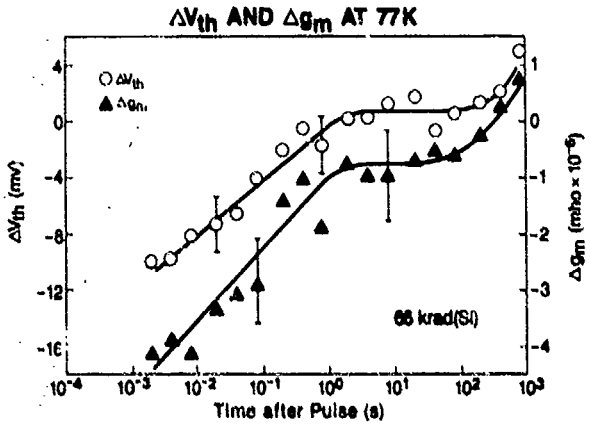

Figure 35 Recovery of threshold voltage shift and transconductance change following pulsed electron beam irradiation at 77 K for MOSFET with 5.3-nm gate oxide [79].

3.6 Total-Dose Radiation-Induced Leakage Currents

In our discussion of the physical mechanisms underlying the radiation response of MOS devices, we focused attention on the gate oxide layer and on the consequences of trapped charge buildup in these layers, primarily that of induced shifts in threshold voltages. However, exactly the same physical processes leading to charge buildup—charge generation, transport and trapping, and interface trap generation—also occur in the thicker oxides used as field regions or isolation or passivation oxides in IC technologies. But instead of voltage shifts, the effects of charge buildup in these oxides on circuit operation involves generation of undesirable parasitic current leakage paths. Specifically, charge buildup in field/passivation/isolation oxide regions can induce formation of inversion channels in the surface regions of adjoining semiconductor regions which, in the presence of any potential gradients (i.e., fringing fields), will result in parasitic current leakage paths. These induced current leakage paths can be important failure modes not only in bulk MOS technologies, but in silicon on sapphire (SOS) and silicon on insulator (SOI) structures and even in bipolar technologies as well.

Figure 36 is a schematic showing a possible induced leakage path in an MOS device structure. Shown are top (a) and cross section (b) views of the device with the various regions of the device indicated. In particular, the field oxide region covers the Si substrate outside the gate oxide and normal source-drain channel regions. If sufficient radiation-induced charge buildup occurs in the field oxide region, especially near the Si substrate, then an inversion layer can be formed in the substrate as indicated in figure 36b, even with the normal channel turned off. This induced channel region under the field oxide then offers a low-resistivity current leakage path between the source and drain around the edge of the gate oxide (normal channel) region as shown in figure 36a. We note that the charge buildup in the field oxide near the substrate interface proceeds in exactly the same manner as in the gate oxide, namely, in response to positive voltages applied to the gate contact lines (or other metal strip lines) over the field oxide, which drive the radiation-generated holes down toward the field oxide/Si interface (fig. 36b). Because the field oxide layers are much thicker than the gate oxide layers, the magnitudes of the fields are much lower (more like 10^5 V/cm rather than 10^6 V/cm) in the field oxide regions; however, the basic processes leading to the buildup are just the same. Furthermore, the charge generation volumes are considerably larger.

The schematic diagrams shown in figure 36 do not accurately reflect today's MOS structures, but the basic principle of the induced leakage current is the same nevertheless. Figure 37 shows a cross section of a more modern recessed field oxide MOS structure. The leakage paths between source and drain in these structures are thought to be in the Si substrate under the so-called bird's beak region of the recessed field oxide, which is immediately adjacent to the gate oxide channel region.

Typically one studies the induced leakage currents under field oxides with the aid of special test field oxide transistors, in which the field oxide

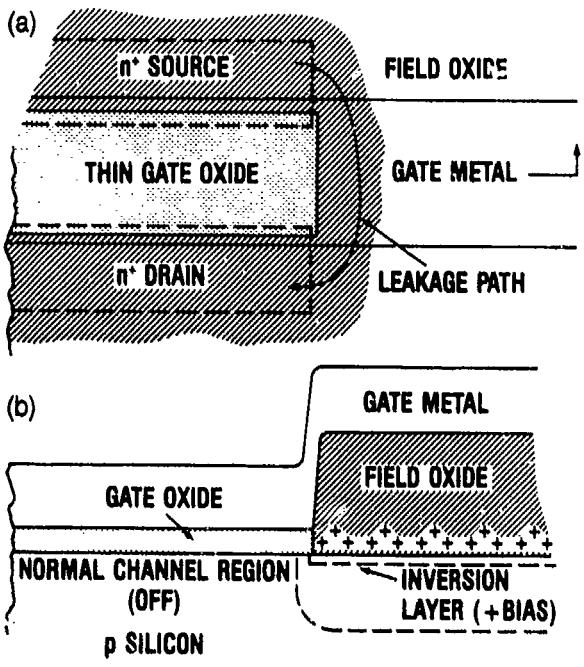

Figure 36. Schematic of MOS device structure indicating in (a) radiation-induced current leakage path due to positive charge buildup at (b) field-oxide/substrate interface.

material is used as a gate oxide in a normal MOS transistor configuration. Some postirradiation subthreshold leakage current measurements [75] are shown in figure 38 for a device with a channel length of 1.0 μm. Results are shown after each of a series of 10-krad(SiO_2) LINAC pulses. Increases in leakage currents by at least several orders of magnitude are obtained. We note that as channel length is reduced, the fringing fields in the field region between source and drain in an actual device configuration increase, which results in increased leakage currents.

Up until rather recently, total-dose ionization effects were generally thought to be negligible in bipolar circuits because of the absence of gate oxides in bipolar devices. However, as device dimensions shrink, it is becoming apparent that bipolar technologies suffer from similar total-dose-induced leakage currents associated with charging of the SiO_2 field and passivation oxides used in bipolar microcircuits. Figure 39 shows a representative modern bipolar device structure taken from Pease et al [131]. Indicated on the figure are three possible regions where leakage paths may be induced because of charge buildup in the recessed field oxide.

Finally, we mention that SOS and SOI technologies suffer from so-called radiation-induced back channel leakage. Figure 40 shows a simple schematic of an SOS structure (it could as well be an SOI structure), indicating radiation-induced positive charge buildup in the sapphire substrate immediately under the active p-Si layer. The normal device channel occurs in the p-Si region next to the gate oxide region. However, because of the positive charging of the sapphire substrate, an inversion layer can be induced on the back side of the p-Si region, resulting in the back channel leakage between source and drain.

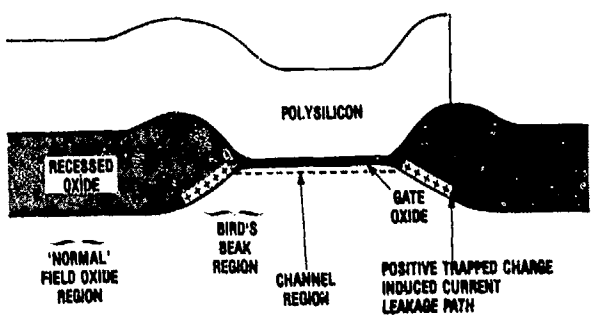

Figure 37. A modern recessed field-oxide structure indicating charge buildup and induced current leakage paths in bird's beak regions of device.

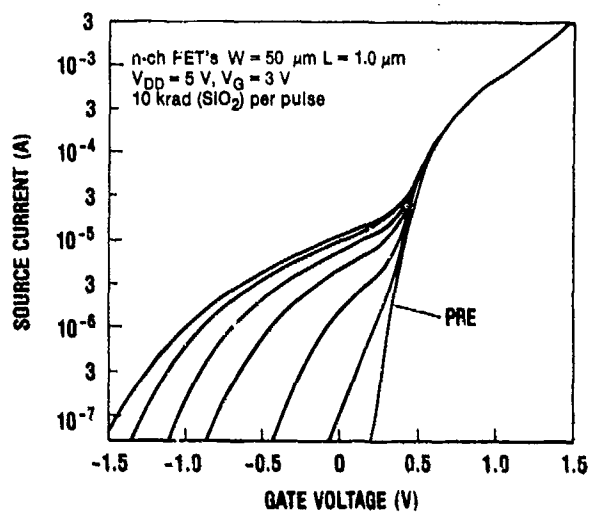

Figure 38. Radiation-induced increase in subthreshold leakage currents in field-oxide transistor test structure [75].

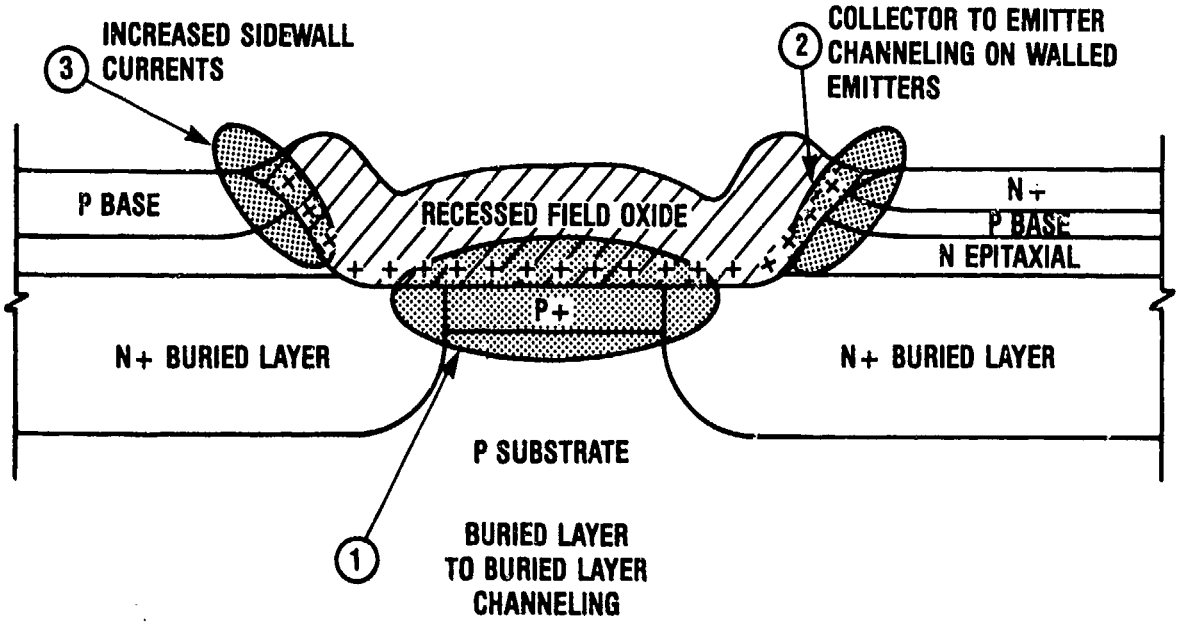

Figure 39. Regions of possible radiation-induced charge buildup and leakage currents in bipolar device structure [131].

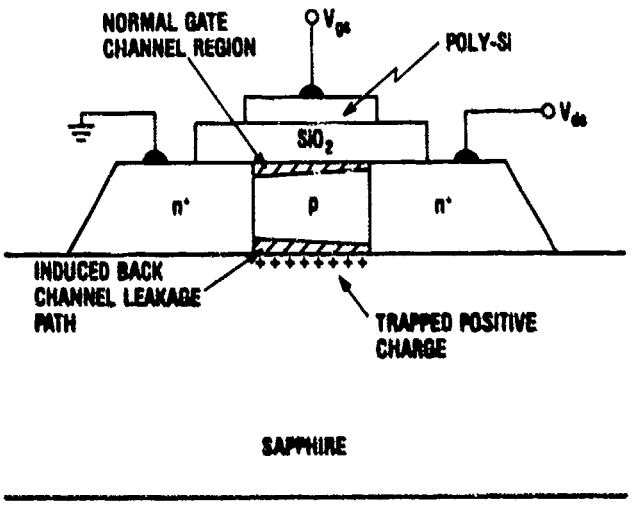

Figure 40. Schematic diagram illustrating back-channel current leakage in silicon-on-sapphire MOS transistor.

4. Transient Radiation Effects

4.1 General Remarks

The term *transient radiation effects* is commonly used to describe those effects caused by radiation-induced photocurrents. These can result either from high dose rate, bulk semiconductor ionization generated by high-intensity pulsed irradiation (the $\dot{\gamma}$ problem), or the dense ionization generated by a single energetic heavy ion (the SEU problem).

The major effects in IC's arising from the short but large-amplitude transient photocurrents include the following:

(1) Simple transient upset in which there is a temporary bit flip, either logic or memory, because of the high current level or excess charge collected at a sensitive bit node in a circuit. The effect is transient in that only the information stored in the bit at the moment of the upset is lost; there is no permanent or long-term damage to the bit cell. The cell becomes functional again upon reset by the next logic cycle or memory write operation.

(2) Long-term induced parasitic transistor states of low voltage and high current. These states include current latchup (which is an npnp silicon-controlled-rectifier type of parasitic state) and the so-called snap-back effect, which is a result of photocurrent-induced initiation of avalanching in the drain junction of an n-channel MOS transistor. These effects can persist indefinitely unless the circuit is properly reset. If the induced parasitic current levels are sufficiently high, they can cause permanent device failures such as junction burnout. These parasitic current states are geometry specific, that is, highly dependent upon the specific device and circuit layout, and will not be discussed here.

(3) Permanent or so-called "hard" failures, which include the abovementioned problem of junction burnout due to heating from very high and prolonged current levels, and dielectric breakdown of thin insulating films due to transient electrical overstress arising from photocurrent effects. Also, in very small scale devices, permanent failures can in principle arise from single-event-induced charge buildup in oxide films or from a single-event-induced displacement damage cluster across an active semiconductor region. These latter SEU effects have not yet been observed, but they are thought to be possibilities if device dimensions are scaled down sufficiently.

The physics of radiation-generated photocurrents is basically understood. In actual practice, however, circuit upset levels are highly dependent upon the specific and usually complex IC device/circuit geometry and upon the specific operational electrical configuration of the circuit. For these reasons, realistic prediction calculations of circuit upset require sophisticated computer simulations. In simplistic terms, the criteria for upset are basically of two types, depending on whether the circuit nodes are charge sensitive or current sensitive: (1) the charge collected at the node within a given time interval exceeds a critical charge for upset, or (2) the actual current level during the photocurrent pulse exceeds a critical current value.

In this discussion of basic mechanisms we illustrate the physics of photocurrent generation with just two simple examples: namely, the radiation-induced photocurrents generated (1) by uniform ionization of an ideal, reverse-biased p-n junction diode, and (2) by the passage of a single highly ionizing particle through the depletion well of an ideal reverse-biased Schottky barrier diode. In the latter case we are concerned with the additional effects caused by screening of the depletion region electric fields by the dense ionization cloud surrounding the track of the particle. This screening effectively extends the field region down into the previously field-free, quasineutral substrate, and results in the so-called field funneling effect.

4.2 Ideal p-n Junction Photocurrents

In figure 41, we show an ideal p-n junction diode being exposed to ionizing radiation [6]. The combined n and p depletion width is W, and the diffusion lengths L_n and L_p are given by $(D_{n,p}\tau_{n,p})^{1/2}$, where D is the diffusion coefficient and τ is the carrier lifetime, and n and p refer to electrons and holes, respectively. The primary photocurrent consists of two components, a prompt (mostly drift) component, i_p, and a slower diffusion current, i_d. The charge pairs produced by the radiation in the depletion region will be separated by the applied field and collected as prompt drift current. If we postulate a step function radiation source with a generation rate of G (pairs/cm^3-s) for $t \geq 0$, then $i_p = qAGW$ at early times, where A is the area of the junction, AW is the depletion region volume, and q is the electronic charge. This result is valid as long as diffusion currents are negligible—that is, for $t \ll \tau_n, \tau_p$. At late times ($t \gg \tau_n, \tau_p$), the photocurrent will reach a saturation value $i_{pp} = i_p + i_d = qAG(W + L_n + L_p)$. This expression is similar to the early time result, except that the collection volume includes the depletion region plus a diffusion length on either side. In figure 42, we illustrate the photocurrent as a function of time [5], for which we have described the asymptotic limits. The theory describing the transition from drift-only current to drift-plus-diffusion current is well developed [132], but we do not describe it here. Similarly in figure 43, the solid line shows the response of a p-n junction to a step function, this time plotted on a linear scale [133]. The dashed curves illustrate the photocurrent response if the radiation is cut off at some time—a pulse rather than a step function. Again,

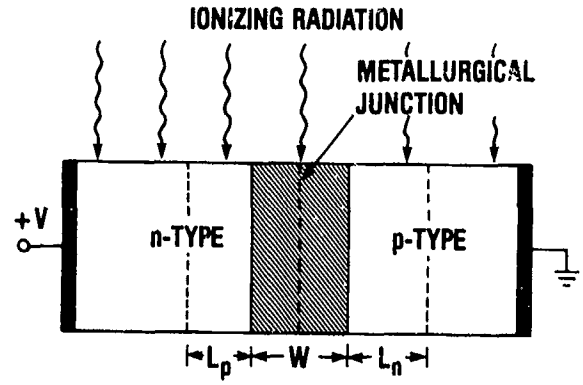

Figure 41. Schematic diagram of a p-n junction diode being bombarded with ionizing radiation.

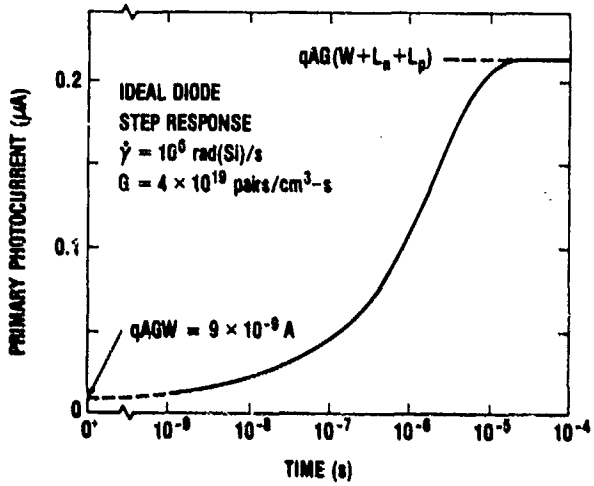

Figure 42. Calculated photocurrent due to step function generation rate for an ideal diode [5].

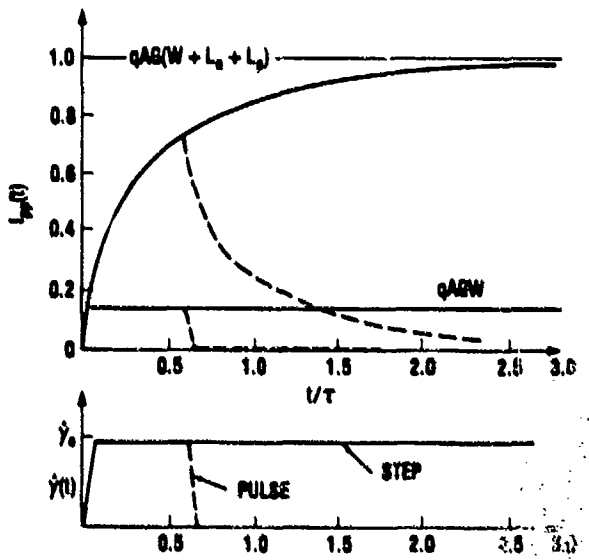

Figure 43. Ideal diode transient photocurrent response [133].

good analytical treatments of this response are available [132], but we do not discuss them here.

4.3 Single-Particle-Induced Photocurrents—Field Funneling Effect

In recent years, single-event upset has been an extremely important reliability problem for the radiation effects community and for the electronics community in general. The work that convinced the world that SEU was a real effect was reported by May and Woods [134], who studied the effect in dynamic random access memories (RAM's). The mechanism which they reported is illustrated in figure 44. A radioactive contaminant in the packaging emits an alpha particle which passes through the p-well of a storage capacitor. Depending on the bias applied, the well will be inverted (full of electrons) or depleted (empty of electrons). The negative charges tend to move toward the positive gate and the positive charges move away from the gate. If the well is already full of electrons, it simply remains full of electrons, and no change of state (bit flip) is observed. But if the well is initially empty, as for the case depicted in figure 44, it will become partially filled with electrons. If enough electrons are collected in the well, it will be sensed as "full," and a bit flip occurs.

An important concept here is the critical charge, the number of stored electrons representing the difference between a stored "0" and a stored "1" (see, for example, work by Ziegler and Lanford [135]). For dynamic RAM's operating at 5 V, the largest voltage swing which can be tolerated without losing stored information is about 2.5 V. If the storage capacitance is 50 fF, then $Q_{crit} = C_{st}\Delta V_{crit} = 50 \times 10^{-15}$ F $\times$ 2.5 V = 125 fC, or about 7.8×10^5 electrons. One of the main concerns behind the study of single-particle effects has been that reducing feature sizes means smaller area capacitors which tend to have smaller capacitance values. Because of scaling, more advanced memories have tended to have smaller critical charges. Of course the charge deposited by an alpha particle does not scale, so upset sensitivity would increase in more advanced circuits unless preventive actions are taken. We note that the total number of electron/hole pairs generated in Si by a 5-MeV α-particle is 1.5×10^6.

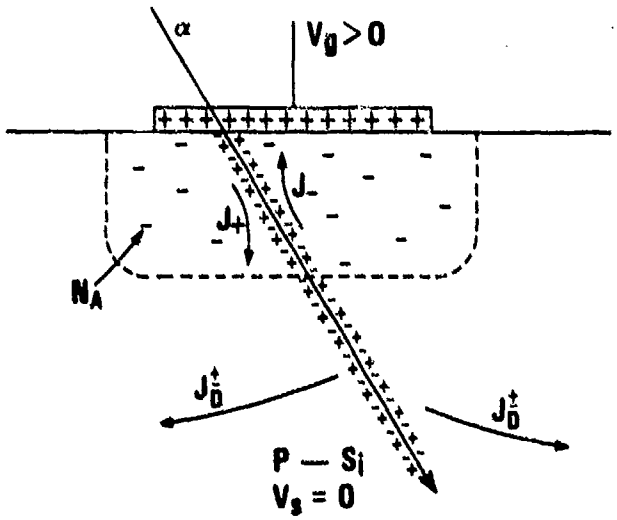

Figure 44. Schematic representation of an alpha particle passing through depletion well of a Schottky barrier diode [137].

An effect which made SEU seem potentially more serious than first thought was the so-called field funneling effect, first reported by Hsieh et al [136]. Funneling is illustrated in figure 45 [137], where we show an alpha particle passing through a junction depletion region at t = 0 (fig. 45a). In the charge column produced by the particle, the density is many orders of magnitude greater than the background doping level, so the depletion layer is immediately neutralized near the track (fig. 45b). After the depletion layer is neutralized, we have a dense column of charge—in effect, a plasma wire in contact with an electrode—which tends to screen electric fields from the interior of the column. As a consequence the field region is extended down the track, as indicated by the equipotential contours in figure 45c. The original idea in model-

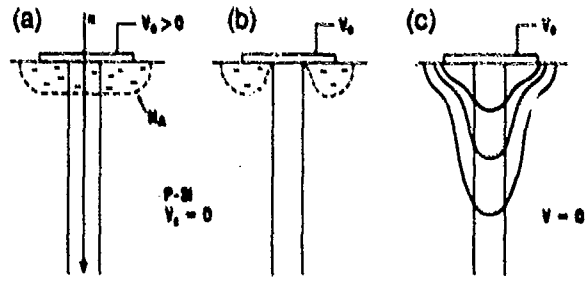

Figure 45. Schematic of charge funneling mechanism indicating (a) an alpha-particle strike through reverse-biased n⁺-p junction; (b) depletion layer being neutralized by plasma column; and (c) equipotential lines extended down along particle track [137].

ling charge collection was that the charge deposited in the depletion layer of the struck device would be collected rapidly by drift, and the remaining charge would be collected more slowly by diffusion [138]. The distortion of the field down the track meant that much more charge would be collected rapidly by drift than had been assumed.

The implications of this conclusion are illustrated in figure 46 [137]. For an alpha particle striking a node in a circuit array, the solid curve indicates the charge collection expected if diffusion is the main process. With funneling, considerably more charge would be collected at the struck node, with less collected at other nearby nodes (dashed curve). If the critical charge for this circuit is in the range indicated, one would expect an upset with funneling, but not without it.

In figure 47, we present experimental results [137] illustrating how much fast drift charge can actually be collected. The charge generated in the original depletion layer is the amount that would be collected rapidly by drift in the absence of funneling. The actual prompt charge collected (in about 1 ns) is indicated by the triangles, and is several times greater than the charge generated in the original depletion layer. The total charge collected, including the slow diffusion component, is also shown. These measurements were for 5-MeV alpha particles incident on p-type Si with a doping density of $8 \times 10^{14}/cm^3$, but similar results have been reported for n- and p-type Si over a range of resistivities and for different incident particles with a wide range of LET's [137,139].

The original reports of field funneling were based on large scale computer simulations along with confirming experiments. In figure 48, we show representative results of these computer simulations for alpha particles incident on p-type Si [136]. These results show the time scale on which the drift collection occurs (10^{-10} to 10^{-9} s), and they show how two samples of different resistivity compare. For more highly doped material, the charge is collected faster, but the total amount collected is less. However, these computer simulations (necessarily two- or three-dimensional) were expensive and difficult for others to use, so a number of simple analytical models were proposed [137, 139–141]. The purpose of these models was to allow reasonably accurate predictions to be made conveniently and quickly. The most widely used of these analytical models seems to be the so-called effective funnel length model [137,139]. The basic approach in this model is to define a collection depth $L_c = \bar{v}_d \tau_c + x_d$, where $\bar{v}_d$ is the average drift

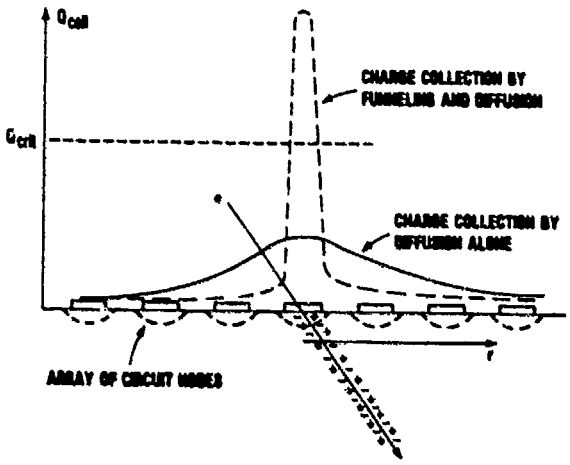

Figure 46. Schematic of charge collection profiles over a circuit array, illustrating enhancement of charge collection at struck node due to charge funneling [137].

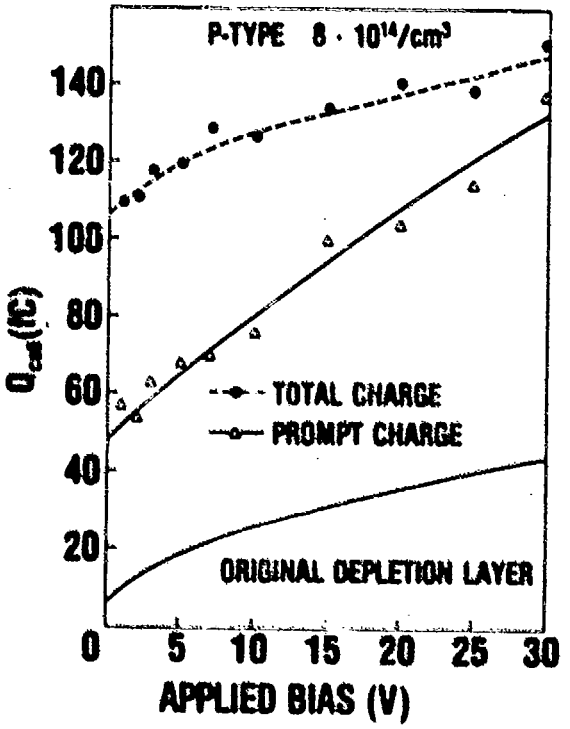

Figure 47. Measured prompt charge collection versus applied bias compared to charge generated in original depletion layer. Dashed line is total charge collected (prompt plus diffusion) [137].

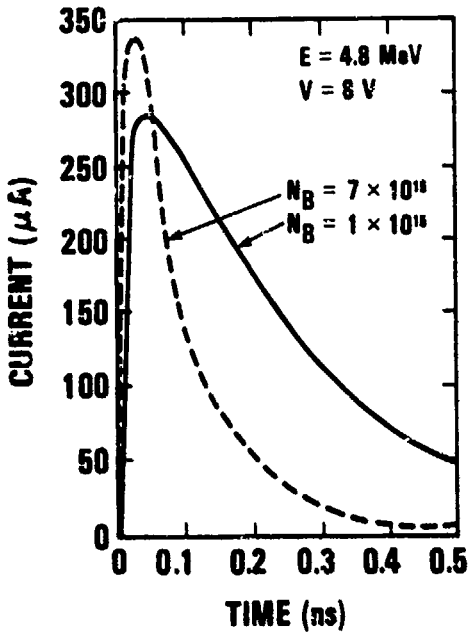

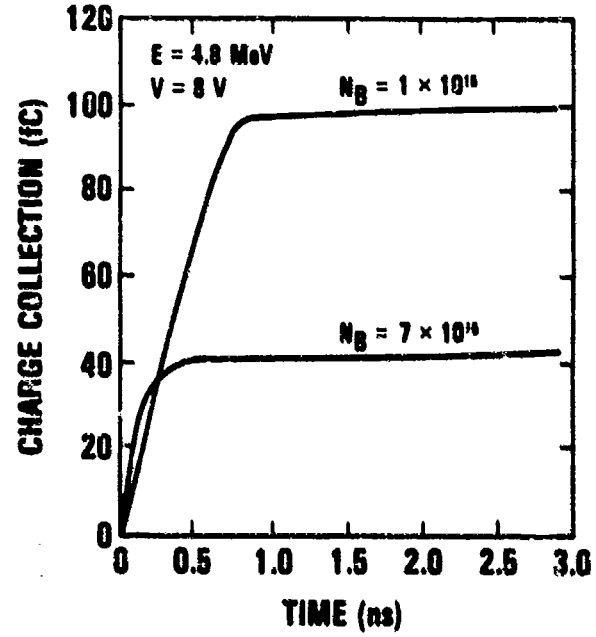

Figure 48. Computer simulations of transient current and charge collection for two substrate doping densities [136].

velocity of the carriers during the collection time τ_c, and x_d is the original depletion layer width. This expression for L_e is simply a formal statement that the drift charge collection will be equal to that generated in the original depletion layer plus that which can be drifted up to the depletion layer in a time τ_c. The collection time, τ_c, is determined by the initial density of charge along the track and by the background doping level of the substrate. Initially the plasma density is much greater than the doping level, but the plasma density drops rapidly as the column expands by diffusion and as the radial fields separate the charges. When the plasma density approaches the doping density at time $t \cong \tau_c$, the depletion region is assumed to reform, cutting off the funnel effect. The average drift velocity $\bar{v}_d$ is related to an average longitudinal field $\bar{E}_L$ which is assumed to exist along the track during τ_c. That is, $\bar{v}_d = \mu(\bar{E}_L)\bar{E}_L$ where μ is the field-dependent mobility of the carriers. Then one closes the loop by assuming that $\bar{E}_L = V_e/L_e$, where V_e is the total applied bias, including the built-in work function. This model in effect replaces a field distribution which varies rapidly in both time and space with a single constant effective average field. For this reason, the effective funnel length model is an extreme simplification, and it can really only be justified empirically.

In fact, this model has proven to be empirically useful in many cases. In figures 49 and 50, we show experimental results along with results of the effective funnel length model for alpha particles incident on p- and n-type Si over a range of doping densities [137]. The agreement is generally good between theory and experiment, especially at low biases, which are the most important in IC operation. When the effective funnel length model was first introduced, it made predictions about the dependence of prompt charge collection on several parameters: doping level, substrate polarity, applied bias, and stopping power of the incident ion. That is, charge collection decreases with increasing doping density, going as N_A^{-Z}, where $1/3 \leq Z \leq 1/2$. Prompt collection is greater in p-type Si than in n-type because the minority carrier mobility is greater. Prompt charge collection varies roughly with the square root of the applied bias. And prompt charge collection should vary with $(dE/dx)^y$, where $1 < y < 4/3$.

All these predictions were subsequently confirmed experimentally, except that for short-range incident particles, the prompt charge collection did not increase as fast as predicted with increasing dE/dx. The model equations were based on the assumption that the track could be represented by an infinitely long cylinder of charge. If end-of-track effects are important, the original model does not

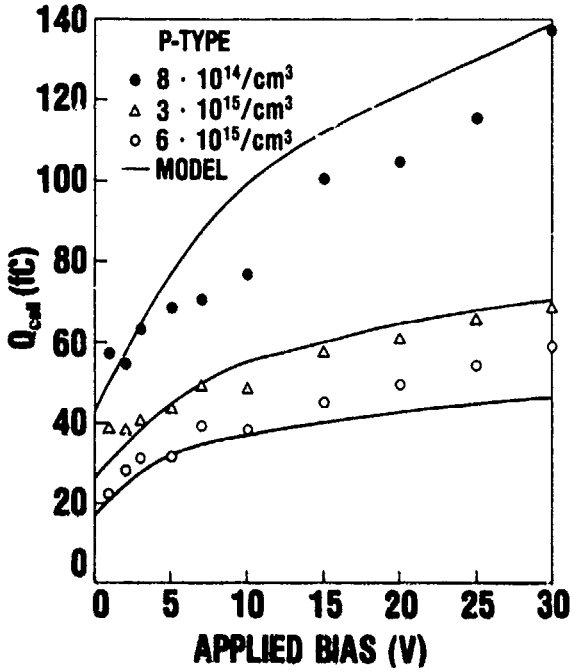

Figure 49. Drift charge collection measurements compared with effective funnel length model results for three p-type samples [137].

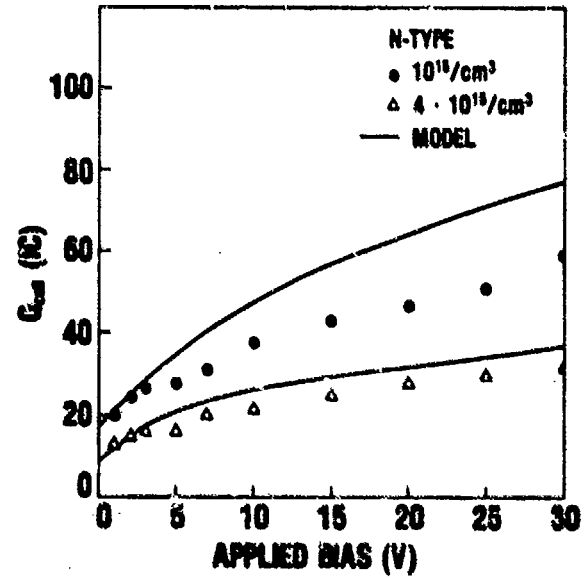

Figure 50. Drift charge collection measurements compared with model results for two n-type samples [137].

account for them. Two revised versions of the model have since been proposed to correct this limitation [142–143], but we do not discuss them here.

The charge collection problem is extremely complicated in general, and there is a limit to the usefulness of simple analytical treatments. To treat complex IC geometries will require computer simulations in the long run despite their drawbacks—cost and difficulty in implementation. We have already mentioned the difficulty caused by end-of-track effects in the effective funnel-length model, even in bulk Si samples. Real technologies increasingly use epitaxial Si, where the funnel would be cut off in the substrate, or they use dielectric substrates (SOS or SIMOX—separation by implanted oxygen). In addition, in a complex circuit, nearby elements would perturb field distributions. Something like the effective funnel-length model has no hope of dealing with all these complexities.

Finally, we want to point out that three kinds of single-particle-induced permanent failures have been discussed in the literature. With these mechanisms, the circuit itself is damaged—a more serious problem than simply losing data. One of these, single-particle-induced latchup, has actually been observed [144,145]. The second, total-dose failure of a small device from the ionization generated by a single heavy particle, has been studied in some detail [22,27]. In SiO_2, the columnar recombination process is so strong for heavy ion tracks that most of the charge generated by an ion simply recombines (see fig. 12 in sect. 3.3.1), and little damage is done to the device. This kind of failure may yet be observed, but the device would have to be very small. The third permanent failure mechanism, displacement damage from a single neutron or ion damaging an active device region, has also been studied in some detail [146–148]. So far, electrical changes attributable to single particles have been observed, but they have not been large enough to cause circuit failures.

5. Displacement Damage Effects

5.1 Introduction and General Comments

In this section, we discuss displacement damage effects in semiconductors. We consider the following questions:

1. How does displacement damage occur?

2. What kinds of particles cause displacement damage?

3. What kinds of defects occur as a result of displacement damage, and how are they distributed?

4. What are the electrical properties of different defect centers?

5. How much annealing of displacement damage occurs, and how fast?

6. What are the stable damage coefficients, and how do they depend on other experimental variables?

7. What are the effects of displacement damage in device physics?

In answering these questions, we describe in a general way the basic physical processes, and we present typical results to illustrate the main effects and how some of the different parameters interact. However, a great deal of work has been done on some of these questions, and we cannot cover more than a small part of it.

First, how does displacement damage occur? The basic physical interaction was illustrated in figure 5a, where an incident particle is shown striking a target atom. This primary interaction results in a target atom recoiling from its lattice site, as well as a scattered particle. If the recoil is energetic enough, the atom is knocked loose from its lattice site and comes to rest some distance away at an interstitial site (fig. 5b). Figure 5 shows a scattering event producing a single vacancy/interstitial pair, but usually the recoiling atom and the scattered primary particle will undergo other interactions. In this case, a cascade of displaced secondary atoms will result.

The simplest mathematical description of the scattering event illustrated in figure 5a is that of an elastic two-body collision. The equations for such a collision follow from the fact that both energy and momentum are conserved. (These equations are treated in detail in a number of basic textbooks in both laboratory coordinates and center-of-mass coordinates [1–3,149,150]. For this reason, we do not discuss these equations in any detail.) Several assumptions are implicit in using an elastic two-body collision model. We assume the particles act like hard spheres with no energy dissipated in electronic excitations or in nuclear reactions. In addition, we assume that no energy is lost to the lattice (that is, to other nearby atoms) when the recoil atom escapes. Frequently these assumptions are well justified, because the energy lost in breaking bonds in the lattice is very small compared to the energy of the particles involved. For example, only about 25 eV need be transferred to a recoil atom in

Si in order to produce a vacancy/interstitial pair. The energy of typical incident particles is measured in MeV, on the other hand. In fact, many other materials also have critical energies for displacement around 25 eV. If only a few electron volts out of 1 MeV are lost to electronic excitations and lattice distortions, these effects can generally be neglected. (Nuclear reactions, if they occur, may be more important.)

This discussion leads into our second question: what kinds of particles can cause displacement? In principle, any energetic particle can cause displacement damage; neutrons and energetic charged particles (electrons, protons, alpha particles, heavy cosmic ray ions) are the most important ones. Since neutrons do not interact directly with the electrons in the target material, they lose energy only through nuclear interactions. For this reason, displacement processes are much more important for neutrons than for charged particles. For the charged particles, interactions with atomic electrons cause most of the energy loss, but Coulomb scattering from nuclei can lead to displacement damage also. The qualitative differences between the interactions of charged and uncharged particles are illustrated in figure 51, where

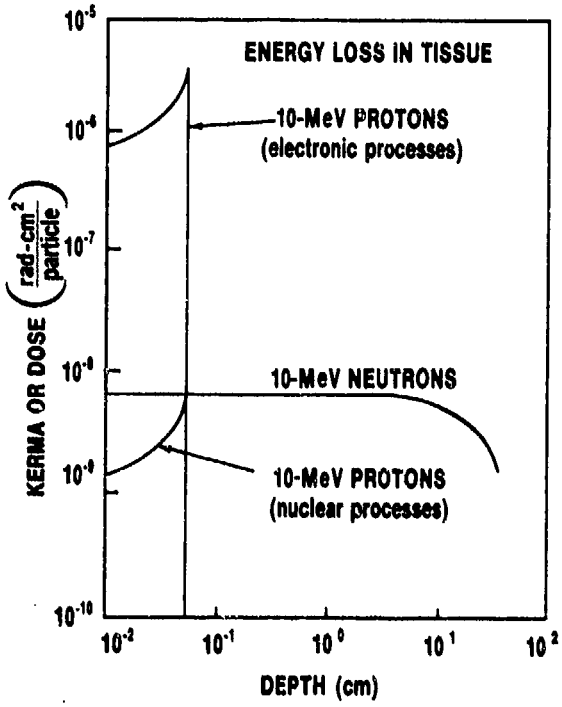

Figure 51. Energy loss for 10-MeV neutrons and for 10-MeV protons indicating for protons energy loss due to both electronic and nuclear processes separately.

we compare the energy deposited in tissue through different processes for 10-MeV protons and neutrons. (The results for silicon are qualitatively similar.) For the 10-MeV neutrons [151], the primary interaction is a nuclear scattering event, but the knock-on atom or atoms lose a large part of their energy through ionization. The total energy loss for neutrons is plotted in the figure, but only a small part of this energy loss actually goes into displacement processes. The remainder is lost by ionization in the slowing down of the knock-on atoms (see fig. 52). For the proton curves in figure 51, we plot the nuclear energy loss and the electronic (ionization) energy loss separately. The electronic processes account for roughly three orders of magnitude more energy loss than nuclear processes.

This is illustrated by figure 52, where we plot for protons the energy loss from nuclear processes (the Lindhard, Scharff, and Schiott—LSS—theory) [152] as a fraction of total energy loss (nuclear plus electronic). For neutrons, we plot the nuclear (LSS) fraction of total energy loss for a primary silicon knock-on atom. For example, an Si atom with an initial energy of 1 MeV would lose about 20 percent of its energy through nuclear processes. If these results were replotted in terms of the energy of the incident neutrons, the curve would obviously be shifted to the right. For this reason, the neutron curve in figure 52 is a limiting case rather than an "exact" result.

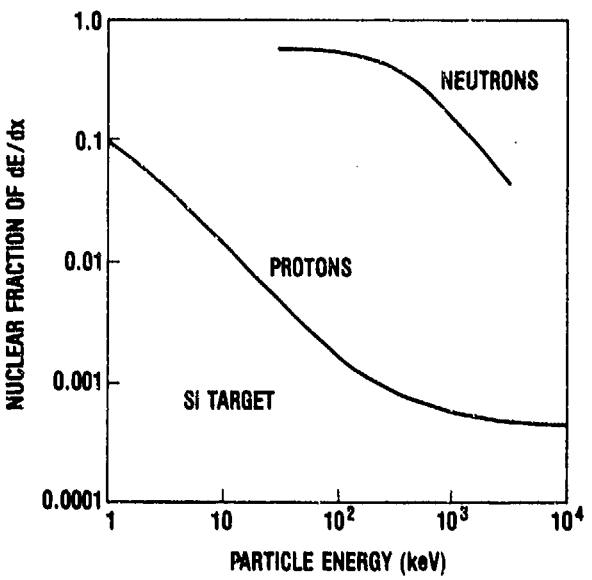

Figure 52. Nuclear fraction of energy loss for protons and neutrons.

The main point of this discussion is that the ultimate fraction of energy going into atomic displacements is one to two orders of magnitude greater for neutrons than protons. For this reason, displacement damage is generally the primary cause of degradation of electrical properties from high-energy neutron irradiation. Another associated key point is that the proton range is many orders of magnitude less than the neutron range (see fig. 51). By the time ionization effects by secondary particles are accounted for, protons may produce more displacement damage in a small increment of volume than neutrons at these energies. However, if one integrates over the range of the particles, the neutrons will cause much more displacement damage because of the difference in ranges.

We have tried here to point out the main qualitative differences between the interactions of charged particles and neutrons and the displacement damage they produce. However, the comparison of displacement effects produced by different kinds of particles at different energies and test conditions is a very active research area. In general, heavier particles generally produce more displacement damage than lighter ones, because they have more momentum at a given energy; however, a detailed picture has not yet emerged of the energy dependence of displacement damage by charged particles.

At this point we explain the concept of kerma, kinetic energy released in the material. Kerma is the initial kinetic energy of all the secondary particles produced by indirectly ionizing primary particles (photons and neutrons). Normally the kerma is the same as the dose. The only exception occurs for secondary particles sufficiently penetrating that they can escape the target material instead of being absorbed.

Next we consider our third question: what kinds of defects occur and how are they distributed? Defects may be classified as simple defects (vacancies, divacancies, vacancy/impurity complexes, interstitials, di-interstitials, interstitial/impurity complexes), as well as larger defect clusters. Historically, the first efforts at modeling displacement damage were attempts to explain experimental results in terms of isolated point defects. However, these results were not entirely satisfactory, leading Gossick [153] to postulate the existence of large disordered regions. This so-called Gossick model of defect clusters is illustrated in figure 53. The core of the damage region with radius R_0 is assumed to be compensated intrinsic material—that is, electrically neutral. The outer shell of the damaged region, between R_0 and R_1, is assumed to be charged by trapped majority carriers (electrons in our example). The space charge region between R_1 and R_2 is an undamaged depletion layer (positive in this example), which balances the trapped majority carrier charge. In the Gossick model, the disordered region presents a potential barrier to majority carriers and a potential well to minority carriers, with the result that defect clusters serve as very efficient regions for minority carrier recombination [5].

A "typical" distribution of clusters produced by a 50-keV Si recoil atom is shown in figure 54 [154]. No one has argued that the clusters are truly spherical, although a spherical shape is frequently assumed for convenience in modeling. The size of the clusters and their spatial distribution has been a somewhat controversial topic over the years. Gossick himself said that a damaged region would typically contain 10^5 to 10^6 atoms, corresponding to R_1 = 15 to 20 nm. (The clusters shown in fig. 54 are slightly smaller than proposed by Gossick.) On one hand, Srour et al [146] have proposed that damage clusters could be larger under some circumstances, and on the other hand, Mueller et al [155] have argued that the clusters are no more than 5 nm in diameter. Mueller's conclusion is drawn from calculations based on a model similar to that shown in figure 55, and on (apparently unpublished) transmission electron micrograph experiments. In figure 55, the size of the damaged regions can be inferred from the fact that the tic marks on the axes are 10 nm apart. The initial energy of the primary Si recoil atom here is 50 keV, the same as in the calculation shown in figure 54. Qualitatively, the electrical effects of neutron bombardment in Si have been accounted for reasonably well using the Gossick cluster model. However, characterizing the details of the actual microscopic nature of the damaged regions is still an active research area.

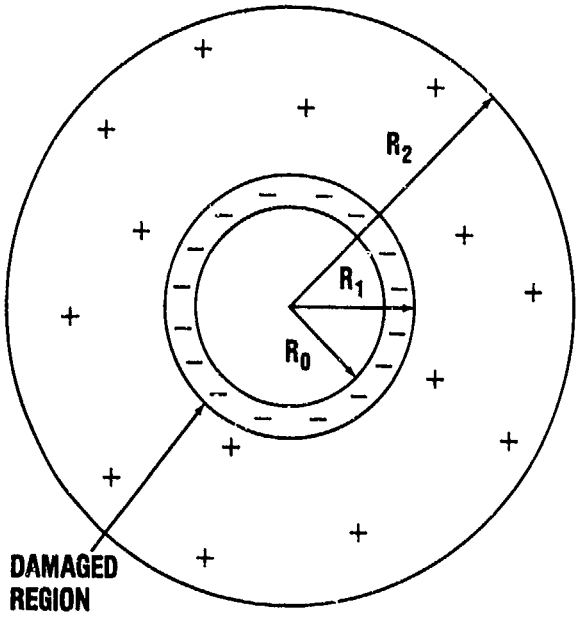

Figure 53. Gossick model for defect clusters in neutron-irradiated n-type Si [5].

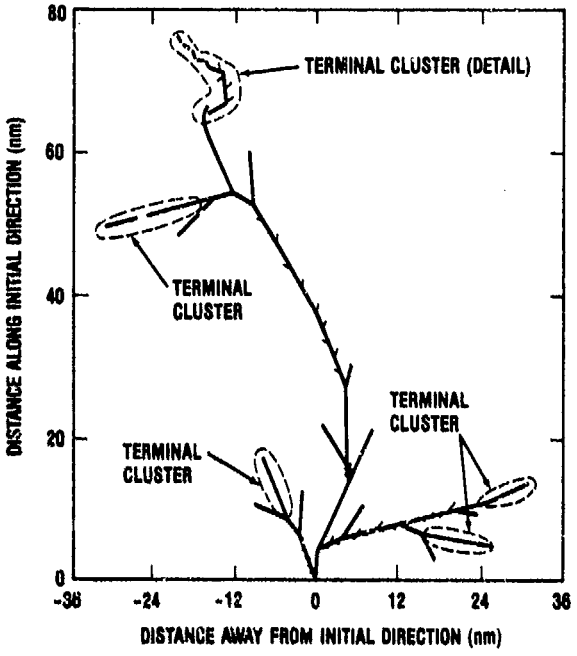

Figure 54. Typical recoil-atom track with primary energy of 50 keV [154].

5.2 Effects on Electrical Properties

Now we come to the question of how the presence of defect centers affects the electrical properties of the semiconductor. The existence of the

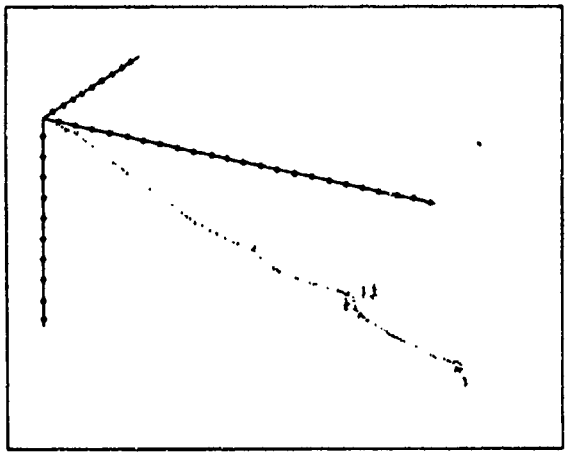

Figure 55. Different picture of typical recoil-atom track with primary energy of 50 keV. Tic marks on axes are 10 nm apart [155].

forbidden bandgap in a semiconductor is a consequence of the periodicity of the lattice. The existence of any defect disrupts the periodicity of the lattice, giving rise to a localized state in the bandgap. In figure 56 we illustrate five different effects which can be caused by localized states in different parts of the bandgap [5]. First, levels near midgap serve as thermal generation centers for electron/hole pairs, leading to increased dark currents in circuits. Second, other localized states lying in the midgap region can serve as recombination centers, shortening minority carrier lifetimes and reducing the gain in bipolar transistors. Third, shallow-trap levels near the band edges can trap charges temporarily, reemitting them in response to thermal excitation. Both majority and minority carriers undergo trapping, but at different levels. This process reduces the charge transfer efficiency in charge-coupled devices (CCD's). Fourth, deep radiation-induced trap levels can compensate the majority carriers, leading to the carrier removal process. In the example in figure 56, deep acceptors compensate the donors near the band edge. Fifth, trap-assisted tunneling can lead to increased junction leakage current when a carrier tunnels halfway through a barrier to a trap state. Two short tunneling steps are much more likely than a particle tunneling all the way through the barrier. A sixth process, not shown, is that the defects act as scattering centers. This process leads to the reduction of carrier mobilities.

The most important consequences of these effects in semiconductors are reduction of minority

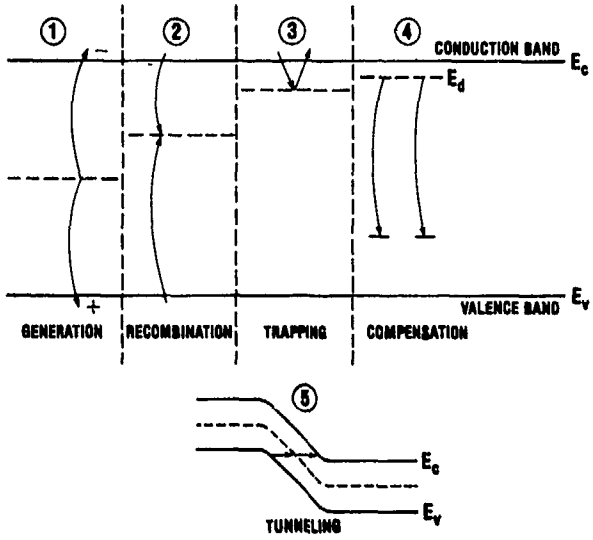

Figure 56. Five effects that can occur because of presence of defect centers in forbidden gap [5].

carrier lifetime, carrier removal, and mobility degradation. In figure 57 we illustrate the relative sensitivity of minority carrier lifetime, carrier concentration, and mobility to neutron irradiation and displacement damage [5]. For bipolar devices, minority carrier lifetime reduction is the most important effect. The longer the initial lifetime is, the more sensitive the devices are. This point is illustrated by curves for 10-μs and 10-ns initial lifetimes. Even with the shorter initial lifetime of 10 ns, significant lifetime reduction would be expected by a total neutron fluence of 10^{12} n/cm^2. For MOS and GaAs devices, on the other hand, minority carriers do not play a significant role. For these devices, carrier removal and mobility reduction are the most

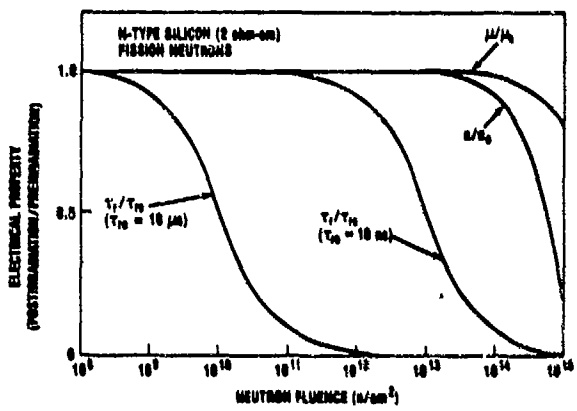

Figure 57. Relative sensitivity of lifetime, carrier concentration, and mobility to neutron bombardment. Two values of preirradiation lifetime are shown [5].

important effects. These effects become significant only at 10^{14} or 10^{15} n/cm^2, or even higher levels.

5.2.1 *Time-Dependent Annealing of Damage*

Next we come to our fifth question: how much and how fast does annealing of displacement damage occur? In general, displacement damage annealing is broken into two parts—short-term annealing and long-term annealing (see fig. 58 [5]). The short-term annealing factor at time t is degradation at time t divided by the "permanent" degradation. Annealing occurs because the defects tend to move around by diffusion and recombine or otherwise repair themselves, but the effectiveness of these processes decreases rapidly with time. Indeed, short-term annealing is usually complete within about one minute, with remaining damage considered "permanent." Actually, the permanent damage also anneals (long-term annealing), but much more slowly. In figure 58, about half the "permanent" damage observed at one minute has recovered by one year. To illustrate the early time annealing effects, we show in figure 59 some typical annealing curves for p-type Si samples exposed to two different kinds of neutron sources [156]. The annealing factor is larger at early times for 14-MeV neutrons than for reactor neutrons, indicating a higher defect interaction rate for the 14-MeV neutrons. In all cases the annealing rate becomes small for $t \gtrsim 10^2$ s.

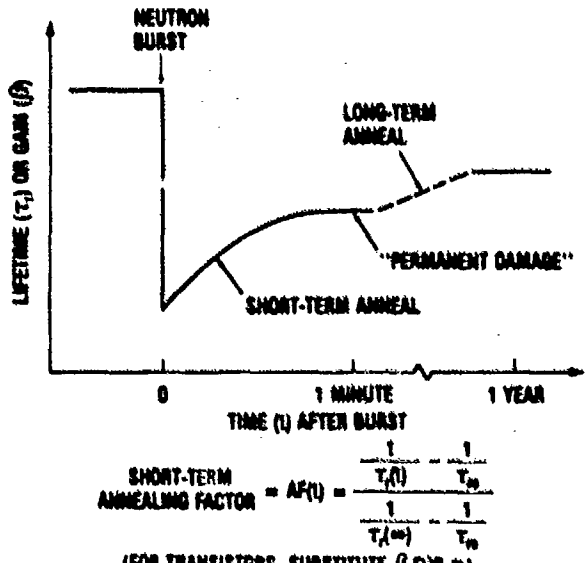

Figure 58. Room-temperature annealing: short- and long-term recovery processes in neutron-irradiated Si [5].

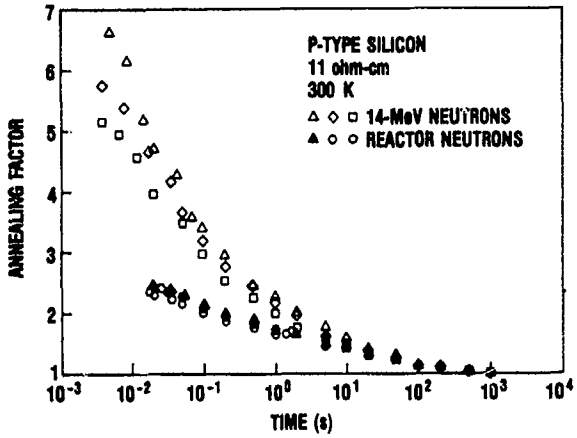

Figure 59. Short-term damage annealing in neutron-irradiated silicon: annealing factors as a function of time for different neutron sources [156].

5.2.2 Long-Term Damage

The sixth question in our initial question list has to do with how much stable displacement damage is caused under a given set of conditions. Long-term displacement damage is expressed in terms of damage coefficients which depend on a large number of variables: particle type, particle energy, material type, resistivity (doping level), injection level, and temperature. In general, the postirradiation value of a parameter (or its reciprocal) is given as the preirradiation value plus a damage coefficient times the incident particle fluence. Several examples of neutron damage coefficients for Si are given in list 6, taken from Srour [5]. We do not discuss in any detail how these coefficients depend on the many relevant variables. However, we do present three examples (fig. 60 to 62) to illustrate how important some of the variables are.

List 6. A number of long-term neutron damage coefficients for silicon.

Recombination lifetime: $\tau_r^{-1} = \tau_{r0}^{-1} + \phi/K_r$
For N-type, low resistivity, and low injection:
$K_r \cong 10^8$ n-s/cm^2 (reactor neutrons)
$K_r \cong 4 \times 10^6$ n-s/cm^2 (14-MeV neutrons)

Generation lifetime: $\tau_g^{-1} = \tau_{g0}^{-1} + \phi/K_g$
For N-type and P-type:
$K_g \cong 7 \times 10^6$ n-s/cm^2 (reactor neutrons)
$K_g \cong 3 \times 10^6$ n-s/cm^2 (14-MeV neutrons)

Carrier removal: n(post) = n(pre) − $(\Delta n/\Delta\phi)\phi$
For N-type, $N_d = 10^{16}$ cm^{-3}, reactor neutrons:
$\Delta n/\Delta\phi \cong 6$ n^{-1} cm^{-1}

Mobility: $\mu^{-1} = \mu_0^{-1} + K_\mu\phi$
For 2 ohm-cm, N-type and P-type, reactor neutrons:
$K_\mu \cong 3 \times 10^{-19}$ V-s/n

Figure 60 shows how relative displacement damage varies as a function of neutron energy [157]. Many practical neutron sources have average energies around 1 MeV, but there are many sharp peaks and valleys in the relative damage function around 1 MeV. A small difference in energy between two sources can easily lead to a difference of a factor of two or three in damage.

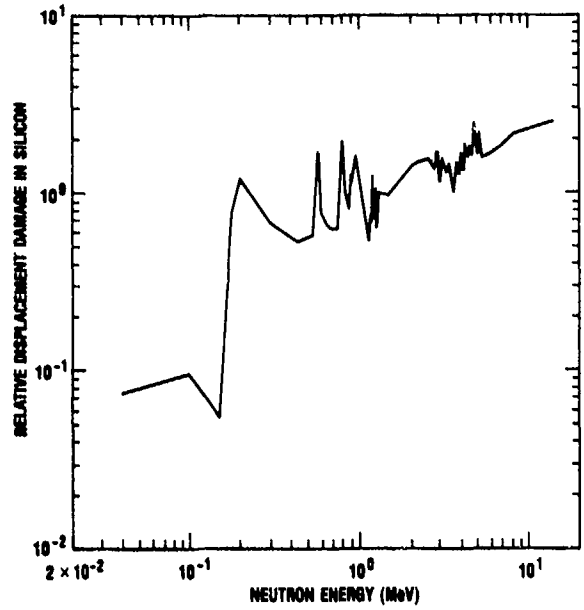

Figure 60. Neutron energy dependence of displacement damage in Si [157].

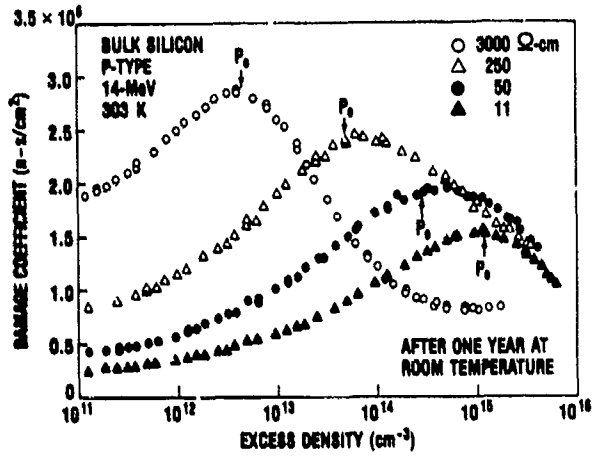

Figure 61. Injection level dependence of long-term recombination lifetime damage coefficient for 14-MeV irradiated p-type Si [158].

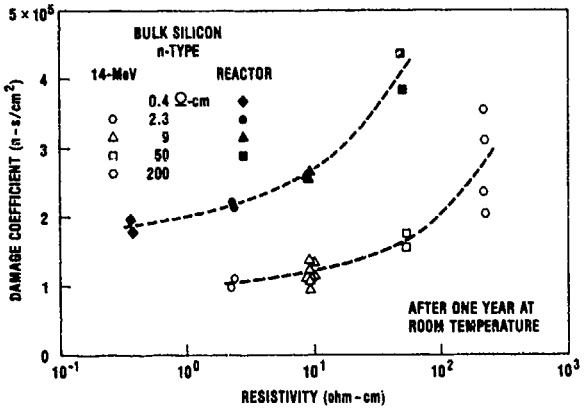

Figure 62. Resistivity dependence of low-injection-level permanent lifetime degradation for different neutron sources [158].

For this reason it is probably even more important to characterize accurately a neutron spectrum than to characterize other radiation source spectra.

In figure 61 the recombination lifetime damage coefficient is plotted as a function of carrier injection level for samples of several resistivities [158]. The peak in each curve occurs when the injection level is equal to the doping density. This figure illustrates the point that the relevant variables interact in complicated ways. The differences between, say, the open circles and solid circles are due to differences in doping level. But the curves cross, so one cannot even make a general statement that damage is greater (or less) in more highly doped material. The answer depends on something else—in this case, carrier injection level.

In figure 62 we show typical damage coefficients for n-type Si of several resistivities one year after irradiation with 14-MeV neutrons or reactor neutrons [158]. These results illustrate again how parameters interact—the resistivity makes an important difference. A great deal of work exploring the effects of various factors on neutron-induced displacement damage in Si was published in the IEEE Transactions on Nuclear Science [11] in the 1960's and early 70's. However, we do not discuss these effects any further here.

5.3 Effects on Device Characteristics

Finally, we come to our seventh and last question: what impact do displacement effects have in device physics? Probably the most important effect—the one receiving the most attention over the years—is that of bipolar transistor gain degradation due to reduction of minority carrier lifetime. Here we present just one example, the degradation of current gain of a discrete bipolar transistor exposed to several neutron fluences up to 5.6 × 10^{13} n/cm² (1 MeV equivalent). In figure 63, we show experimental points showing that the gain is reduced by about an order of magnitude for the largest fluence, depending somewhat on the operating temperature [159]. The solid curves are theoretical predictions, and they agree quite well with the experimental results.

Because transistor gain is approximately proportional to minority carrier lifetime divided by carrier transit time through the base region, the effect of gain degradation is decreased by the use of devices with narrow base regions. For this reason, present-day scaled-down IC bipolar transistors are much less susceptible to neutron irradiation than the old discrete devices. Other displacement damage effects in Si bipolar devices that have received some attention include increase in leakage currents due to the introduction of generation centers in reversed bias junctions, and carrier removal effects which lead to decreased punch-through voltages and increased collector resistance [5].

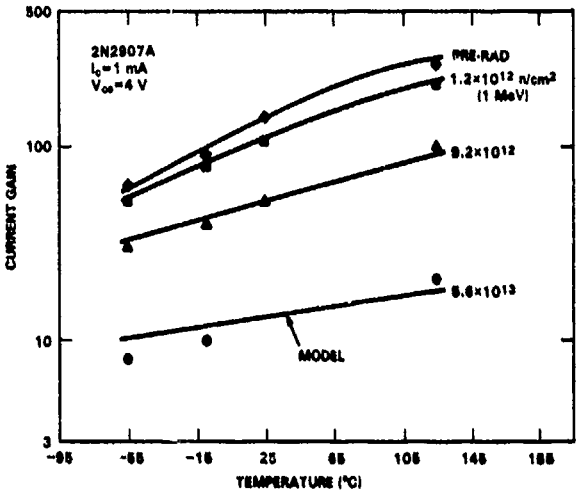

Figure 63. Typical gain degradation in bipolar transistor irradiated with three different 1-MeV equivalent neutron fluences [159].

6. Radiation Effects in Gallium Arsenide

GaAs is a semiconducting crystalline material like Si, and therefore is subject to the same basic radiation effects that occur in Si, namely, ionization and atomic displacements. However, there are some different consequences of the basic radiation effects on the electrical characteristics of GaAs devices, which lead to qualitatively different radiation susceptibilities. In a nutshell, the total dose ionization hardness of GaAs devices is generally very good, because GaAs technologies do not employ gate oxides; neutron effects (displacement damage) are considerably smaller, because lifetime degradation is generally unimportant in GaAs technologies; and transient radiation effects (both $\dot{\gamma}$ upset and SEU) in GaAs are roughly comparable to the harder Si technologies. Thus, it can be generally asserted that the overall radiation hardness of GaAs circuits is superior to the Si-based circuits. It cannot be said, though, that GaAs is immune to radiation effects, particularly with respect to transient upsets. The hardness levels for present day state-of-the-art GaAs devices can be approximately stated as follows:

10^7 to 10^8 rad(GaAs) for total ionizing dose;

10^{10} to 10^{11} rad(GaAs)/s for transient upset;

$\sim 10^{-7}$ errors/bit-day for single-event upset; and

$\sim 10^{15}$ n/cm^2 for neutron displacement damage.

We now discuss each of the radiation susceptibility categories in a little more detail for GaAs, indicating some of the primary radiation effects problems of concern. For further information on radiation effects in GaAs devices and circuits, the reader is referred particularly to the recent review article by Zuleeg [160].

6.1 Total Ionizing Dose

The insensitivity of GaAs to total ionizing dose—at least for permanent effects—is due to two factors: (1) the absence of gate insulators in GaAs devices, and (2) the absence of parasitic current leakage paths under field/passivation insulators due to the difficulty of inverting GaAs surface regions. This latter factor is a result of very high interface-state densities present (before irradiation) in all GaAs/insulator interfaces; effectively, the Fermi level at an interface is pinned at a fixed constant value by the high N_{it} density. This is precisely the reason it has not been possible to fabricate good GaAs metal-insulator-semiconductor (MIS) devices. (It should also be noted with respect to the first factor that Si junction field-effect transistor (JFET) technology, which also does not use gate oxides, also enjoys a higher tolerance to total dose than other Si technologies.)

The high total-dose insensitivity of GaAs is clearly illustrated in figure 64, which shows experimental results [161] of $I_{DS}^{1/2}$ versus V_G for an epitaxial enhancement-mode GaAs JFET before irradiation (dark circles) and after exposure to an ionizing radiation dose of 10^6 rad(GaAs) (open circles). Before the irradiation, $V_T = 0.42$ V, and after exposure $V_T = 0.425$ V, essentially a null effect. Also shown (triangles) are the results after neutron irradiation to 1.7×10^{13} n/cm^2. In this case there is

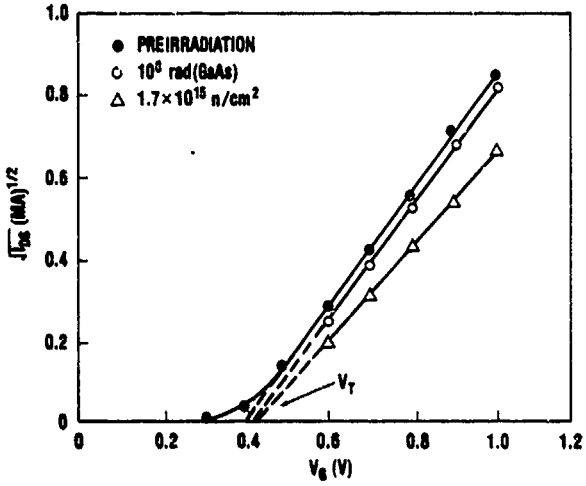

Figure 64. Effect of irradiation on I_{DS}-V_G characteristic of epitaxial GaAs JFET with channel region doping density of $10^{17}/cm^3$ [161].

still only a small shift in V_T, but there is a noticeable change in the slope of the curve, or transconductance. We return to this point in section 6.3.

Even though GaAs devices are basically immune to long-term total-dose effects, a transient effect has been observed [162] which is associated with ionizing radiation-induced charging of Cr-doped semi-insulating (SI) GaAs substrates which have been widely used in GaAs FET structures for isolation purposes. This substrate charging causes a reduction in the drain current of the transistor with observed time constants as large as seconds. The effect on I_{DS} is depicted in figure 65, which shows I_{DS} normalized to its preirradiation value plotted versus time following 100 rad(GaAs) of pulsed (3-ns) 600-keV x-ray irradiation for a series of initial I_{DS} values [162]. These I_{DS} transients are characterized by peak reductions in current amplitude ranging from 90 percent of the quiescent current at 0.5 mA to less than 5 percent at the 10-mA level. The recovery time constants associated with these data are in the range from 10 to 14 s.

A schematic model [163] indicating the cause of the transient reduction in I_{DS} is shown in figure 66. A net negative charging of the SI substrate is depicted which induces a backgate depletion region in the p-GaAs epitaxial layer (n-channel region) next to the interface with the substrate. This induced depletion region then reduces, or pinches, the electron current flow in the n-channel. The substrate charging was attributed [162,163] to electron

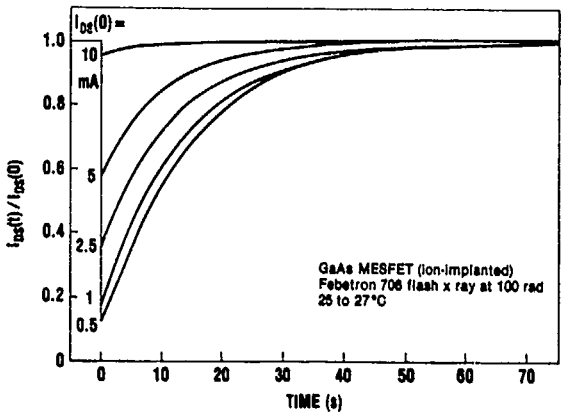

Figure 65. Pulsed radiation response characteristics at various I_{DS} levels of GaAs MESFET (metal epitaxial semiconductor FET). [162].

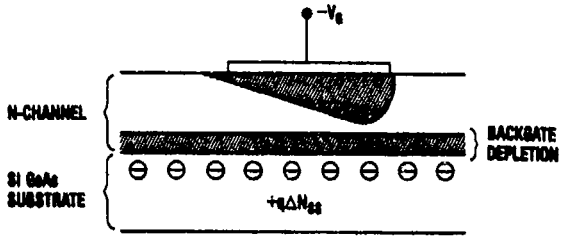

Figure 66. Schematic cross section of gate region of GaAs FET, indicating effect of transient substrate charging [163].

trapping in deep trap levels associated with the Cr impurities. Based on the time constants for the discharge of the traps (recovery of I_{DS}), the energy level of the traps was determined to be ~0.8 eV. The transient charging problem can be avoided by using carefully prepared intrinsic SI GaAs substrates having low impurity concentrations [164] or by the use of a conducting p-GaAs buffer layer [163,165] between the active channel and SI substrate.

6.2 Transient Radiation Effects

In principle, GaAs devices should be somewhat harder to transient $\dot{\gamma}$ upset than SI devices because of shorter minority carrier lifetimes. But because upset levels in practice are strongly dependent upon circuit configuration (geometric layout as well as electrical), the actual upset levels in GaAs circuits are generally comparable with the harder SI technologies [166].

Based on extensive experimental work and analysis, Zuleeg et al [167] argue that the upset lev-

els in GaAs JFET's with channel lengths below ~1 μm are dominated by shunt currents between the source and drain through the SI substrate. This is indicated by I_{ps} in figure 67, which schematically illustrates the shunt current effect. The currents I_{pp1} and I_{pp2} are the usual junction photocurrents, and these dominate the upset levels for devices with longer channel lengths. In effect, the normally high-resistivity SI substrate becomes conducting because of the induced carrier densities from ionization in the substrate, and offers a low-resistance shunt path for currents between the source and drain regions. For a 1-μm channel length, the predicted upset rate due to the shunt substrate current is ~5×10^{10} rad(GaAs)/s.

The charge collected at a Schottky junction diode on a semiconducting GaAs substrate following a single energetic particle strike is qualitatively similar to the charge collection in the corresponding SI structures. The prompt charge collection, enhanced by the field funneling effect (see sect. 4.3), seems to be fairly well described [168] by the effective funnel length model of McLean and Oldham [137], originally developed to describe charge collection due to alpha-particle strikes through SI Schottky junction diodes. So apparently the same physics (underlying the funnel effect) is operative in both GaAs and SI diodes that are on purely semiconductor substrates. However, for GaAs diodes that are fabricated on a GaAs epitaxial layer on top of a doped SI GaAs substrate—corresponding to the more usual present-day technology configuration—there is a significant reduction in the observed charge collection, both total and prompt, from that in diodes fabricated on semiconductor substrates [169]. This effect is illustrated by the data in figure 68, which, over the bias range shown,

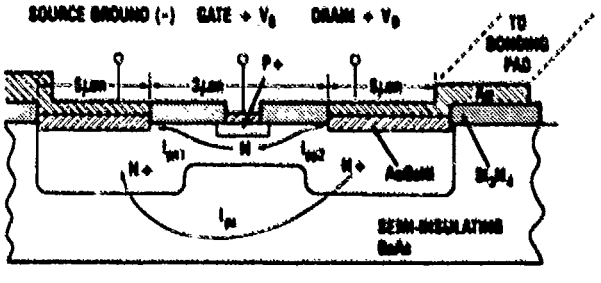

Figure 67. Cross section of enhancement mode GaAs JFET indicating source-drain shunt current path through semi-insulating substrate [167].

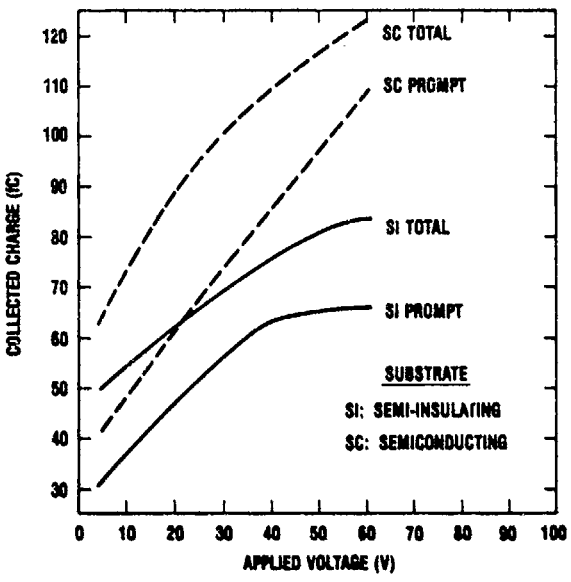

Figure 68. Comparison of alpha-particle-induced charge collection for diodes fabricated on semiconductor substrates and semi-insulating substrates [169].

indicate about a 40-percent reduction in the amount of charge collected in the diodes on an SI substrate, compared with those on a semiconducting (SC) substrate. The mechanism responsible for the reduced charge collection is the same as that responsible for the transient substrate charging effect discussed in the previous subsection, namely, long-term trapping of the radiation-induced carriers in the doped SI substrate at deep trapping levels, most likely associated with the Cr impurities. In the single-event case, the deep level trapping is helping matters by reducing the prompt charge collection. To date, comparable single-event-induced charge-collection experiments for epitaxial layer GaAs diodes fabricated on intrinsic (undoped) SI substrates have not been carried out.

6.3 Displacement Damage Effects

Minority carrier degradation due to displacement damage is not important in GaAs devices, either because of the short initial (preirradiation) carrier lifetimes for bipolar GaAs technologies or because the devices are majority carrier devices for FET technologies. The transistor gain degradation in either kind of device is due primarily to carrier removal and mobility degradation. The change in the transconductance of a JFET due to these effects following neutron exposure to 1.7×10^{15}

n/cm^2 was already noted in figure 64. A detailed analysis of the neutron-induced degradation in transconductance for JFET's operating in the hot-electron regime was carried out by Behle and Zuleeg [170], and the results for the transconductance normalized to its initial value are shown in figure 69 plotted against neutron fluence for three different channel doping concentrations. Experimental results for GaAs JFET's with a channel doping of approximately 1×10^{17} cm^{-3} are shown by the circles in the figure, in good agreement with the predictions of the analysis.

We briefly note in concluding this section the primary displacement-damage-induced degradation in some other important classes of GaAs devices. GaAs is used extensively in optoelectronic devices, and these devices degrade by the introduction of nonradiative recombination centers, which lead, for example, to a decreased efficiency in GaAs light-emitting diodes. Carrier removal is the prime degradation mechanism in GaAs charge-coupled devices, leading to reduction in the charge transfer efficiency. The so-called novel GaAs device structures (devices such as high-electron-mobility transistors—HEMT's—and modulated doping FET's—MODFET's) which depend for their operation on layers of high electron mobility may degrade seriously because of mobility reduction induced by displacement damage.

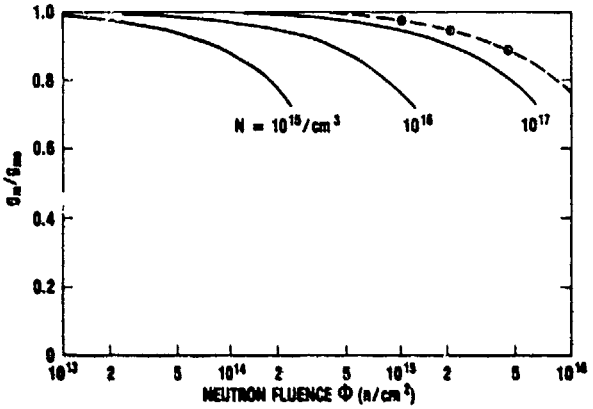

Figure 69. Calculated normalized transconductance versus neutron fluence for GaAs JFET's operating in hot-electron range for three channel doping concentrations. Experimental results for channel doping of 1×10^{17}/cm^3 shown by circles [170].

7. Temperature Effects

Temperature affects to some degree just about all physical properties and processes. As such, the broad subject of temperature effects is far beyond the scope of our present discussion, and hence we do not discuss here temperature effects per se. The temperature dependence of electronic material properties (such as carrier mobilities, concentrations, and lifetimes, electrical conductivities and resistivities, bandgap widths, thermal conductivities) and of device/circuit characteristics (transistor gains, threshold voltages, turn-on speed, leakage currents, noise levels) are discussed in most standard textbooks [13–16]. Further, the important role of temperature in reliability/wearout issues (such as redistribution of dopants and diffusion of impurities, enhanced electromigration, contact stability, dielectric breakdown, thermal expansion strains, and so on) is addressed in many conferences and journals devoted to reliability matters.

Rather, in this final section, we confine our discussion of temperature effects to some brief remarks in several areas where there is a close relationship between temperature and the basic mechanisms of radiation effects. Our discussion is not meant to be exhaustive, but simply to provide a feeling for the kinds of temperature-related effects that bear upon radiation response. First, we discuss some examples in which temperature is a major physical parameter determining the radiation response. Then we consider radiation-induced thermal effects and synergistic effects of combined radiation and thermal stresses. Last we briefly mention the reliability problem of hot carrier injection in MOSFET's. This latter problem is currently receiving a lot of interest, and even though it really is more of a high field problem than temperature related, we include it here because many of the electrical effects of hot carrier injection parallel those resulting from irradiation.

7.1 Effect of Temperature on Radiation Response

The first point we make here is the perhaps physically intuitive one that increasing the temperature generally enhances the annealing of radiation damage. For example, at higher temperatures, the short-term recovery in MOS devices is faster (see fig. 14), and the annealing rate of long-term deeply trapped holes increases. For this latter effect, note the increased recovery of ΔV_{ot} at 125 °C over that at 25 °C in figure 27. Although enhanced annealing is generally beneficial, it may not always bring welcome results, as also illustrated by figure 27. For the case in point, the response data shown in figure 27 are for a MOSFET with an appreciable radiation-induced interface trap density ($\Delta N_{it} \approx \Delta N_{ot}$), and hence there is a large rebound effect (reversal in the sign of ΔV_T) as the trapped holes anneal. So in this case, enhancing the trapped hole anneal brings on the rebound effect sooner, and if a sufficient positive-going excursion of V_T can result in circuit failure, then figure 27 predicts the faster onset of this failure mode at higher temperature.

The second point we want to make is a further word of caution: hardening schemes that are developed to improve the radiation response of a circuit

in one temperature regime (e.g., near room temperature) may utterly fail in other temperature regimes. The rebound effect serves as one such example if at room temperature one is depending on interface trap buildup to offset the positive trapped oxide charge, so that only a small net change is produced in V_T. Although this scheme may work over some considerable time regime at room temperature, it rapidly falls apart at elevated temperature. Another example is that of a hardening scheme first proposed a few years ago to reduce the single-event-upset rate: that of placing appropriately chosen resistances in the cross coupling links of a static memory cell to decrease the circuit response time and thereby reduce the sensitivity of the cell to a sudden and rapid current pulse [171]. Some of the earlier attempts at using this scheme employed intrinsic polycrystalline silicon as the coupling resistors. However, the resistivity (or conductivity) of an intrinsic bandgap solid depends upon the number density of carriers thermally excited across the energy bandgap, and therefore has an Arrhenius-type temperature dependence with an activation energy of half the bandgap [13–15]. This is clearly shown by the plot in figure 70 of the resistance of an intrinsic polysilicon sample versus reciprocal temperature [172], in which an activation energy of 0.59 eV is indicated, as expected for intrinsic silicon. The point here is that if the resistance value is chosen to reduce the SEU error rate to an acceptable level at room temperature, then it may be far off the mark to insure an acceptable SEU error rate at a different temperature. Note, for example, in figure 70 the two orders of magnitude difference in the resistance values between 27° and 100°C. The problem associated with the strong temperature dependence of intrinsic polysilicon resistivity has a simple solution, namely, the use instead of doped polysilicon material, which has a much flatter temperature dependence [172].

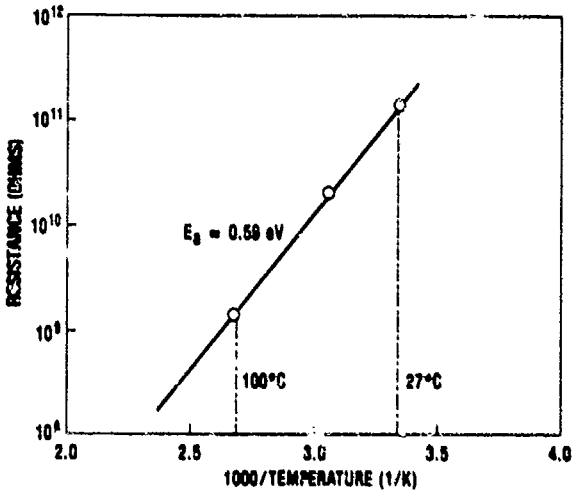

Figure 70. Experimentally measured load resistance versus reciprocal temperature for intrinsic polysilicon resistor, indicating activation energy of 0.59 eV [172].

Another problem also originating from a fundamental materials property and which is not so easily solved has to do with the use of SiO_2 MOS devices at low (cryogenic) temperatures. There is a considerable interest in such applications either for CCD's or for normal MOSFET purposes. The advantage of low-temperature MOSFET applications is illustrated by the subthreshold I_{DS}-V_{GS} characteristics [173] shown in figure 71 for an NMOS device at two temperatures, 300 and 77 K. The low-temperature characteristic is considerably sharper, implying a much faster and sharper turn-on of the device at 77 K. Furthermore, at cryogenic temperatures, CMOS devices are essentially immune to latchup, carrier mobilities are higher, and metal interconnects have lower resistance.

However, in spite of all these advantages for low-temperature operation of SiO_2 MOSFET's, the catch is that severe problems arise if the devices are also exposed to ionizing radiation at low temperature. Indeed, even if the devices were superhardened for room-temperature operation by some special processing which virtually eliminates all deep hole traps and interface traps, enabling the device to continue operating after exposure to

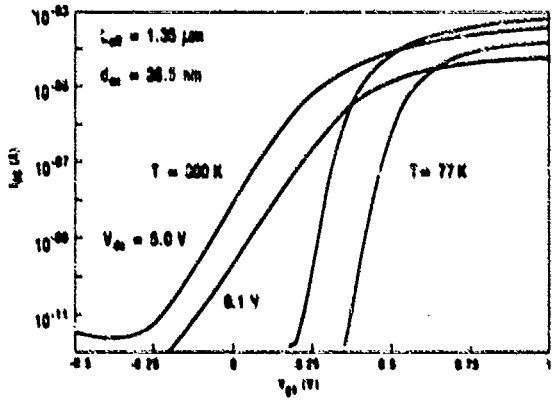

Figure 71. I_{DS} versus V_{GS} characteristics of a surface channel NMOS device at 300 and 77 K [173].

many Mrad(SiO_2), it would provide no advantage at low temperatures—exposure to radiation at low temperature would still result in the maximum possible threshold voltage shift, that given by equation (5) of section 3.3.1. In effect, one is up against a basic material property, namely the effective immobility of holes in SiO_2 at low temperatures. At these temperatures all (SiO_2) oxides are soft. Referring back to figure 14, we see that for a typical operating field of 1 MV/cm, virtually no recovery in ΔV_{fb} takes place for $T \lesssim 140$ K on a time scale of thousands of seconds. The holes remain frozen in place very near their points of generation. Now, as the field is raised beyond ~3 MV/cm, some transport does occur at low temperature on this time scale, as figure 15 shows for T = 79 K. In this case, almost complete recovery is attained at 10^3 s for a field of 6 MV/cm. However, no one really contemplates the practical use of MOS devices at these kinds of fields.

The low-temperature problem in SiO_2 MOS devices is further illustrated by the data in figure 72 from Srour and Chiu [174], showing the flatband voltage shift of 91-nm oxide MOS capacitors at 77 K and room temperature, as a function of applied gate voltage measured 1 hour following 10^5 rad(Si) exposure to Co^{60} irradiation. The oxide here is relatively hard at room temperature, having a deep hole trapping fraction of ~0.05; however, the greatly increased hole trapping at 77 K is obvious. We note that the initial rapid increase in ΔV_{fb} at 77 K with applied bias (either polarity) reflects the increasing yield of holes (that escape initial recombination) with oxide field—see figure 12. The

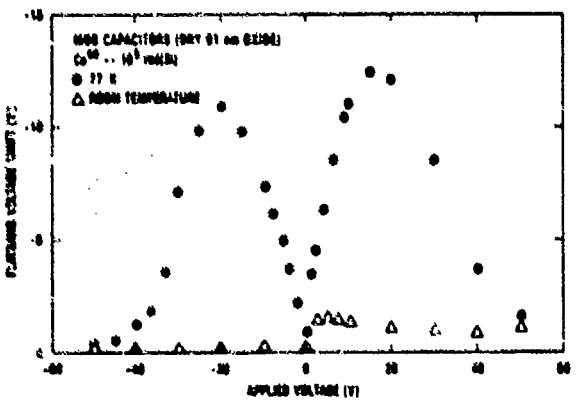

Figure 72. Flatband voltage shift versus gate voltage applied during irradiation for MOS capacitors irradiated at both 77 K and room temperature [174].

turnaround in ΔV_{fb} beyond ~ ± 20 V is explained by the increasing amount of hole transport occurring for increasing oxide field (compare fig. 15), with $\Delta V_{fb} \rightarrow 0$ at ± 50 V, corresponding to an oxide field of ~6 MV/cm. The principal message of figures 72, 14, and 15 is that there is a serious problem with the use of SiO_2 MOS devices at low temperature. In practice, either alternative insulators must be used such as Si_3N_4, or some special low-temperature hardening scheme must be used, which may involve a double-layer oxide structure which compensates the trapped holes by also trapping electrons very efficiently [175].

Before we go on, several other noteworthy points can be made about the data in figure 72. First, the virtually zero voltage shift under negative applied bias at room temperature supports the assertion that most of the deep hole trapping occurs near the SiO_2/Si interface and not in the SiO_2 bulk. Under negative bias, the holes are driven toward the gate electrode, where they may also be trapped, but then they have little effect on the field at the SiO_2/Si interface. Second, the fall-off in ΔV_{fb} at room temperature with increasing positive polarity probably reflects the $E_{ox}^{-1/2}$ dependence of the hole-trapping cross section (see sect. 3.3.3), but with the increase again at ~50 V probably due to additional holes being generated by impact ionization events at this high field [176]. Finally, the asymmetry in the peak of ΔV_{fb} at 77 K between positive and negative polarity has been attributed by several authors [20,35,78,174] to an initial (intrinsic) prompt hole transport over a distance of ~10 nm, which occurs in a subnanosecond time frame before the holes become immobilized in the self-trapped (polaron) states. This effect is not so important for relatively thick oxides ($d_{ox} \gtrsim 30$ nm) but should be very important for thin oxides where $d_{ox} \lesssim 10$ nm.

7.2 Radiation-Induced Heating Effects

We now discuss some effects that occur when there is appreciable heating of a material induced by the energy deposition associated with the irradiation, as may occur with a high-dose, pulsed radiation exposure. Obviously, the effects associated with increased temperature that we have just discussed, such as enhanced annealing of radiation-induced damage, will apply equally in

these situations. In addition, there may be important synergistic effects in which there are combined radiation and thermally induced parameter changes. In the simplest situations, in which the effects are just additive, we may indicate the combined effect schematically with the equation

$$\Delta_{total} = \Delta_{rad} + \Delta_{thermal}\,, \tag{13}$$

where Δ refers to the change in some physical quantity and the subscripts are self-explanatory. Some physical quantities for which equation (13) may apply, at least in some limited dose and temperature ranges, include MOSFET threshold voltage, bipolar transistor gain, leakage currents, and circuit noise levels.

As just one case in point, we consider the MOSFET threshold voltage. In section 3, we devote considerable attention to radiation-induced threshold voltage shifts. However, it is well known that V_T also changes with temperature, an effect which is discussed in most textbooks on electronic devices [13–16]. The temperature dependence of V_T is shown in figure 73, which is taken from Sze [13] following earlier published work [177,178]. In figure 73a, the shift in V_T relative to its room temperature value for a MOSFET with a gate oxide thickness of 100 nm is plotted against temperature over the range −50° to 125°C for three doping densities, and in figure 73b the temperature coefficient of V_T at room temperature (dV_T/dT) is plotted versus substrate doping density with oxide thickness as a parameter in the range from 0.05 to 1 μm. These plots are based on the temperature dependencies of parameters that go into the standard expression for V_T. We make the following point concerning figure 73: note that V_T shifts negatively with increasing temperature. Suppose for the sake of argument that the higher substrate doping sample (3×10^{16} cm^{-3}) in figure 73(a) received a radiation pulse that induced a voltage shift of −0.5 V (after the hole transport phase) and that because of the energy deposition by the pulse, the temperature of the MOSFET rose by 100°C (from ~25° to ~125°C); then there would be an additional negative shift in V_T of ~ −0.5 V, producing a total shift due to the combined radiation and thermal effects of −1.0 V.

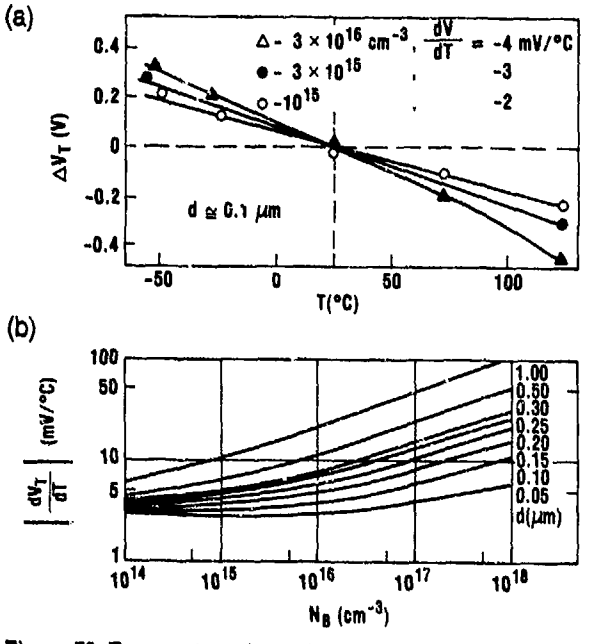

Figure 73. Temperature dependence of MOSFET threshold voltage: (a) Experimental measurement of threshold voltage versus temperature for three doping densities. (b) Temperature coefficient of V_T versus substrate doping with oxide thickness as a parameter [13, 177, 178].

Another radiation-induced heating effect that has received a fair amount of practical attention is the so-called thermomechanical shock problem [179–182]. This effect occurs under conditions of very rapid energy deposition (high fluence, pulsed irradiation), where the pulsewidth of the irradiation is less than the acoustic relaxation time, which is essentially the time required for a sound wave to traverse the region of energy deposition (the time required for relaxation of thermally induced strains associated with the rapid heating). In effect, propagating stress waves can originate from regions having large gradients in the thermally induced internal pressure. In practice, large stress gradients can be produced in regions near boundaries between dissimilar materials, especially between materials with large differences in their atomic numbers (high-Z/low-Z boundaries), so that there is a large difference in the energy deposition (and hence internal pressure) on the two sides of the boundary. The stress waves originating from such regions can propagate through solid systems (IC chips), producing damage such as broken contact and die bonds and chip fracture.

A simple schematic illustrating the generation of thermomechanical stress waves is shown in

figure 74, where we consider a single material slab sample (infinite extension in y and z) having a free surface boundary (with air or vacuum) on which a short pulse of radiation is incident. Associated with the irradiation is an energy deposition profile $\Delta E(x)$ extending into the bulk of the sample from the surface, as indicated in the top diagram of figure 74 for time $t = 0^+$. Along with the local increase in internal energy of the solid, there is a corresponding local temperature rise $\Delta T(x)$ related to $\Delta E(x)$ through the specific heat at constant volume C_V and the density ϱ. We assume that the pulsewidth τ_p of the radiation is much less than the acoustic relaxation time, which in this case is just ℓ/v_s, where ℓ is the spatial extent of the energy deposition and v_s is the velocity of sound in the material. Then, because the material sample wants to expand with increasing temperature, there will be an induced internal pressure rise $\Delta P(x)$, which is proportional to $\Delta E(x)$ via the Grüneisen parameter Γ. This parameter is the thermodynamic quantity defined as the partial derivative of internal pressure with respect to internal energy at constant volume. As indicated in figure 74, Γ can be expressed in terms of other measured physical quantities: the volume coefficient of thermal expansion β, the isothermal compressibility K_T, the specific heat C_V, and density ϱ. If cgs units are used—$\Delta E(x)$ in units of ergs/cm^3 and $\Delta P(x)$ in dynes/cm^2—then typical Grüneisen values are on the order of unity.

Now, the pressure at a free surface must be zero, so that at $t = 0^+$ in this simple example, a stress discontinuity occurs at the boundary, or rather, more realistically for a finite pulsewidth, there is a large stress gradient in the surface region of the sample. In effect, the surface expands outwardly to relieve the internal pressure, and the net result is a propagating stress wave indicated schematically by the bottom diagram in figure 74 for some time $t > 0$. Note that it has both compressive and tensile components, with the tensile component originating from the reflection of a leftward-going compressive wave at the surface. Obviously the region between the compressive and tensile peaks is one of high dynamic strain. In the elastic (low stress) limit, the wave propagates at the velocity of sound.

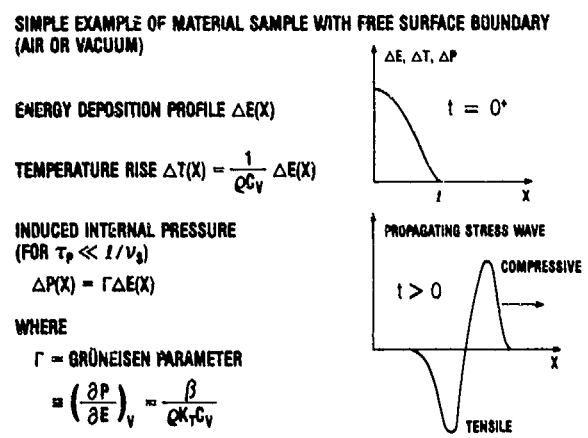

Figure 74. Thermomechanical stress generation at free surface boundary of material sample due to pulsed energy deposition, indicating initial internal pressure profile and subsequent propagating stress wave.

A very important point in discussing thermomechanical shock effects in military systems is the following: failures are due to complex multidimensional interactions. In the late 60's and early 70's, many researchers found that thermomechanical shock effects could not be modeled adequately using one-dimensional slab geometries. They were forced to two- and three-dimensional analysis to have any realistic hope of modeling actual failure mechanisms. Although many authors reached similar conclusions at about the same time, we cite only a single example [183]. This work shows that even for a monolithic disk, the largest mechanical stress occurs when the radial wave propagating in from the edge of the sample reaches the center. That is, even for a very simple structure, the two-dimensional effects are critical. Of course, structures of real interest are even more complicated, since they are seldom cylindrical and they have multiple interfaces between different materials. For simplicity, in our discussion we have illustrated some of the basic ideas using one-dimensional geometry; but a realistic and detailed treatment, which we do not pursue here, becomes exceedingly complex.

7.3 Hot Carrier Injection in MOSFET's

The last topic that we very briefly discuss in this section is that of hot carrier injection in MOSFET's. As mentioned at the beginning of the section, this is an important reliability problem associated with the long-term operation of MOS circuits, and it is receiving much attention at present from the electron device and IC communities. It is not really a

temperature problem per se, but rather it is caused by high-field heating of the carriers moving in the channel of a MOSFET. The process is indicated schematically by the diagram in figure 75 for an n-channel device [184]. As the channel carriers—electrons in this case—move along the channel in response to the drain potential V_d, they encounter a high-field region at the end of the channel in the drain depletion region. This high-field region rapidly accelerates the electrons, causing a large increase in their effective temperature in this region and some (small fraction) of these hot electrons will be injected following a scattering event into the gate oxide, where they will drift toward the gate electrode (for positive gate bias). In addition, there will be impact ionization of additional electron/hole pairs in the high-field drain-depletion region, which results in a substrate hole current as indicated in figure 75. This substrate hole current has been found to be approximately linearly proportional to the injected electron current in the oxide [185].

The basic problem associated with the injection of hot carriers into the oxide is that it induces charging of the gate oxide, in a manner analogous to that due to ionizing irradiation, and therefore likewise results in threshold voltage shifts and transconductance degradation. In the case of hot electron injection (which is a far greater problem than hot hole injection), the charging effects are due to electron trapping in the oxide bulk (which causes positive threshold voltage shifts) and to the generation of interface traps near the drain end of the channel. The main difference between this case and radiation-induced charging is that for the radiation case it is hole trapping near the SiO_2/Si interface that is of concern and, in addition for radiation, the interface traps are generated all along the channel.

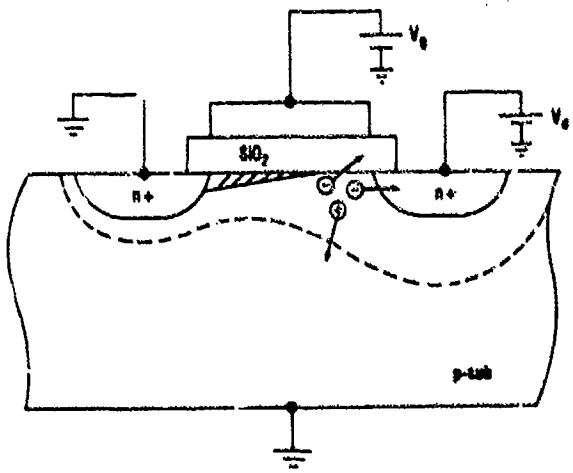

Figure 75. Schematic diagram showing process of hot electron injection in n-channel MOSFET [184].

The hot-electron-induced charging of oxide films is illustrated by the data shown in figures 76 and 77 [186]. The injected electrons for these data were produced by avalanche injection of electrons into the gate oxide of MOS capacitor structures fabricated on p-type Si substrates. Figure 76 shows the flatband voltage shift as a function of injection time for several values of injected current levels, and as a function of total accumulated injected charge, F_A. Figure 77 shows the decomposition of the oxide charge into the bulk electron trapping Q_{ot}

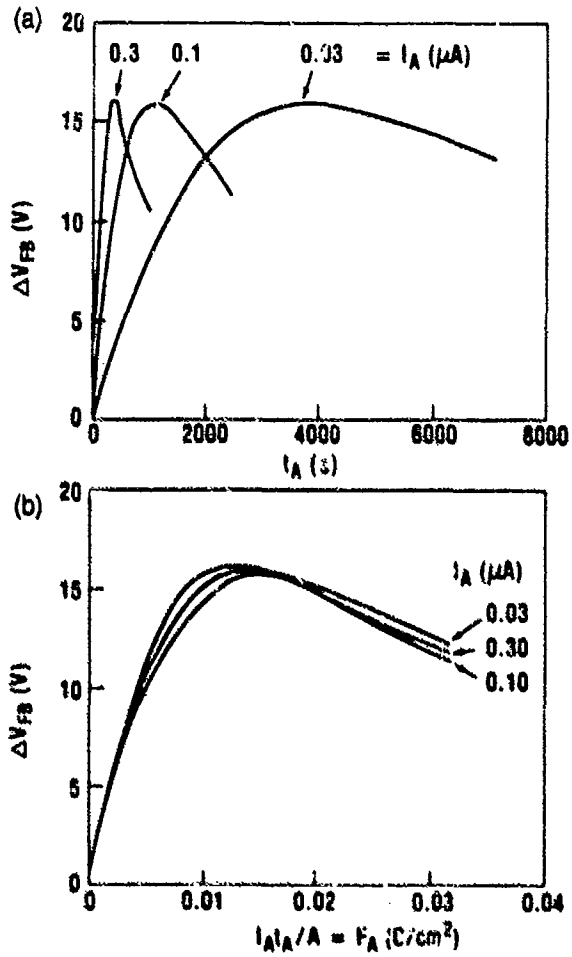

Figure 76. Oxide charging produced by avalanche injection of electrons into oxide layer of MOS capacitor: (a) Flatband voltage shift versus injection time at several current levels. (b) Same data plotted versus injected fluence [186].

and interface trapped charge Q_{it}, where the injected electron fluence was taken out to much greater levels than for figure 76. Note the turnaround in net oxide charge in this case for $F_A \gtrsim 0.1$ C/cm^2.

We do not go into any greater discussion of the hot carrier injection problem, except to end with a few general comments. First, the problem becomes more critical as device dimensions are scaled down and operating electric fields increase. Second, in a fashion reminiscent of the enhanced hole trapping in SiO_2 films at low temperature, the injection of hot electrons is actually enhanced at low temperature (77 K) [173]. This is due to longer mean free paths at lower temperature for lattice (phonon) scattering, which leads to a greater effective electron temperature (greater average energy imparted to the channel electrons). Third, with respect to radiation effects, for anticipated long-term use of a circuit, it is important that any radiation hardening effort also be compatible with minimizing hot-carrier-induced degradation [187]. Finally, also in this regard, there should be studies carried out which will establish whether radiation damage has any effect upon hot carrier injection, i.e., whether radiation-induced charging may enhance the injection.

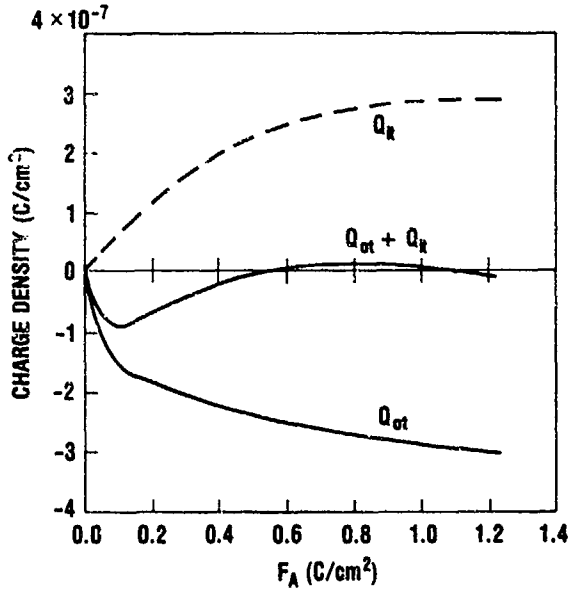

Figure 77. Net oxide charge density separated into bulk oxide trapped charge (Q_{ot}) and interface trapped charge (Q_{it}) [186].

8. Concluding Comment

In this discussion we have attempted to give an overview of the basic physical processes which determine the radiation response of electronic devices and materials. Although basic radiation effects physics remains a very active research area with many important unresolved questions, we wish to conclude by emphasizing that mechanisms research has successfully answered many questions concerning some difficult problems. For example, the prediction of the postirradiation response of MOS devices has sometimes been regarded as an impossible task because of the wide range of observed responses. However, as we highlighted in section 3, the complexity of the response exists because a number of different processes with different characteristic time scales contribute to the overall response, and it is difficult to know a priori how much effect each one will have. However, if the observed response can be broken down into the component processes which can be treated separately to some extent, then the overall response problem becomes much more manageable. By making effective use of the accumulated mechanisms knowledge of the basic processes, accurate postirradiation response predictions can usually be made with only a relatively simple set of measurements. In such a manner a certain amount of order and understanding can often be made of a complex and often confusing picture.

Acknowledgements

The authors wish to thank their colleagues, H. Edwin Boesch, Jr., Joseph M. Benedetto, and James M. McGarrity, for many helpful technical discussions while preparing this tutorial.

References

1. R. D. Evans, *The Atomic Nucleus*, McGraw-Hill, New York (1955).

2. E. Segre, *Nuclei and Particles*, W. A. Benjamin, New York (1965).

3. V. A. J. van Lint, T. M. Flanagan, R. E. Leadon, J. A. Naber, and V. C. Rogers, *Mechanisms of Radiation Effects in Electronic Materials*, volume 1, Wiley-Interscience, New York (1980).

4. J. W. Corbett, *Electron Radiation Damage in Semiconductors and Metals*, Academic Press, New York (1966).

5. J. R. Srour, *Basic Mechanisms of Radiation Effects on Electronic Materials, Devices, and Integrated Circuits*, Defense Nuclear Agency technical report, DNA-TR-82-20 (August 1982).

6. J. R. Srour, *Basic Mechanisms of Radiation Effects on Electronic Materials, Devices, and Integrated Circuits*, 1983 IEEE NSREC Short Course, Gatlinburg, TN (July 1983).

7. J. E. Gover, *Basic Radiation Effects in Electronics Technology*, 1984 IEEE NSREC Short Course, Colorado Springs, CO (July 1984).

8. D. Pines, *Elementary Excitations in Solids*, W. A. Benjamin, New York (1964).

9. M. J. Berger and S. M. Seltzer, NASA-SP Publication 3036 (1966).

10. J. F. Janni, AFWL-TR-65-150 (1966).

11. See, for example, the December issues of the IEEE Transactions on Nuclear Science (1965–1987).

12. R. C. Hughes, Phys. Rev. Lett. *30* (1973), 1333.

13. S. M. Sze, *Physics of Semiconductor Devices*, Wiley, New York (1981).

14. B. G. Streetman, *Solid State Electronic Devices*, 2nd ed., Prentice-Hall, Englewood Cliffs, NJ (1980).

15. R. S. Muller and T. I. Kamins, *Device Electronics for Integrated Circuits*, Wiley, New York (1977).

16. A. B. Glaser and G. E. Subak-Sharpe, *Integrated Circuit Engineering*, Addison-Wesley, Reading, MA (1977).

17. G. A. Ausman, Jr., and F. B. McLean, Appl. Phys. Lett. *26* (1975), 173.

18. O. L. Curtis, J. R. Srour, and K. Y. Chiu, J. Appl. Phys. *45* (1974), 406.

19. H. H. Sander and B. L. Gregory, IEEE Trans. Nucl. Sci. *NS-22* (1975), 2157.

20. H. E. Boesch, Jr., and J. M. McGarrity, IEEE Trans. Nucl. Sci. *NS-23* (1976), 1520.

21. J. M. Benedetto and H. E. Boesch, Jr., IEEE Trans. Nucl. Sci. *NS-33* (1986), 1318.

22. T. R. Oldham, J. Appl. Phys. *57* (1985), 2695.

23. M. von Smoluchowski, Ann. Phys. (Leipzig) *44* (1915), 1103.

24. L. Onsager, Phys. Rev. *54* (1938), 554.

25. G. Jaffe, Ann. Phys. (Leipzig) *42* (1913), 303.

26. P. Langevin, Ann. Chim. Phys. *28* (1903), 289; *28* (1903), 433.

27. T. R. Oldham and J. M. McGarrity, IEEE Trans. Nucl. Sci. *NS-28* (1981), 3975; *NS-30* (1983), 4377.

28. H. E. Boesch, Jr., F. B. McLean, J. M. McGarrity, and G. A. Ausman, Jr., IEEE Trans. Nucl. Sci. *NS-22* (1975), 2163.

29. R. C. Hughes, Appl. Phys. Lett. *26* (1975), 436.

30. R. C. Hughes, E. P. EerNisse, and H. J. Stein, IEEE Trans. Nucl. Sci. *NS-22* (1975), 2227.

31. F. B. McLean, G. A. Ausman, Jr., H. E. Boesch, Jr., and J. M. McGarrity, J. Appl. Phys. *47* (1976), 1529.

32. F. B. McLean, H. E. Boesch, Jr., and J. M. McGarrity, IEEE Trans. Nucl. Sci. *NS-23* (1976), 1506.

33. J. R. Srour, S. Othmer, O. L. Curtis, Jr., and K. Y. Chiu, IEEE Trans. Nucl. Sci. *NS-23* (1976), 1513.

34. O. L. Curtis, Jr. and J. R. Srour, J. Appl. Phys. *48* (1977), 3819.

35. R. C. Hughes, Phys. Rev. B *15* (1977), 2012.

36. H. E. Boesch, Jr., J. M. McGarrity, and F. B. McLean, IEEE Trans. Nucl. Sci. *NS-25* (1978), 1012.

37. F. B. McLean, H. E. Boesch, Jr., and J. M. McGarrity, In *The Physics of SiO_2 and Its Interfaces*, S. T. Pantelides, ed., Pergamon Press, New York (1978), p 19.

38. H. E. Boesch, Jr., F. B. McLean, J. M. McGarrity, and P. S. Winokur, IEEE Trans. Nucl. Sci. *NS-25* (1978), 1239.

39. H. E. Boesch, Jr. and F. B. McLean, IEEE Trans. Nucl. Sci. *NS-32* (1985), 3940.

40. E. W. Montroll and G. H. Weiss, J. Math. Phys. *6* (1965), 167.

41. H. Scher and M. Lax, Phys. Rev. B *7* (1973), 4491.

42. H. Scher and E. W. Montroll, Phys. Rev. B *12* (1975), 2455.

43. G. Pfister and H. Scher, Adv. Phys. *27* (1978), 744.

44. F. B. McLean and G. A. Ausman, Jr., Phys. Rev. B *15* (1977), 1052.

45. I. G. Austin and N. F. Mott, Adv. Phys. *18* (1969), 41.

46. N. F. Mott and E. A. Davis, *Electronic Processes in Non-Crystalline Materials*, 2nd ed., Clarendon Press, Oxford (1979), pp 65-97.

47. D. Emin, Adv. Phys. *24* (1975), 305.

48. G. F. Derbenwick and H. H. Sander, IEEE Trans. Nucl. Sci. *NS-24* (1977), 2244.

49. G. F. Derbenwick and B. L. Gregory, IEEE Trans. Nucl. Sci. *NS-22* (1975), 2151.

50. K. H. Zaininger, Appl. Phys. Lett. *8* (1966), 140.

51. A. S. Grove and E. H. Snow, Proc. IEEE *54* (1966), 894.

52. K. H. Zaininger, IEEE Trans. Nucl. Sci. *NS-13* (1966), 237.

53. R. J. Powell and G. F. Derbenwick, IEEE Trans. Nucl. Sci. *NS-18* (1971), 99.

54. J. P. Mitchell and D. G. Denure, Solid State Elect. *16* (1973), 825.

55. J. M. Aitken, D. J. DiMaria, and D. R. Young, IEEE Trans. Nucl. Sci. *NS-23* (1976), 1526.

56. J. L. Peel and R. C. Eden, IEEE Trans. Nucl. Sci. *NS-18* (1971), 84.

57. J. P. Mitchell, IEEE Trans. Elec. Dev. *ED-14* (1967), 764.

58. J. N. Churchill, T. W. Collins, and F. E. Holmstrom, IEEE Trans. Elec. Dev. *ED-21* (1974), 768.

59. T. W. Collins, F. E. Holmstrom, and J. N. Churchill, IEEE Trans. Nucl. Sci. *NS-26* (1979), 5176.

60. T. R. Oldham, A. J. Lelis, and F. B. McLean, IEEE Trans. Nucl. Sci. *NS-33* (1986), 1203.

61. R. C. Hughes and C. H. Seager, IEEE Trans. Nucl. Sci. *NS-30* (1983), 4049.

62. J. M. Aitken and D. R. Young, IEEE Trans. Nucl. Sci. *NS-24* (1977), 2128.

63. H. E. Boesch, Jr., F. B. McLean, J. M. Benedetto, J. M. McGarrity, and W. E. Bailey, IEEE Trans. Nucl. Sci. *NS-33* (1986), 1191.

64. C. M. Dozier and D. B. Brown, IEEE Trans. Nucl. Sci. *NS-27* (1980), 1694.

65. H. E. Boesch, Jr., and F. B. McLean, IEEE Trans. Nucl. Sci. *NS-32* (1985), 3940.

66. J. J. Tzou, J. Y. C. Sun, and C. T. Sah, Appl. Phys. Lett. *43* (1983), 861.

67. G. H. Sigel, Jr., E. J. Friebele, R. J. Ginther, and D. L. Griscom, IEEE Trans. Nucl. Sci. *NS-21* (1974), 56.

68. S. Manzini and A. Modelli, In *Insulating Films on Semiconductors*, J. F. Verwels and D. R. Wolters, eds., North-Holland, New York (1983), p 112.

69. C. L. Marquardt and G. H. Sigel, Jr., IEEE Trans. Nucl. Sci. *NS-22* (1975), 2234.

70. P. M. Lenahan and P. V. Dressendorfer, IEEE Trans. Nucl. Sci. *NS-30* (1983), 4602.

71. R. H. Silsbee, J. Appl. Phys. *32* (1961), 1459.

72. F. J. Feigl, W. B. Fowler, and K. L. Yip, Solid State Comm. *14* (1974), 225.

73. D. L. Griscom, Nucl. Instr. Methods Phys. Res. *131* (1984), 481.

74. F. J. Grunthaner, P. J. Grunthaner, and J. Maserjian, IEEE Trans. Nucl. Sci. *NS-29* (1982), 1462.

75. H. E. Boesch, Jr., private communication.

76. P. S. Winokur, IEEE Trans. Nucl. Sci. *NS-29* (1982), 2102.

77. P. S. Winokur, K. G. Kerris, and L. Harper, IEEE Trans. Nucl. Sci. *NS-30* (1983), 4326.

78. N. S. Saks, M. G. Ancona, and J. A. Modolo, IEEE Trans. Nucl. Sci. *NS-31* (1984), 1249.

79. J. M. Benedetto, H. E. Boesch, Jr., F. B. McLean, and J. P. Mize, IEEE Trans. Nucl. Sci. *NS-32* (1985), 3916.

80. E. C. Ross and J. T. Wallmark, RCA Review *30* (1969), 366.

81. F. B. McLean, *A Direct Tunneling Model of Charge Transfer at the Insulator-Semiconductor Interface in MIS Devices*, Harry Diamond Laboratories, HDL-TR-1765 (October 1976).

82. A. H. Johnston and S. B. Roeske, IEEE Trans. Nucl. Sci. *NS-33* (1986), 1487.

83. P. S. Winokur, J. M. McGarrity, and H. E. Boesch, Jr., IEEE Trans. Nucl. Sci. *NS-23* (1976), 1580.

84. P. S. Winokur, H. E. Boesch, Jr., J. M. McGarrity, and F. B. McLean, IEEE Trans. Nucl. Sci. *NS-24* (1977), 2113.

85. J. M. McGarrity, P. S. Winokur, H. E. Boesch, Jr., and F. B. McLean, In *The Physics of SiO_2 and Its Interfaces*, S. T. Pantelides, ed., Pergamon Press, New York (1978), p 428.

86. P. S. Winokur, H. E. Boesch, Jr., J. M. McGarrity, and F. B. McLean, J. Appl. Phys. *50* (1979), 3492.

87. P. S. Winokur and H. E. Boesch, Jr., IEEE Trans. Nucl. Sci. *NS-27* (1980), 1647.

88. H. E. Boesch, Jr., and F. B. McLean, J. Appl. Phys. *60* (1986), 448.

89. P. S. Winokur, F. B. McLean, and H. E. Boesch, Jr., *Physical Processes Associated with Radiation-Induced Interface States*, Harry Diamond Laboratories, HDL-TR-2081 (April 1986).

90. H. E. Boesch, Jr., IEEE Trans. Nucl. Sci. *NS-29* (1982), 1446.

91. H. E. Boesch, Jr., and T. L. Taylor, IEEE Trans. Nucl. Sci. *NS-31* (1984), 1273.

92. J. R. Schwank, P. S. Winokur, F. W. Sexton, D. M. Fleetwood, J. H. Perry, P. V. Dressendorfer, D. T. Sanders, and D. C. Turpin, IEEE Trans. Nucl. Sci. *NS-33* (1986), 1178.

93. P. S. Winokur, E. B. Errett, D. M. Fleetwood, P. V. Dressendorfer, and D. C. Turpin, IEEE Trans. Nucl. Sci. *NS-32* (1985), 3954.

94. P. S. Winokur and M. M. Sokoloski, Appl. Phys. Lett. *28* (1976), 627.

95. S. K. Lai, J. Appl. Phys. *54* (1983), 2540.

96. C. T. Sah, IEEE Trans. Nucl. Sci. *NS-23* (1976), 1563.

97. A. G. Revesz, IEEE Trans. Nucl. Sci. *NS-24* (1977), 2102.

98. C. M. Svensson, in *The Physics of SiO_2 and Its Interfaces*, S. T. Pantelides, ed., Pergamon Press, New York (1978), p 328.

99. F. B. McLean, IEEE Trans. Nucl. Sci. *NS-27* (1980), 1651.

100. D. L. Griscom, J. Appl. Phys. *58* (1985), 2524.

101. D. B. Brown, IEEE Trans. Nucl. Sci. *NS-32* (1985), 3900.

102. E. P. EerNisse and G. F. Derbenwick, IEEE Trans. Nucl. Sci. *NS-23* (1976), 1534.

103. V. Zekeriya and T. P. Ma, IEEE Trans. Nucl. Sci. *NS-31* (1984), 1261.

104. F. Toyokawa, M. Tsukiji, M. Sakamoto, and K. Koboyashi, IEEE Trans. Nucl. Sci. *NS-33* (1986), 1210.

105. M. L. Reed and J. D. Plummer, IEEE Trans. Nucl. Sci. *NS-33* (1986), 1198.

106. K. Naruke, M. Yoshida, K. Maeguchi, and H. Tango, IEEE Trans. Nucl. Sci. *NS-30* (1983), 4054.

107. C. M. Dozier and D. B. Brown, IEEE Trans. Nucl. Sci. *NS-30* (1983), 4382.

108. T. P. Ma, Appl. Phys. Lett. *27* (1975), 615.

109. C. R. Viswanathan and J. Maserjian, IEEE Trans. Nucl. Sci. *NS-23* (1976), 1540.

110. T. P. Ma and R. C. Barker, J. Appl. Phys. *45* (1974), 317.

111. N. S. Saks, M. G. Ancona, and J. A. Modolo, IEEE Trans. Nucl. Sci. *NS-33* (1986), 1185.

112. C. T. Sah, J. Y. C. Sun, and J. J. T. Tzou, J. Appl. Phys. *53* (1982), 8886.

113. E. H. Poindexter, G. J. Gerardi, M. E. Rueckel, P. J. Caplan, N. M. Johnson, and D. K. Biegelsen, J. Appl. Phys. *56* (1984), 2844.

114. T. P. Ma, G. Scoggan, and R. Leone, Appl. Phys. Lett. *27* (1975), 61.

115. P. M. Lenahan and P. V. Dressendorfer, J. Appl. Phys. *55* (1984), 3495.

116. M. Knoll, D. Braunig, and W. R. Fahrner, IEEE Trans. Nucl. Sci. *NS-29* (1982), 1471.

117. Y. Nishi, Jpn. J. Appl. Phys. *5* (1966), 333.

118. E. H. Poindexter and P. J. Caplan, Prog. Surf. Sci. *14* (1983), 201.

119. P. M. Lenahan and P. V. Dressendorfer, Appl. Phys. Lett. *41* (1982), 542.

120. S. C. Sun and J. D. Plummer, IEEE Trans. Elec. Devices *ED-27* (1980), 1497.

121. A. H. Johnston, IEEE Trans. Nucl. Sci. *NS-31* (1984), 1427.

122. J. R. Schwank, P. S. Winokur, P. J. McWhorter, F. W. Sexton, P. V. Dressendorfer, and D. C. Turpin, IEEE Trans. Nucl. Sci. *NS-31* (1984), 1434.

123. P. S. Winokur, J. R. Schwank, P. J. McWhorter, P. V. Dressendorfer, and D. C. Turpin, IEEE Trans. Nucl. Sci. *NS-31* (1984), 1453.

124. P. J. McWhorter and P. S. Winokur, Appl. Phys. Lett. *48* (1986), 13.

125. G. Groeseneken, H. E. Maes, N. Beltran, and R. F. DeKeersmaecker, IEEE Trans. Elec. Devices *ED-31* (1984), 42.

126. K. F. Galloway, M. Gaitan, and T. J. Russell, IEEE Trans. Nucl. Sci. *NS-31* (1984), 1497.

127. C. M. Dozier, D. B. Brown, R. K. Freitag, and J. L. Throckmorton, IEEE Trans. Nucl. Sci. *NS-33* (1986), 1324.

128. H. E. Boesch, Jr., IEEE Trans. Nucl. Sci. *NS-33* (1986), 1337.

129. J. M. Benedetto and H. E. Boesch, Jr., IEEE Trans. Nucl. Sci. *NS-33* (1986), 1318.

130. D. B. Brown, IEEE Trans. Nucl. Sci. *NS-33* (1986), 1240.

131. R. L. Pease, R. M. Turfler, D. Platteter, D. Emily, and R. Blice, IEEE Trans. Nucl. Sci. *NS-30* (1983), 4216. See also R. Pease, D. Emily, and H. E. Boesch, Jr., IEEE Trans. Nucl. Sci. *NS-32* (1985), 3946.

132. J. L. Wirth and S. C. Rogers, IEEE Trans. Nucl. Sci. *NS-11* (1964), 24.

133. J. P. Raymond, 1985 IEEE NSREC Short Course, Monterey, CA (July 1985).

134. T. C. May and M. H. Woods, IEEE Trans. Electron Dev., *ED-26* (1979), 2.

135. J. F. Ziegler and W. Lanford, Science *206* (1979), 776.

136. C. M. Hsieh, P. C. Murley, and R. R. O'Brien, IEEE Electron Dev. Lett. *EDL-2* (1981), 103 and IEEE Trans. Electron Dev. *ED-30* (1983), 686.

137. F. B. McLean and T. R. Oldham, IEEE Trans. Nucl. Sci. *NS-29* (1982), 2018.

138. S. Kirkpatrick, IEEE Trans. Electron Dev. *ED-26* (1979), 1742.

139. T. R. Oldham and F. B. McLean, IEEE Trans. Nucl. Sci. *NS-30* (1983), 4493.

140. C. Hu, IEEE Elec. Dev. Lett. *EDL-3* (1982), 31.

141. G. C. Messenger, IEEE Trans. Nucl. Sci. *NS-29* (1982), 2024.

142. M. Shur, K. Lee, R. Choe, and E. Berger, IEEE Trans. Nucl. Sci. *NS-33* (1986), 1140.

143. T. R. Oldham, F. B. McLean, and J. M. Hartman, IEEE Trans. Nucl. Sci. *NS-33* (1986), 1646.

144. K. Soliman and D. K. Nichols, IEEE Trans. Nucl. Sci. *NS-30* (1983), 4464.

145. R. Koga and W. A. Kolasinski, IEEE Trans. Nucl. Sci. *NS-31* (1984), 1190.

146. J. R. Srour, S. Othmer, A. Bahraman, and R. A. Hartmann, IEEE Trans. Nucl. Sci. *NS-28* (1981), 3968.

147. J. R. Srour, Z. Shanfield, R. A. Hartmann, S. Othmer, and D. M. Newberry, IEEE Trans. Nucl. Sci. *NS-30* (1983), 4526.

148. J. R. Srour and R. A. Hartmann, IEEE Trans. Nucl. Sci. *NS-32* (1985), 4195.

149. A. E. Profio, *Radiation Shielding and Dosimetry*, J. Wiley & Sons, Toronto, Canada (1979).

150. L. F. Curtiss, *Introduction to Neutron Physics*, Van Nostrand, Princeton, NJ (1959).

151. W. S. Snyder and J. Neufeld, Brit. J. Radiol. *28* (1955), 342.

152. J. Lindhard, M. Scharff, and H. Schiott, Mat. Fys. Medd. Vid. Selsk. *33* (1963), 1.

153. B. R. Gossick, J. Appl. Phys. *30* (1959), 1214.

154. V. A. J. van Lint, R. E. Leadon, and J. F. Colwell, IEEE Trans. Nucl. Sci. *NS-19* (1972), 181.

155. G. P. Mueller, N. D. Wilsey, and M. Rosen, IEEE Trans. Nucl. Sci. *NS-29* (1982). 1493.

156. J. R. Srour and O. L. Curtis, IEEE Trans. Nucl. Sci. *NS-19* (1972), 362.

157. R. R. Holmes, Bell Telephone Laboratories technical report (October 1, 1970).

158. J. R. Srour, IEEE Trans. Nucl. Sci. *NS-20* (1973), 190.

159. M. S. Cooper, J. P. Retzler, and G. C. Messenger, IEEE Trans. Nucl. Sci. *NS-26* (1979), 4758.

160. R. Zuleeg, in *VLSI Electronics: Microstructure Science*, Vol. II, N. G. Einspruch and W. R. Wisseman, eds., Academic Press, New York (1985), p 391.

161. R. Zuleeg and K. Lehovec, IEEE Trans. Nucl. Sci. *NS-27* (1980), 1343.

162. M. Simons and E. E. King, IEEE Trans. Nucl. Sci. *NS-26* (1979), 5080.

163. W. T. Anderson, Jr., M. Simons, and W. F. Tseng, IEEE Trans. Nucl. Sci. *NS-33* (1986), 1442.

164. R. Zuleeg, J. K. Notthoff, and G. L. Troeger, IEEE Trans. Nucl. Sci. *NS-29* (1982), 1656.

165. W. T. Anderson, Jr., M. Simons, E. E. King, H. B. Dietrich, and R. J. Lambert, IEEE Trans. Nucl. Sci. *NS-29* (1982), 1533.

166. B. L. Buchanan, in *VLSI Handbook*, N. G. Einspruch, ed, Academic Press, New York (1985), p 565.

167. R. Zuleeg, J. K. Notthoff, and G. L. Troeger, IEEE Trans. Nucl. Sci. *NS-30* (1983), 4151.

168. M. A. Hopkins and J. R. Srour, IEEE Trans. Nucl. Sci. *NS-30* (1983), 4457.

169. M. A. Hopkins and J. R. Srour, IEEE Trans. Nucl. Sci. *NS-31* (1984), 1116.

170. A. F. Behle and R. Zuleeg, IEEE Trans. Elec. Devices *ED-19* (1972), 993.

171. S. E. Diehl, A. Ochoa, Jr., P. V. Dressendorfer, R. Koga, and W. A. Kolasinski, IEEE Trans. Nucl. Sci. *NS-29* (1982), 2032.

172. W. J. Stapor, R. L. Johnson, Jr., M. A. Xapsos, K. W. Fernald, A. B. Campbell, B. L. Bhuva, and S. E. Diehl, IEEE Trans. Nucl. Sci. *NS-33* (1986), 1610.

173. J. D. Plummer, Proc. 1986 IEEE IEDM (1986), 378.

174. J. R. Srour and K. Y. Chiu, IEEE Trans. Nucl. Sci. *NS-24* (1977), 2140.

175. N. S. Saks, J. M. Killiany, P. R. Reid, and W. D. Baker, IEEE Trans. Nucl. Sci. *NS-26* (1979), 5074.

176. H. E. Boesch, Jr., and J. M. McGarrity, IEEE Trans. Nucl. Sci. *NS-26* (1979), 4814.

177. L. Vadasz and A. S. Grove, IEEE Trans. Elec. Devices *ED-13* (1966), 863.

178. R. Wang, J. Dunkley, T. A. DeMassa, and L. F. Jelsma, IEEE Trans. Elec. Devices *ED-18* (1971), 386.

179. R. M. White, J. Appl. Phys. *34* (1963), 3559.

180. R. A. Graham and R. E. Hutchinson, Appl. Phys. Lett. *11* (1967), 69.

181. F. C. Perry, J. Appl. Phys. *41* (1970), 5017.

182. R. B. Oswald, Jr., F. B. McLean, D. R. Schallhorn, and L. D. Buxton, J. Appl. Phys. *42* (1971), 3463.

183. D. R. Schallhorn, R. B. Oswald, Jr., W. D. Scharf, G. L. Skillington, T. R. Oldham, and A. J. Baba, IEEE Trans. Nucl. Sci. *NS-22* (1975), 2576.

184. F.-C. Hsu, J. Hui, and K. Y. Chiu, Proc. 1985 IEEE IEDM (1985), 48.

185. E. Takeda and N. Suzuki, IEEE Elec. Dev. Lett. *4* (1983), 111.

186. F. J. Feigl, D. R. Young, D. J. DiMaria, S. Lai, and J. Calise, J. Appl. Phys. *52* (1981), 5665.

187. J. D. McBrayer, D. M. Fleetwood, R. A. Pastorek, and R. V. Jones, IEEE Trans. Nucl. Sci. *NS-32* (1985), 3935.

DISTRIBUTION

ADMINISTRATOR
DEFENSE TECHNICAL INFORMATION CENTER
ATTN DTIC-DDA (12 COPIES)
CAMERON STATION, BUILDING 5
ALEXANDRIA, VA 22304-6145

OFFICE OF DEPUTY CHIEF OF STAFF
FOR RES, DEV, & ACQ
ATTN DAMA-ARZ-D, RES PROGRAMS
WASHINGTON, DC 20310

HQ DEFENSE NUCLEAR AGENCY
ATTN R. C. WEBB
ATTN RAEE, L. M. COHN
ATTN T. D. STANLEY
ATTN C. H. FORE
ATTN RAEE, S. P. ERNST
6801 TELEGRAPH RD
ALEXANDRIA, VA 22305

OFFICE OF THE SECRETARY OF DEFENSE
DTSA/STRATEGIC TRADE
ATTN LTC BOSE
OUSDP COMMAND CENTER
ROOM 4D825
WASHINGTON, DC 20301-2600

DEPT OF THE DEFENSE
ATTN D. O. PATTERSON
2207 PAUL SPRING PKWY M104
ALEXANDRIA, VA 22308

US ARMY ELECTRONICS TECHNOLOGY & DEVICES
LABORATORY
ATTN G. J. IAFRATE
ATTN R. J. ZETO
ATTN T. HUNTER
ATTN B. PFEFFER
ATTN E. H. POINDEXTER
FT MONMOUTH, NJ 07703-5302

COMMANDER
US ARMY MATERIEL COMMAND
ATTN AMCCN-N
5001 EISENHOWER AVE
ALEXANDRIA, VA 22333-0001

COMMANDER
US ARMY NUCLEAR & CHEMICAL AGENCY
ATTN MONA-NV, MAJ DOMASZEK
ATTN MONA-NU, R. A. PFEFFER
7500 BACKLICK RD, BLDG 2073
SPRINGFIELD, VA 22150

ARMY RESEARCH OFFICE
ATTN SLCRO, M. STROSCIO, ELECTRONICS DIV
PO BOX 12211
RESEARCH TRIANGLE PARK, NC 27709

USASDC
ATTN R. K. DUDNEY
ATTN C. HARPER
ATTN COL J. SHEEHY
PO BOX 1500 DASD-H-YA
HUNTSVILLE, AL 35807-3801

US MILITARY ACADEMY
DEPT OF PHYSICS
ATTN P. O'REILLY
ATTN W. EICHINGER
WEST POINT, NY 10996

US NAVAL ACADEMY
ATTN T. S. LIM
ELECTRICAL ENG DEPT. STOP 14B
ANAPOLIS, MD 21402

US NAVAL ACADEMY
ATTN R. L. MARTIN
E.E. DEPT MS 14B
ANNAPOLIS, MD 21402

US NAVY
ATTN W. B. MOHR
1822 RAWLINGS PL
CROFTON, MD 21114

NWSC CRANE
ATTN T. TURFLINGER
BLDG 2087 CODE 60541
CRANE, IN 47522

OFFICE OF NAVAL RESEARCH
ATTN K. DAVIS, CODE 414
ATTN M. N. YODER, CODE 414
ATTN R. C. POHANKA, CODE 431N
800 N. QUINCY ST
ARLINGTON, VA 22217-5000

OFFICE OF NAVAL RESEARCH DETACHMENT
ATTN C. LAO
1030 EAST GREEN ST
PASADENA, CA 91106

NAVAL RESEARCH LABORATORY
ATTN CODE 6813, M. G. ANCONA
ATTN CODE 6815, W. T. ANDERSON
ATTN CODE 4682, D. B. BROWN
ATTN CODE 4613, A. B. CAMPBELL
ATTN CODE 6016, W. E. CARLOS
ATTN CODE 4682, C. M. DOZIER
ATTN CODE 4680, R. K. FREITAG
ATTN CODE 6570, D. L. GRISCOM
ATTN CODE 6816, H. HUGHES
ATTN CODE 6816, W. C. JENKINS
ATTN CODE 6810, J. M. KILLIANY
ATTN CODE 4673, A. R. KNUDSON

DISTRIBUTION (cont'd)

NAVAL RESEARCH LABORATORY (cont'd)
ATTN CODE 6816, R. J. LAMBERT
ATTN CODE 4653, A. I. NAMENSON
ATTN CODE 4611, E. L. PETERSON
ATTN CODE 4610, J. RITTER
ATTN CODE 6813, N. S. SAKS
ATTN CODE 4613, W. J. STAPOR
ATTN CODE 6816, R. STAHLBUSH
ATTN CODE 4615, G. SUMMERS
ATTN CODE 6813, J. R. WATERMAN
ATTN CODE 4613, M. ZAPSOS
4555 OVERLOOK AVE, SW
WASHINGTON, DC 20375-5000

NAVAL WEAPONS SUPPORT CTR
ATTN CODE 6054, T. D. ELLIS
ATTN CODE 6054, D. W. EMILY
ATTN CODE 6054, Y. D. KIM
ATTN CODE 6054, D. G. PLATTETER
ATTN J. L. RAMSEY
CRANE, IN 47522

ROME AIR DEVELOPMENT CENTER
RADC/ESR
ATTN A. R. FREDERICKSON
ATTN J. C. GARTH
ATTN S. MITTLEMAN
ATTN J. SCHOTT
ATTN W. SHEDD
HANSCOM AFB, MA 01731

AIR FORCE INST. OF TECH.
AFIT/ENP
ATTN M. J. SABOCHICK
WRIGHT-PATTERSON AFB, OH 45433

AIR FORCE WEAPONS LAB
ATTN R. J. MAIER
ATTN K. K. HUNT, AFWL/NTCT
ATTN G. S. JOLLY, AFW/NTCTR
KIRTLAND AFB, NM 87117-6008

NASA/GODDARD SPACE FLIGHT CTR
ATTN CODE 311, J. W. ADOLPHSEN
ATTN CODE 313, V. DANCHENKO
ATTN CODE 633, E. G. STASSINOPOULOS
GREENBELT, MD 20771

NASA HEADQUARTERS
ATTN M. M. SOKOLOSKI
NASA HEADQUARTERS, DC 20546

THE AEROSPACE CORP
ATTN CHARLES BARNES, M2-244
ATTN P. BUCHMAN, M4/996
ATTN R. KOGA, M2-259
ATTN N. SRAMEK, M4/989
ATTN K. T. WILSON, M4/989

THE AEROSPACE CORP (cont'd)
ATTN T. C. ZIETLOW, M2/244
PO BOX 92957
LOS ANGELES, CA 90009

ARACOR
ATTN L. J. PALKUTI
425 LAKESIDE DR
SUNNYVALE, CA 94086

AT&T BELL LABS
ATTN L. MANCHANDA
6001 MOUNTAIN AVE
MURRY HILL, NJ 07974

AT&T BELL LABS
ATTN R. L. REMKE
PO BOX 13566
READING, PA 19607

JAMES T. BLANDFORD
CONSULTANT
ATTN JAMES T. BLANDFORD
10 CERRITO
IRVINE, CA 92715

BOEING ELECTRONICS
ATTN A. JOHNSTON
ATTN BOR-YEN MAO
PO BOX 24969
SEATTLE, WA 98125

BOEING AEROSPACE CO
ATTN T. CRISWELL
PO BOX 3999
SEATTLE, WA 98124

BOEING AEROSPACE CO
ATTN ITSU ARIMURA
6045 86TH SE 501-369
MERCER ISLAND, WA 98040

BOEING AEROSPACE
ATTN P. R. MEASEL
9510 NE 5TH ST
BELLEVUE, WA 98004

BOOZ ALLEN HAMILTON
ATTN P. E. DeBOY
ATTN J. TERRELL
ATTN R. E. McCOSKEY
4330 EAST WEST HWY S623
BETHESDA, MD 20814

CEA (FRANCE)
ATTN L. J. LUC
CENTRE D-ETUDES DE BRUYERES-
LE-CHATEL FB 12
BRUYERS LE CTL 91680 FRANCE

CENTRAL RESEARCH LAB-HATACHI
1-280
ATTN TAKAHIRO OKABE
TOKYO 185 JAPAN

CIMSA SINTRA
ATTN J. PINEL
AVE du GENERAL EISENHOWER
BP 1009
31023 TOULOUSE CEDEX FRANCE

COMSAT
ATTN A. MEULENBERG
CLARKSBURG, MD 20855

CONTROL DATA CORP
ATTN D. M. NEWBERRY
2300 E 88TH ST
BLOOMINGTON, MN 55420

G. C. MESSENGER
CONSULTANT
3111 BEL AIR DR 7F
LAS VEGAS, NV 89109

DARPA/DSO
ATTN S. A. ROOSILD
2027 LAKEBREEZE WAY
RESTON, VA 22091

FULMER RESEARCH LABS
ATTN A. HOLMES-SIEDLE
STOKE POGES
SLOUGH BERKS SL2 4QD ENGLAND

GE AEROSPACE
ATTN J. L. ANDREW
PO BOX 8555 M1211
PHILADELPHIA, PA 19101

GENERAL ELECTRIC
ATTN D. TASCA
PO BOX 8555 ROOM M1211
PHILADELPHIA, PA 19101

GENERAL ELECTRIC CR&D
ATTN H. H. WOODBURY
PO BOX 8 KW-B314
SCHENECTADY, NY 12301

GENERAL ELECTRIC
ATTN J. BLACK
3395 TARLETON EAST
DURHAM, NC 27713

HAHN MEITNER INSTITUT
ATTN D. BRAUNIG
GLIENICKER STR.100 PO BOX 27255
1000 BERLIN 39 CA GERMANY
GERMANY 030-80092494

HARRIS SEMICONDUCTOR
ATTN J. C. LEE
PO BOX 883 MS54-102
MELBOURNE, FL 32902

HARRIS SEMICONDUCTOR
ATTN W. H. SPEECE
PO BOX 883 M/S 54-103
MELBOURNE, FL 32901

HARRIS SEMICONDUCTOR
ATTN J. B. LONG
PO BOX 883 MS 53/210
MELBOURNE, FL 32901

HARRIS CORPORATION
ATTN J. E. SCHROEDER
PO BOX 94000
MELBOURNE, FL 32902

HARRIS SEMICONDUCTOR
ATTN R. D. CHERNE
ATTN J. BULLER
PO BOX 883 M/S 54-103
MELBOURNE, FL 32901

HARRIS GASD
ATTN WAYNE E. ABARE
335 MEADOWWOOD LN DIV. 2147
W. MELBOURNE, FL 32904

HONEYWELL
ATTN J. W. SCHRANKLER
12001 ST HWY 55
PLYMOUTH, MN 55441

HONEYWELL
ATTN J. J. SILVER
1150 E. CHEYENNE MTN BLVD
COLORADO SPRINGS, CO 80906

HONEYWELL SYSTEMS & RESEARCH CTR
ATTN D. F. BERNDT
335 PINEVIEW LANE N
PLYMOUTH, MN 55441

HONEYWELL SYSTEMS & RESEARCH CENTER
ATTN R. A. BELT
17835 18TH CIRCLE
PLYMOUTH, MN 55447

HONEYWELL, INC
ATTN R. RABE
SSEP-MS/14-2015
12001 STATE HWY 55
PLYMOUTH, MN 55441

HONEYWELL, INC
ATTN A. P. JOHNSON
2600 RIDGEWAY PKWY
MN17-2341
MINNEAPOLIS, MN 55413

HUGHES AIRCRAFT CORP
ATTN K. G. AUBUCHON
ATTN A. OCHOA
6155 EL CAMINO REAL
CARLSBAD, CA 92008

HUGHES AIRCRAFT
ATTN D. BINDER
PO BOX 92919
LOS ANGELES, CA 90009

IBM
ATTN N. HADDAD
ATTN A. EDENFELD
ATTN T. F. MAHAR, JR.
ATTN B. A. POSEY
ATTN L. R. ROCKETT
ATTN T. M SCOTT
ATTN S. M. TYPSON
9500 GODWIN DR
BLDG 867/1B
MANASSAS, VA 22110

ICS RADIATION TECH
ATTN M. GAUTHIER
8416 FLORENCE AVE #205
DOWNEY, CA 90240-3919

IRT
ATTN J. C. PICKEL
ATTN N. J. RUDIE
101 S KRAMER BLVD SUITE 132
PLACENTIA, CA 27514

IRT CORP
ATTN J. C. AZAREWICZ
ATTN J. W. HARRITY
ATTN M. A. ROSE
ATTN J. M. WILKINFELD
PO BOX 85317
SAN DIEGO, CA 92138

IRT CORP
ATTN T. A. MARTIN
1364 BEVERLY RD STE 101
McLEAN, VA 22101

JAYCOR
ATTN P. G. COAKLEY
ATTN R. E. LEADON
ATTN W. SEIDLER
11011 TORREYANA RD
PO BOX 85154
SAN DIEGO, CA 92138

JAYCOR
ATTN S. C. ROGERS
2811 WILSHIRE BLVD #690
SANTA MONICA, CA 90272

JPL-CALTECH
ATTN P. A. ROBINSON
ATTN J. W. WINSLOW
4800 OAK GROVE DR
PASADENA, CA 91109

JET PROPULSION LAB
ATTN M. G. BUEHLER
ATTN J. COSS
ATTN D. K. NICHOLS
ATTN W. E. PRICE
ATTN W. STACKHOUSE
ATTN J. A. ZOUTENDYK
4800 OAK GROVE DR MS 180-202
PASADENA, CA 91109

KAMAN SCIENCES CORP
ATTN E. E. CONRAD
1911 JEFFERSON DAVIS HWY
SUITE 1200
ARLINGTON, VA 22202

KAMAN TEMPO
ATTN B. A. ALFONTE
2560 HUNTINGTON AVE
SUITE 500
ALEXANDRIA, VA 22303

LOCKHEED
ATTN J. S. SMITH
5321 HANOVER ST
LOCKHEED RES LAB
PALO ALTO, CA 94034

LOS ALAMOS NAT LAB
ATTN R. S. WAGNER
LOS ALAMOS, NM 87545

MARTIN MARIETTA LABS
ATTN S. P. BUCHNER
1450 SOUTH ROLLING RD 4M-424
BALTIMORE, MD 21227

DISTRIBUTION (cont'd)

MATRA AEROSPACE
ATTN P. GAUTIER
37 ave LOUIS-BREGUET B.P.1
78146 VELIZY-VILLACOUBLAY CEDEX
FRANCE 33-1-39469600

McDONNELL DOUGLAS
ATTN R. ZULEEG
5301 BOLSA AVE MS 28
HUNTINGTON BEACH, CA 92647

MISSION RESEARCH CORP
ATTN E. A. BURKE
11 INDIAN HILL RD
WOBURN, MA 01801

MISSION RESEARCH CORP
ATTN D. R. ALEXANDER
ATTN R. L. PEASE
1720 RANDOLPF RD
ALBUQUERQUE, NM 87106

MISSION RESEARCH CORP
ATTN A. H. KALMA
4935 N 30TH ST
COLORADO SPRINGS, CO 80919

MISSION RESEARCH CORP
ATTN J. P. RAYMOND
ATTN D. P. SNOWDEN
ATTN V. A. J. VAN LINT
5434 RUFFIN RD
SAN DIEGO, CA 92123

MYERS AND ASSOCIATES
ATTN D. K. MYERS
16415 RUSTLING OAK
MORGAN HILL, CA 95037

NATIONAL BUREAU OF STANDARDS
ATTN H. S. BENNETT, ROOM B310
ATTN T. J. RUSSEL
ATTN S. M. SELTZER, 536.01
ATTN J. S. SUHLE, B308
BLDG 225
GAITHERSBURG, MD 20893

NATIONAL SEMICONDUCTOR
ATTN F. C. JONES
ATTN P. McNALLY
112 BELHAVEN DR
LOS GATO, CA 95030

NORTHROP RESEARCH & TECH CTR
ATTN A. BAHARMAN
ATTN K. KITAZAKI
ATTN M. M. MORIWAKI
ATTN Z. SHANFIELD

NORTHROP RESEARCH & TECH CTR
(cont'd)
ATTN J. SROUR
ONE RESEARCH PARK 0365/T60
PALOS VERDES PENINSU, CA 90274

NORTHROP ELECT
ATTN E. KING
2301 W 120TH ST
HAWTHORNE, CA 90250

NORTHROP ELECTRONICS DIV
ATTN G. E. DAVIS
321 19TH ST, "B"
MANHATTEN BEACH, CA 90266

OAK RIDGE NAT LAB
ATTN R. H. RITCHIE
OAK RIDGE, TN 37830

OUSDA (R/AT) (CET)
ATTN LTC H. BROWN
ATTN COL W. FREESTONE
ATTN B. SUMNER
PENTAGON MAIL ROOM 3D-139
1211 FERN ST
WASHINGTON, DC 20310

PHYSICON
ATTN J. D. HARPER
3225 BOB WALLACE AVE SUIT I
HUNTSVILLE, AL 35805

PHYSICON INC
ATTN T. G. HENDERSON
10303 MELANIE DR
HUNTSVILLE, AL 35803

RAYTHEON MICROELECTRONICS CTR
ATTN S. L. KANE
358 LOWELL ST MC 54
ANDOVER, MA 01810

RAYTHEON CO
ATTN H. FLESCHER
12 ORANISON RD
WESTON, MA 02193

RCA
ATTN T. E. SULLIVAN
ATTN H. VELORIC
RT 202 MZ113
SOMERVILLE, NJ 08876

RCA MICROELECTRONICS CTR
ATTN J. E. SAULTZ
ATL BLDG 145-3 ROUTE 38
MOORESTOWN, NJ 08057

RCA ASTRO
ATTN G. BRUCKER
PO BOX 800 410-2-C-19
PRINCETON, NJ 08543-0800

RCA CORP
MOORESTOWN CORP CENTER
ATTN J. S. PRIDMORE
ATL BLDG
MOORESTOWN, NJ 08057

R&D ASSOCIATES
ATTN G. M. SAFONOV
PO BOX 9695 BLDG 870
MARINA del REY, CA 90295

R&D ASSOCIATES
ATTN F. COPPAGE
PO BOX 9335
ALBUQUERQUE, NM 87119

REC ELECTRONICS INC
ATTN R. E. CONKLIN
114 WAYNE DR
FAIRBORN, OH 45324

RESEARCH TRIANGLE INSTITUTE
ATTN M. SIMONS
PO BOX 12194
RESEARCH TRIANGLE PARK, NC 27709

SACHS/FREEMAN ASSOC
ATTN LEON S. AUGUST
6920 BAYLOR DR
ALEXANDRIA, VA 22307

SAIC
ATTN J. SPRATT
2615 PAC COAST HWY #300
HERMOSA BEACH, CA 90254

SAIC
ATTN D. MILLWARD
ATTN D. LONG
102290 SORRENTO VALLEY RD
SAN DIEGO, CA 92121

SANDIA NATIONAL LAB
ATTN DIV. 1233, W. BEEZHOLD
ATTN DIV. 1232, D. E. BEUTLER
ATTN DIV 7252, D. W. BUSHMIRE
ATTN DEPT 2120, W. R. DAWES, JR.
ATTN DIV 2144, P. V. DRESSENDORFER
ATTN DIV 2147, D. M. FLEETWOOD
ATTN DIV 2126, J. E. GOVER
ATTN B. L. GREGORY
ATTN DIV 113, R. C. HUGHES
ATTN ORG 2151, W. C. LOVEJOY
ATTN DIV. 2144, J. D. McBRAYER
ATTN DIV. 2146, P. J. McWHORTER

SANDIA NATIONAL LAB (cont'd)
ATTN DIV 2144, J. R. SCHWANK
ATTN DIV 2142, F. W. SEXTON
ATTN H. T. WEAVER
ATTN DIV 2146, P. S. WINOKUR
ATTN DIV 2126, T. F. WROBEL
PO BOX 5800
ALBUQUERQUE, NM 87185

DAVID SARNOFF RESEARCH CTR
ATTN G. W. CULLEN, CN5300
ATTN R. K. SMELTZER
ATTN K. SCHLESIER, CN5300 3-079
PRINCETON, NJ 07543-5300

SDIO/T/IS
ATTN J. IONSON
ATTN K. WU
ATTN LTC M. KEMP
ATTN LTC R. GAJEIRSKI
THE PENTAGON
WASHINGTON, DC 20301-7100

SIMTEK CORP
ATTN G. DERBENWICK
1626 VICKERS DR
COLORADO SPRINGS, CO 80918

SPIRE
ATTN B. BUCHANAN
PATRIOTS PARK
BEDFORD, MA 01730

STANDARD OIL CO RESEARCH CTR
ATTN H. SCHER
4440 WARRENSVILLE CENTER RD
CLEVELAND, OH 44128

TELEDYNE SYSTEMS CO
ATTN J. H. SOKOL
M/S 16
NORTHRIDGE, CA 91304

TELEDYNE BROWN ENGINEERING
ATTN H. A. HARDT
704 CORLETT DR
M/S 47
HUNTSVILLE, AL 35802

TEXAS INSTRUMENTS
ATTN T. F. CHEEK, JR
PO BOX 660246 M/S 3145
DALLAS, TX 75266

TEXAS INSTRUMENTS
ATTN MISHEL MATLOUBIAN
PO BOX 655012 MS 944
DALLAS, TX 75265

TEXAS INSTRUMENTS
ATTN R. SUNDARESAN
MS 944 PO BOX 655621
DALLAS, TX 75040

TEXAS INSTRUMENTS
ATTN L. R. HITE
PO BOX 655621 MS369
DALLAS, TX 75252

TEXAS INSTRUMENTS
ATTN T. HOUSTON
627 OPAL LN
RICHARDSON, TX 75080

TEXAS INSTRUMENTS
ATTN C. A. BROWN
1512 RIDGEVIEW DR
ARLINGTON, TX 76012

TEXAS INSTRUMENTS, INC
ATTN F. W. POBLENZ
1923 DEEP VALLEY DR
RICHARDSON, TX 75080

TEXAS INSTRUMENTS, INC
ATTN W. BAILEY
PO BOX 655621
DALLAS, TX 75265

TRW
ATTN A. A. WITTELES
6908 VERDE RIDGE RD
PALOS VERDES, CA 90274

TRW
ATTN DAVID W. ALEXANDER
416 THE TERRACE #4
REDLANDS, CA 92373

TRW
ATTN M. HOPKINS
ONE SPACE PARK MS134/8822
REDONDO BEACH, CA 90278

TRW
ATTN JAMES S. CABLE
ONE SPACE PARK D1/1302
REDONDO BEACH, CA 90278

TRW
ATTN MILTON ASH
ONE SPACE PARK R6/2184
REDONDO BEACH, CA 90278

TRW
ATTN A. CARLAN
ONE SPACE PARK 134-9039
REDONDO BEACH, CA 90278

UNITED TECH. MICROELECTRONICS CTR
ATTN C. GWYN
1575 GARDEN OF THE GODS RD
COLORADO SPRINGS, CO 80907

UNITED TECHNOLOGIES MICROELECTRONICS CTR
ATTN R. WOODRUFF
1575 GARDEN OF THE GODS
COLORADO SPRINGS, CO 80907

UNITED TECHNOLOGIES CORP MOSTEK
ATTN J. P. MIZE
CARROLLTON, TX 75006

WESTINGHOUSE
ATTN F. BLAHA
421 DAVID DR
ARNOLD, MD 21012

WASHINGTONHOUSE ELECT
ATTN E. J. VITEK
PO BOX 1521 MS 5210
BALTIMORE, MD 21203

WESTINGHOUSE ELECTRIC
ATTN R. CRICCHI
PO BOX 1521 MS3531
BALTIMORE, MD 21203

WOLICKI ASSOCIATES INC
ATTN E. WOLICKI
1310 GATEWOOD DR MS12
ALEXANDRIA, VA 22307

UNIVERSITY OF ARIZONA
ATTN K. F. GALLOWAY
BLDG 104, ELEC & COMP ENG
TUCSON, AZ 85721

CLARKSON UNIVERISTY
ATTN P. J. McNULTY
PO BOX 292
CANTON, NY 13617

HAMPTON UNIVERSITY 6465
ATTN DEMETRIUS D. VENABLE
HAMPTON, VA 23668

UNIVERSITY OF NEW MEXICO
DEPT EEE
TAPY HALL
ATTN D. A. NEAMAN
ALBUQUERQUE, NM 87131

NORTH CAROLINA SU
ATTN L. MASSENGILL
NCSDU-ECE DEPT. BOX 7911
RALEIGH, NC 27695-7911

DISTRIBUTION (cont'd)

NORTH CAROLINA SU
ATTN J. HAUSER
ECE DEPT BOX 7911
RALEIGH, NC 27695-7911

PENNSYLVANIA STATE UNIVERSITY
ATTN W. WARREN, 127 HAMMOND BLDG
ATTN H. WITHAM, 227 HAMMOND BLDG
ATTN P. M. LANAHAN, 123 HAMMOND BLDG
UNIVERSITY PARK, PA 16802

RENSSELAER POLYTECHNIC INST
ATTN R. C. BLOCK
RPI LINAC
TROY, NY 12180

VANDERBILT UNIVERSITY
ATTN D. KERNS
ATTN S. KERNS
DEPT OF ELECTRICAL ENGINEERING
NASHVILLE, TN 37212

YALE UNIVERSITY
DEPT OF ELECTRICAL ENGINEER
ATTN T. P. MA
ATTN E. DaSILVA
DEPT OF ELECT. ENG.
PO BOX 2157 YALE S
NEW HAVEN, CT 06520

US ARMY LABORATORY COMMAND
ATTN TECHNICAL DIRECTOR, AMSLC-TD

INSTALLATION SUPPORT ACTIVITY
ATTN LEGAL OFFICE, SLCIS-CC

USAISC
ATTN RECORD COPY, ASNC-ADL-TS
ATTN TECHNICAL REPORTS BRANCH,
ASNC-ADL-TR

HARRY DIAMOND LABORATORIES
ATTN D/DIVISION DIRECTORS
ATTN LIBRARY, SLCHD-TL (3 COPIES)
ATTN LIBRARY, SLCHD-TL (WOODBRIDGE)
ATTN CHIEF, SLCHD-NW-E
ATTN CHIEF, SLCHD-NW-EC
ATTN CHIEF, SLCHD-NW-ED
ATTN CHIEF, SLCHD-NW-EE
ATTN CHIEF, SLCHD-NW R
ATTN CHIEF, SLCHD-NW-RA
ATTN CHIEF, SLCHD-NW-RC
ATTN CHIEF, SLCHD-NW-RE
ATTN CHIEF, SLCHD-NW-RH
ATTN CHIEF, SLCHD-NW-RI
ATTN CHIEF, SLCHD-NW-P
ATTN CHIEF, SLCHD-TT
ATTN R. G. WARDELL, SLCHD-DE-OS
ATTN B. ZABLUDOWSKI, SLCHD-IT-EB
ATTN B. VAULT, SLCHD-NW

HARRY DIAMOND LABORATORIES (cont'd)
ATTN A. HERMANN, SLCHD-NW-EC
ATTN C. KENYON, SLCHD-NM-EC
ATTN C. LE, SLCHD-NW-EC
ATTN T. MAK, SLCHD-NW-EC
ATTN R. MOORE, SLCHD-NW-EC
ATTN A. NGUYEN, SLCHD-NW-EC
ATTN C. REIFF, SLCHD-NW-EC
ATTN D. TROXEL, SLCHD-NW-EC
ATTN J. BRAND, SLCHD-NW-P
ATTN J. CORRIGAN, SLCHD-NW-P
ATTN R. POLIMADEI, SLCHD-NW-P
ATTN A. BABA, SLCHD-NW-RA
ATTN L. BELLIVEAU, SLCHD-NW-RA
ATTN C. MERKEL, SLCHD-NW-RA
ATTN R. FLEETWOOD, SLCHD-NW-RA
ATTN B. SCHALLHORN, SLCHD-NW-RA
ATTN M. SMITH, SLCHD-NW-RA
ATTN J .M. BENEDETTO, SLCHD-NW-RC
ATTN K. W. BENNETT, SLCHD-NW-RC
ATTN T. V. BLOMQUIST, SLCHD-NW-RC
ATTN H. E. BOESCH, SLCHD-NW-RC
(5 COPIES)
ATTN M. DIMANNA, SLCHD-NW-RC
ATTN A. J. LELIS, SLCHD-NW-RC
ATTN W. DELANCEY, SLCHD-NW-RC,
ATTN T. GRIFFIN, SLCHD-NW-RC
ATTN J. HARTMAN, SLCHD-NW-RC
ATTN L. MADOO, SLCHD-NW-RC
ATTN J. M. McGARRITY, SLCHD-NW-RC
(20 COPIES)
ATTN R. REAMS, SLCHD-NW-RC
ATTN B. J. ROD, SLCHD-NW-RC
ATTN T. TAYLOR, SLCHD-NW-RC
ATTN C. FAZI, SLCHD-NW-RE
ATTN R. GARVER, SLCHD-NW-RE
ATTN J. TATUM, SLCHD-NW-RE
ATTN A. WARD, SLCHD-NW-RE
ATTN M. ZAHRIGAN, SLCHD-NW-RE
ATTN J. BLACKBURN, SLCHD-NW-RH
ATTN M. BUMBAUGH, SLCHD-NW-RH
ATTN H. EISEN, SLCHD-NW-RH
ATTN R. GILBERT, SLCHD-NW-RH
ATTN S. MURRILL, SLCHD-NW-RH
ATTN G. OVREBO, SLCHD-NW-RH
ATTN P. REINER, SLCHD-NW-RH
ATTN C. ROSS, SLCHD-NW-RH
ATTN C. SELF, SLCHD-NW-RH
ATTN C. TIPTON, SLCHD-NW-RH
ATTN J. VANDERWALL, SLCHD-NW-RH
ATTN H. BRANDT, SLCHD-NW-RI
ATTN A. BROMBORSKY, SLCHD-NW-RI
ATTN D. DAVIS, SLCHD-NW-RI
ATTN G. HUTTLIN, SLCHD-NW-RI
ATTN A. KEHS, SLCHD-NW-RI
ATTN K. KERRIS, SLCHD-NW-RI
ATTN R. LAMB, SLCHD-NW-RI
ATTN L. LEBELO, SLCHD-NW-RI
ATTN M. LITZ, SLCHD-NW-RI
ATTN B. RUTH, SLCHD-NW-RI

DISTRIBUTION (cont'd)

HARRY DIAMOND LABORATORIES (cont'd)
ATTN J. SOLN, SLCHD-NW-RI
ATTN D. WITTAKER, SLCHD-NW-RI
ATTN C. ARSEM, SLCHD-ST-AD
ATTN T. BAHDER, SLCHD-ST-RA
ATTN J. BRUNO, SLCHD-ST-RA
ATTN P. B. JOHNSON, SLCHD-ST-A
ATTN J. STELLATO, SLCHD-ST-RA
ATTN G. SIMONIS, SLCHD-ST-RA
ATTN C. MORRISON, SLCHD-ST-RA
ATTN R. NEIFELD, SLCHD-ST-RA
ATTN M. TOBIN, SLCHD-ST-RA
ATTN D. WORTMAN, SLCHD-ST-RA
ATTN S. KULPA, SLCHD-PO-P
ATTN T. R. OLDHAM, SLCHD-NW-RC (10 COPIES)
ATTN F. B. McLEAN, SLCHD-NW-RC (40 COPIES)